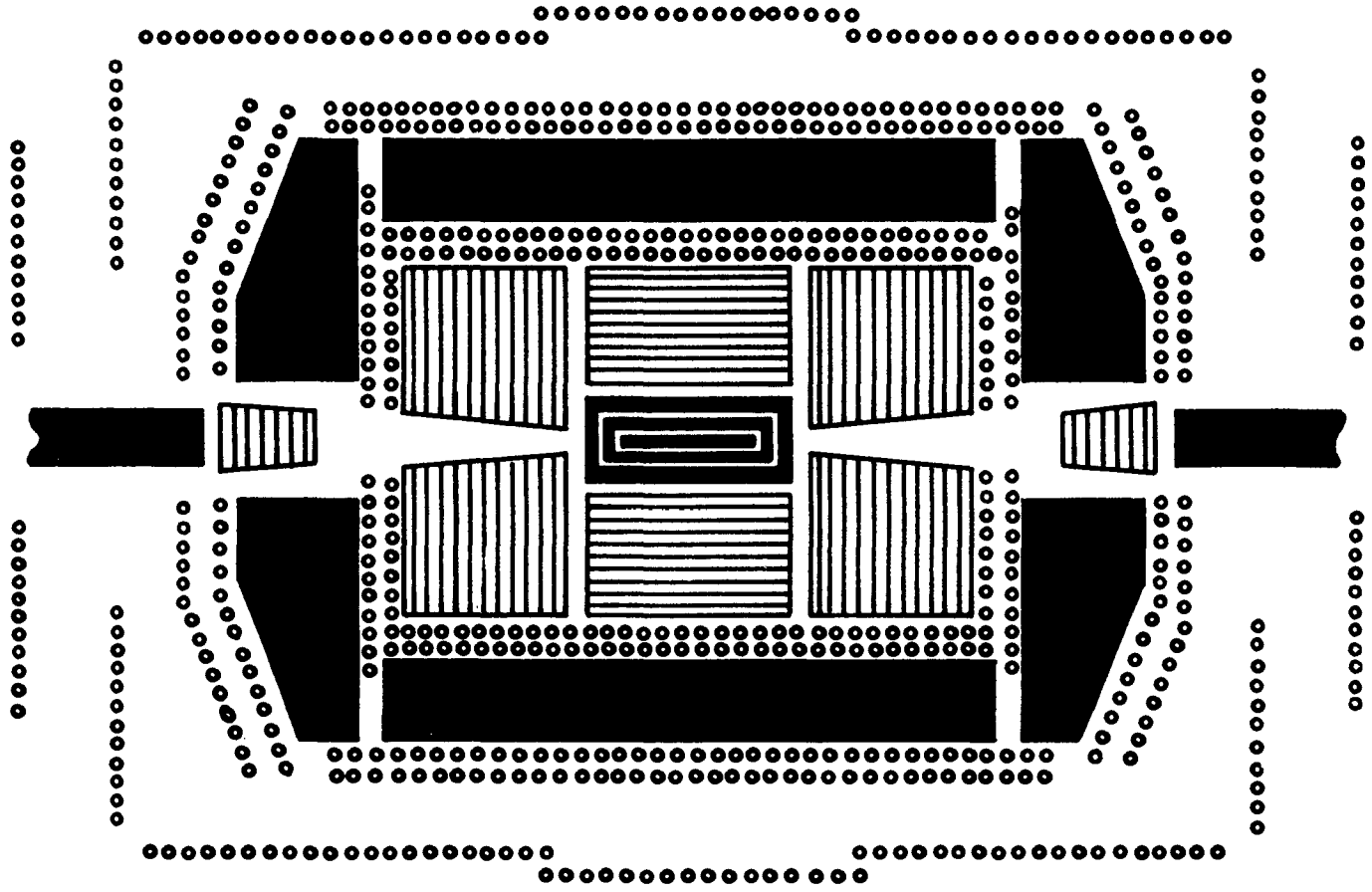

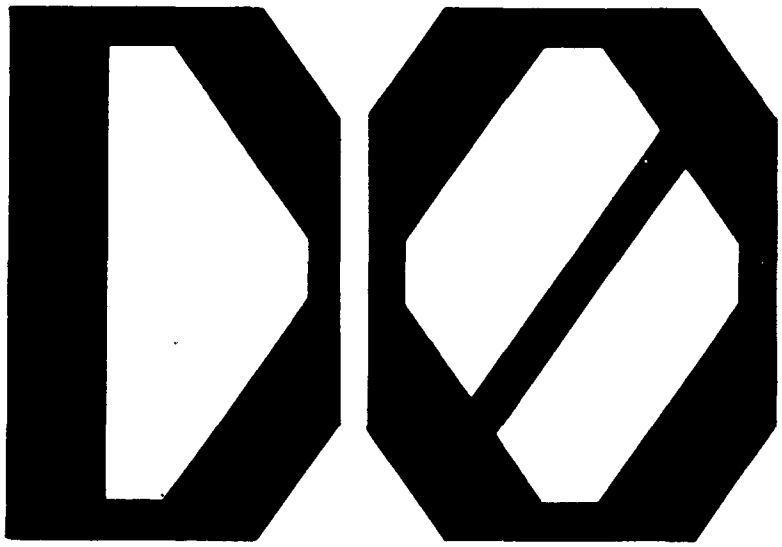

DESIGN REPORT

An Experiment at DO to Study Antiproton - Proton Collisions at 2 TeV

December 1983

THE DO COLLABORATION

B. Pifer
University of Arizona

L. Ahrens, S. Aronson, P. Connolly, B. Gibbard, H. Gordon, R. Johnson,
S. Kahn, M. Month, M. Murtagh, S. Protopopescu, S. Terada,
D. Weygand, D. H. White, and P. Yamin
Brookhaven National Laboratory

D. Cutts, J. Hoftun, R. Lanou, and T. Shinkawa
Brown University

P. Franzini, D. Son, P. M. Tuts, and S. Youssef
Columbia University

C. Brown, B. Cox, C. Crawford, R. Dixon, H. Fenker, D. Finley,
D. Green, H. Haggerty, M. Harrison, H. Jostlein, E. Malamud,
P. Martin, P. Mazur, J. McCarthy, and R. Yamada
Fermi National Accelerator Laboratory

H. Goldman
Florida State University

S. Kunori and P. Rapp
University of Maryland

M. Abolins, R. Brock, D. Edmonds, D. Owen,
B. Pope, S. Stampke, and H. Weerts
Michigan State University

D. Buchholtz and B. Gobbi
Northwestern University

E. Gardella, W. Kononenko, W. Selove, G. Theodosiou, and R. Van Berg
University of Pennsylvania

M. Adams, R. Butz, R. Engelmann, G. Finocchiaro, L. Godfrey,
P. Grannis, D. Hedin, J. Horstkotte, J. Kirz, J. Lee-Franzini,
S. Linn, D. Lloyd-Owen, M. Marx, R. McCarthy, L. Romero,
R. D. Schamberger, and H. Weisberg
State University of New York at Stony Brook

and

J. Ficenec
Virginia Polytechnic Institute

TABLE OF CONTENTS

1. INTRODUCTION

The experiment described in this report had its origins in a series of proposals presented to the Fermilab PAC from February 1982 through June 1983, responding to a call for ideas for experiments at the D0 intersection region of TeV I. Over this period, the scale of the proposals tended to grow as the suggested size parameters for the collision hall were revised. In the last round, there was a set of proposals which focussed upon the physics of large transverse momentum or small distance scales. These proposals differed in detail in their stress upon lepton, hadron jet, or missing energy signatures. Different compromises were made on angular coverage, energy resolution, use of magnetic fields and stress upon forward versus central production of particles.

In June 1983, the PAC recommended to the lab director a somewhat unusual compromise solution to the question of choice of proposal. All proposed experiments were rejected. As accepted by Lederman, Phase I approval was given to a new project for D0 (see Fig. 1.1) in which a project manager was named (Grannis) and certain detector criteria were enunciated. These criteria can be summarized as follows:

1. Electromagnetic energy resolution at the level of $\sigma/E = 0.05/\sqrt{E}$ with good π-e separation.
2. Muon momentum resolution of approximately 20%.
3. Hadron energy resolution of about $\sigma/E = 0.8/\sqrt{E}$.
4. Good solid angle coverage for control of missing energy resolution.
5. A reasonable approximation of projective geometry in the calorimetry, with good segmentation.

Beginning in July, a collaboration was assembled, including many of the proponents of earlier D0 proposals as well as other physicists. Meetings to

discuss the design of the detector began in late July; from the outset, the criteria given by the PAC were felt to be useful goals for an experiment. The opinion of the collaboration was that, given the existing UA1 and UA2 experiments and the CDF detector under construction, we should focus to some degree upon a detector that could most usefully complement these efforts. In particular, we believe that an enhanced capability for lepton detection (electrons, muons, and neutrinos) would enable a rich and varied collection of investigations, not possible in the other detectors. Our general aim then has been to design a detector which identifies the presence of leptons over nearly full solid angle, even in the presence of nearby tracks from hadronic jets. We have aimed for quite fine segmentation of good hadron calorimetry, both because of the benefit in identifying jets and because of its influence upon missing p_T resolution.

The design presented here has emerged as the best choice for our goals only quite recently. It is based upon a choice, for both electromagnetic and hadronic calorimetry, of uranium liquid-argon systems. These calorimeters are then surrounded by magnetized iron toroids for muon detection. Owing to the short time available for preparation of this report, our aim has been to find an acceptable solution to the problems of detector design. In so doing, we have uncovered a variety of questions which clearly require more study before a final design can be made. The spirit of this report is then to give a single coherent statement of our proposed detector. We anticipate that such details as boundaries between major subdivisions of the detector, segmentation of calorimeter readouts, and precise arrangement of muon tracking chambers will continue to be fine tuned. Nevertheless, we anticipate that the properties of the final detector should remain relatively close to that described here.

In the ensuing description of the details of our detector, it will be clear that we have made some choices on how to meet the criteria established by the PAC. The ability to measure hadron energy and missing p_T will exceed the suggested specification by about a factor of two. Muon momentum measurement should be about 20%, as specified, with sign selection out to about 300 GeV/c. Segmentation, both transverse and longitudinal should be excellent, with a good approximation to projective geometry. The electromagnetic energy resolution will not be as good as set in the criteria; we anticipate $\sigma/E = A/\sqrt{E} + B$, with A = 10-12% and B < 1%. Compared with our estimate of achievable resolution using continuous sampling glass calorimetry, we argue that for electrons and photons above about 50 GeV/c, the uranium liquid-argon option should be better.

In summary, we are enthusiastic in proposing this design for an experiment which will attack the physics of 2 TeV in the center of mass. The capability of the detector is unique in many significant ways, and we are confident that in the most important area of searching for new phenomena at and above the vector boson mass scale it will be the best available. We are fully aware that the pressures of time and money are severe; the prospect for a most exciting physics program makes the effort worthwhile.

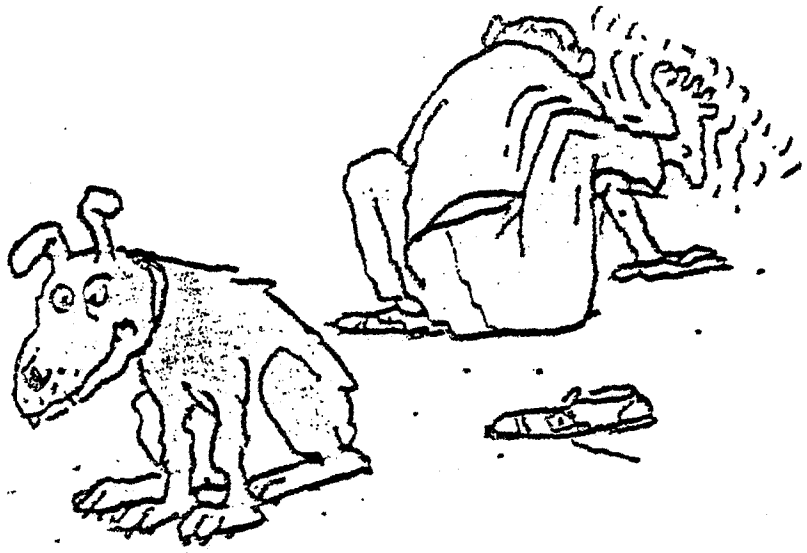

Fig. 1.1

2. PHYSICS AT DØ

The range of physics which can be addressed at TeV I is enormous and has been discussed at length in many reviews,[1] proposals[2]--and recently in terms of results from the CERN $Sp\bar{p}S$ Collider experiments. In this chapter, we give a selection of experimental questions which have focussed our thinking about an experiment at DØ, with particular emphasis on those which we feel can benefit from the strengths built into the DØ design. In presenting this list, we should bear in mind the likely direction of CERN $Sp\bar{p}S$ experiments prior to 1986 as well as the strong points of the CDF design for BØ.

The success of UA1 and UA2 in isolating the intermediate vector bosons now seems assured. The utility of good lepton identification and energy measurement, together with a hadron calorimeter capable of resolving jets and inferring the presence of missing transverse energy has been amply demonstrated. The CERN program will continue over the next few years and upgrades of the two major detectors are likely. Making the assumption[3] that the mean luminosity of $Sp\bar{p}S$ will be 5×10^{29} $cm^{-2}sec^{-1}$ over the next three years and that the experimental live time will be 1.6×10^{7} sec, leads to the expectation of about 200 $Z^0 \to e^+e^-$ events and 2000 $W^{\pm} \to e^{\pm}\nu$ events. Plans to raise the energy to 630 GeV are being made which should increase the cross sections by about 30%. With event samples of this order it is clear that many of the main features of W and Z should be well established by 1986. In particular, we may expect that the W mass will be measured to within about 0.3 GeV and the Z-W mass difference to within 0.8 GeV. The V,A structure of the charged current should be clearly manifest in the W-decay asymmetry. Jet physics should be well studied out to p_T = 200 GeV/c, yielding cross sections, angular distributions, fragmentation functions, and multijet to two-jet ratios. The searches for the top quark in $W \to t\bar{b}$ or diffractive Λ_t production may well prove

successful. Identification of a two-jet invariant mass peak at the W mass will be attempted, although the current detectors may have problems in these studies for both physics and instrumental reasons.

In the face of these expected results from CERN, it is useful to re-examine the program of physics that can be anticipated at TeV I. The general situation is that the standard model has been enormously successful thus far; no perceivable departures from its predictions are sensible in the present data. However, much of the theoretical literature of the past several years has focussed on the necessity of augmenting the standard model in some way. Although the popular notions on how to complete the picture may be wrong, it is useful to note that almost all such models postulate observable new phenomena emerging in the mass region $100 \leq m \leq 500$ GeV/c^2--or in deviations from orthodoxy in W and Z parameters at the level of radiative corrections. Thus the role of experiments at TeV I will be, in our view, to search for evidence of these new ingredients. The combination of good luminosity and high energy should combine to give marked improvement in our ability to find such new phenomena. The fact that the mass scale accessible will be well into the region where new states are predicted to exist should make TeV I a premier search machine.

In the discussion of specific topics below, we shall assume a standard run to be four months of running with 50% efficiency, at $\mathcal{L} = 10^{30}$ cm^{-2}sec^{-1} ($\int \mathcal{L} dt = 5\times10^{36}$ cm^{-2} = 5 pb^{-1}). Given the cross section in Fig. 2.1,[4] one expects about 1500 $Z^0 \to e^+e^-$ (and as many $Z^0 \to \mu^+\mu^-$), depending on the scaling violations assumed, and about 15,000 $W^\pm \to e^\pm\nu$ (and also $W^\pm \to \mu^\pm\nu$). Thus even for standard studies of the W and Z, the improvement in statistical error could be nearly a factor of three, compared with the integrated running of the CERN collider up to 1986.

2.1. PRECISION TESTS IN THE INTERMEDIATE BOSON SECTOR

2.1.1 Z and W Mass Measurements

A measurement of particular interest, accessible only in hadron machines until LEP II, is the mass ratio of W and Z. The measured masses, m_W and m_Z can be used to determine

$$\sin\theta_W = \frac{38.5\ \text{GeV}}{m_W},$$

and

$$\rho = \frac{m_W^2}{m_Z^2 \cos^2\theta_w}.$$

The mass of the Z^0 can be best measured via the decay $Z \to e^+e^-$. Simulations indicate an error δm_Z of less than 50 MeV from statistical sources alone. However m_W cannot be measured directly by this method so the precision in m_Z is less useful. An interesting method which can be employed for both m_W and m_Z has been suggested[5]; it employs the distribution in the transverse mass constructed from the p_T for an observed lepton and an inferred neutrino,

$$m_T^2 = 2E_T^{\ell} E_T^{\nu} (1 - \cos\theta_{\ell\nu}),$$

where E_T^{ℓ} is the transverse energy of e or μ, E_T^{ν} is the missing transverse energy in the event (after ignoring the second charged lepton in the case of the $Z^0 \to \ell^+\ell^-$), and $\theta_{\ell\nu}$ is the angle in the transverse plane between the two. Figure 2.2 shows the expected m_T distribution for the W under two extreme assumptions on the p_T for the W. The Jacobian peak near $m_T = m_W$ is quite pronounced and is largely insensitive to the p_T of the W.[6] The dominant effects in smearing this peak are the physical width of the boson and the

resolution in missing E_T. A study[6] of this method, using missing E_T resolutions appropriate to UA1 ($\delta E_T = 0.6\sqrt{\Sigma E_T}$) indicates mass errors δm_W = 80 MeV and δm_Z = 250 MeV, for decays involving electrons. The corresponding muon decays would yield errors about twice as large if muon momenta were measured to within 20%. (The missing E_T resolution is dominated in a hermetic detector like UA1 by hadron energy resolution; improvement in that resolution is expected to yield proportional gains in missing E_T resolution.)

Given these mass measurements of the W, the value of $\sin^2\theta_w$ can be determined with statistical precision of ±0.0005, so systematic effects must obviously be considered. Theoretical uncertainties in the radiative correction (itself about 6% of m_W) will also be present. The major systematic error here is in the energy scale for electrons. In principle, this can be calibrated through the Z^0 mass measurement and comparison with the e^+e^- determination of m_Z. This should give control of systematic errors on m_W to within 0.5% and thus an error on $\sin^2\theta_w$ of about 0.0025. Such a measurement would be most useful, both in comparing against theoretical values from Grand Unified Theories and with low energy measurements from neutrino scattering.

The measurement of the ρ parameter is a direct look at possible new ingredients in the standard model.[7] For the standard model without modification, ρ = 1. New states (heavy quarks, Higgs, Technicolor bosons, etc.) modify the value of ρ if present. Measurement of m_W and m_Z by the same method in the same experiment should give a nearly systematic free measurement of ρ to a precision of about 0.005. This, for example, would translate into an upper bound on the t-quark mass of about 130 GeV[8] if only Standard Model ingredients were present.

2.1.2 Z and W Width Measurements

Measurement of Γ_Z has been identified as being of particular interest due to its sensitivity to extra generations of light neutrino pairs. Cosmological constraints[9] suggest an upper bound on light neutrino generations of 3 or 4. The current limit on N_ν is about 50, based on an upper limit to the Z^0 width.[10] With high statistics and good electromagnetic energy resolution, considerable improvement can be made. Figure 2.3 shows the e^+e^- invariant mass distribution for $Z \rightarrow e^+e^-$, assuming $\Gamma_Z = 3$ GeV and electron energy resolutions appropriate to this proposal and to CDF.

A study of the precision in measuring Γ_Z was undertaken for an earlier DO proposal.[11] This study used an ensemble of Monte Carlo experiments measuring $Z \rightarrow e^+e^-$ with variable energy resolutions and event sample sizes. The error on Γ_Z was found to be well fitted by

$$\delta\Gamma_Z = \left(\frac{2}{N}\right)^{1/2} \sqrt{\Gamma^2_Z + (2.35\sigma_m)^2} \ ,$$

when N = number of events and σ_m = mass resolution. Figure 2.4 shows $\delta\Gamma_Z$ versus N for different mass resolutions and indicates that with the good energy resolution of this proposal, a sample of 1500 events should yield an error of 130 MeV/c^2.

The expected contribution to Γ_Z from each additional neutrino pair is 181 MeV/c^2. Theoretical uncertainties exist, both in the size of radiative corrections (these are estimated to be small[7]) and due to lack of knowledge of the t-quark mass. The latter uncertainty is small if the t-quark is found or is heavier than 40 GeV/c^2.

An interesting measurement, accessible only in hadron colliders at present, is a direct comparison of Γ_W and Γ_Z. The method is again to study

the m_T distribution described in 2.1.1. Figure 2.5 shows the calculated[6] m_T distribution for three different values of Γ_W. The measurement of the m_T distribution places a particular premium on missing E_T resolution. A study[6] of the errors on Γ_W using the measured UA1 missing E_T resolution gives, for our sample, $\delta\Gamma_W$ = 200 MeV. This experiment, with its improved hadron energy resolution, should do better than this. Taken in conjunction with the measurement of Γ_Z, we estimate an error on (Γ_W/Γ_Z) of 8%. Measurement of both widths offers the interesting possibility of testing for the effect of QCD radiative corrections. The W has no decays into a new lepton pair generation if the charged lepton is heavier than the W. Its sensitivity to the t-quark mass is less than for the Z width. Measurement of Γ_W to within 200 MeV may well help limit the range of accessible values for m_t since the expected contribution to Γ_W from each (low mass) quark pair is 800 MeV.

2.1.3 Search for Narrow States

Recently there have been indications of an unexpectedly large branching ratio for $Z^0 \to e^+e^-\gamma$ (and one event of $Z^0 \to \mu^+\mu^-\gamma$) from UA1 and UA2. The data themselves are insufficient to draw conclusions, but calculations of the probability for radiative effects are too small by nearly two orders of magnitude to explain these events. The interesting possibility exists that there is a decay mode $Z \to X\gamma$; $X \to \ell^+\ell^-$. With the good EM energy resolution of the DO detector, the invariant mass resolution for two or three particle combinations will be better than for UA1, UA2, or the CDF detector. If such a signal does indeed exist, it will be most interesting to search for the companion decay, $W \to e\nu\gamma$; again, good EM energy resolution will be at a premium.

A useful supplement to these searches will be examination of the muonic analogs. Here the DO detector has the unique possibility of triggering on

muons over the full solid angle. Should these radiative decays exist, comparison of electron and muon rates is essential to disentangle the physical mechanism.

An additional requirement for these searches is the ability to distinguish γ from π^0. The observed events have quite energetic γ candidates (tens of GeV). At these energies, unambiguous identification of γ versus π^0 is virtually impossible by looking for separated γ showers. The DO detector, with its fine-grained longitudinal segmentation, does offer a good statistical measure for distinguishing 1, 2, or multigamma showers.

Searches for new quarkonium states ($t\bar{t}$) are also aided by the very good mass resolution of the DO detector. Our estimates give sensitivity to a potential ($t\bar{t}$) state up to masses of 55 GeV/c^2 (thirty events over a small background). In this calculation we have used the ansatz of Gaisser scaling[12] and scaling functions determined from ISR data.[13,14]

2.1.4 Decay Asymmetry in $W^{\pm}$ Production and Decay

It is well understood[15] that the combined asymmetry of production of W^+ and W^- (the W^- tends to follow the incident $\bar{p}$) and V-A asymmetry in decay (charged leptons are anticorrelated with the W momentum) yields a sizable asymmetry in ℓ^+/ℓ^- production from W decay. This asymmetry, expressed in terms of the decay angle, θ^*, of ℓ^- from W^- in the W rest frame measured with respect to the proton beam direction, is expected to be $(1 + \cos\theta^*)^2$. The UA1 experiment reports[16] good agreement with this finding and gives $\langle\cos\theta^*\rangle = 0.4 \pm 0.1$. Given our sample of $W^{\pm} \rightarrow \mu^{\pm}\nu$ with sign-selected muons, we can expect an error on $\langle\cos\theta^*\rangle$ of less than 1%.

The potentiality that heavy W's or Z's exist reinforces the desire to measure the decay muon asymmetry over the full solid angle. Such heavy bosons could have a range of possible decay couplings, resulting in arbitrary asymmetries. This possibility suggests that the experiment retain good muon sign determination out to the maximum p_T values where cross sections allow heavy W', Z' production to be seen [i.e., for $p_T(\mu) \lesssim 150$ GeV/c].

Clearly the premium on detector capability here is upon good muon identification at large p_T. Decay backgrounds from π and K decay can be expected to be small ($h/\mu < 10^{-3}$ for $p_T > 30$ GeV/c). The dominant background will likely be hadron punchthrough; this component will be minimized using a relatively thick muon filter. In the case of $W \to \mu\nu$, the muon is expected to be relatively isolated and balanced in the transverse plane by missing p_T. Studies for earlier proposals[11,17] have shown that a rejection factor of about 100:1 can be achieved from these two criteria; these studies use the topological properties of background jet events embodied in the ISAJET Monte Carlo program.[18]

2.1.5 Search for the Gauge Boson Coupling

Measurement of associated production of gauge bosons would be extremely interesting, as it would reveal the character of the boson self couplings. These trilinear couplings are exactly specified in the standard model.[19] The largest of these reactions is expected to be $\bar{p}p \to W^{\pm}\gamma X$ for which the cross section is calculated[19] to be about 350 pb^{-1} (for the sum of both charges). The distribution of the angle θ_γ of the γ with respect to the $\bar{p}$ in the center of mass has a very pronounced dip at $\cos\theta_\gamma = -0.33$ in the standard model. Both cross-section magnitude and angular distribution are affected if the

standard model constraints are removed. Figure 2.6 shows the effect of altering the effective coupling on the angular distributions.

The detection of associated $W^{\pm}\gamma$ production is most straightforward if one demands the decay $W \to \ell\nu$ (ℓ = e or μ). The photon must be required to carry some minimum transverse momentum. Assuming $p_T(\gamma) > 10$ GeV/c, and standard W branching ratios yields[20] a reduction in observable signal of approximately 0.017 if one uses both e and μ. The resulting sample of $W^{\pm}(\ell\nu) + \gamma$ events in our luminosity interval is then about 20.

This small signal exists in a background from $W^{\pm}$ + jet events which is estimated[20] to be about 200 times larger. This background can be considerably reduced, first by requiring the γ candidate to be relatively isolated from other particles and secondly by applying cuts which reject 2γ showers relative to single γ.

Clearly, the size of the event sample is too small to measure detailed properties of the angular distribution. However, the cross sections computed in the standard model depend upon a particular cancellation of diagrams involving quark exchange and the gauge coupling. Removal of these constraints would result in a larger cross section. While a small deviation in the cross section would be hard to measure, a large deviation would signal a significant violation of the standard model.

Other potential searches exist which may prove of interest. A few events of the type $\bar{p}p \to W^{+}W^{-}X$, with one $W \to \ell\nu$ and the other $W \to$ 2 jet, should exist in our sample. Good lepton identification and jet-mass resolution are essential. The production of $Z^0\gamma$, expected to be unobservably small in the standard model, could be enhanced if the Z^0 were composite.

2.1.6 W, Z Production

The detailed measurement of W and Z production cross sections yield interesting results. The standard picture of the boson production involves a nearly identical process as for Drell Yan production of lepton pairs. For TeV I, the scaling variable $\sqrt{\tau} = m/\sqrt{s} \simeq 0.045$, is smaller than can be reliably probed at lower energies. It is precisely this region where the QCD non-scaling corrections are expected to enhance the cross section.

The x-dependence of W and Z production reveal the parton x-distribution in the same way as in Drell-Yan production. Comparison of W and Z distributions offer the possibility to probe differences in the structure functions for u, d and sea quarks.

The p_T distribution of produced bosons is interesting for a study of radiative processes in QCD. Early results from UA1[16] indicate the existence of $W^{\pm}$ + jet production in agreement with the idea that high p_T W's are made by initial state gluon radiation. We may expect that about 30 such W + jet and 6 Z^0 + jet events will exist in our standard sample for $p_T(\text{jet}) > 100$ GeV. The rate of such processes, as a function of $p_T(\text{jet})$ should allow extraction of useful information on $\alpha_s(q^2)$.

2.1.7 Quark Decays of W and Z

The decays of W and Z into quark pairs are well understood within the standard model (subject to a knowledge of the t-quark mass). Decays of W and Z into a pair of quark jets is in principle observable, if the QCD jet production backgrounds can be controlled. This study places a large premium upon good hadron energy measurement in order to reduce the error on jet invariant mass. Good segmentation of calorimetry is also desired.

Flavor tagging of jets can be accomplished in some circumstances. Quark semileptonic decays yield observable electrons and muons whose components of momentum parallel and perpendicular to the jet axis differ for different quark flavors. Ability to use these signatures demand good lepton identification in the presence of the remaining hadronic debris in the semileptonic decays. An explicit Monte Carlo study of $W^+ \to t\bar{b}$ is shown in Figs. 2.7 and 2.8. Although the QCD backgrounds exceed the signal by a factor of about 100, simple topological cuts can be found which reduce them below the signal, leaving useful numbers of signal events (150 events for m_t = 60 GeV).

2.2 HIGH p_T STUDIES OF QCD

2.2.1 Jet Production

The emergence of small angle clustering of energetic particles in UA2[21] and UA1[22] have dramatically confirmed the prediction of parton jets in hadron collisions. Many properties of these jets of $p_T \leq 200$ GeV/c have been studied including multiplicity distributions, energy flow, transverse momenta within the jets, angular distributions, and cross sections. The presence of three jet events has been established to be in rough agreement with QCD predictions. Hadronization distributions have been studied for a mixture of quark and gluon jets.

At TeV I, again assuming a run of 5 pb^{-1} and the expected QCD jet cross section,[23] we may expect to have jets up to 500 GeV/c. Extension of the measured properties to this smaller distance scale is of great interest in itself. Measurement of the ratio of three or more jets to two jets at very large p_T will enable measurement of the strong coupling constant at much larger q^2 than available elsewhere. Measurement of the p_T dependence of the jet cross section is an interesting place to look for effects of quark compositeness. A

recent calculation[24] suggests that compositeness that enters with a mass scale parameter of $\Lambda \sim 2$ TeV ($\sim 10^{-17}$ cm) can be sensed through a (non-scaling) deviation from lower p_T jet cross-section behavior. The major detector requirements for these jet studies are good hadronic energy resolution and good segmentation.

2.2.2 QED/QCD Ratio Tests

The ratio of single γ to single gluon production is sensitive to the ratio of coupling constants, α/α_s. At the CERN ISR and Fermilab, useful measurements of the γ/π^0 ratio have confirmed QCD expectations. These are roughly that the γ/π^0 ratio increases like $x_T = 2p_T/\sqrt{s}$, so one may expect $\gamma/\pi^0 = 0.05$ at $p_T = 50$ GeV/c. An explicit calculation[25] is shown in Fig. 2.9 which indicates appreciable rates of single γ out to $p_T = 50$ GeV/c. The related measurements of the ratios (jet + γ)/(2 jets) or (2 jets + γ)/(3 jets) contain even more direct information on the α/α_s ratio. Finally, it has been calculated[26] that a measurement of 2γ production at large invariant mass can give complementary information to the Drell-Yan dilepton production, with perhaps less background.

The measurement of single photons (as opposed to π^0, η, or ω) is a delicate experimental problem. Studies have shown[11] that in an electromagnetic calorimeter with fine longitudinal segmentation, it is possible to measure γ/π^0 to within a few percent in the presence of multigamma backgrounds, based upon the distribution of the depth of first conversion. Additional discrimination has been shown[27] to be given from detailed multilayer shower deposition correlations.

2.3 SEARCHES BEYOND THE STANDARD MODEL

The potential of TeV I, with high energy and good luminosity, is likely to be most fully realized in searching for new particles or phenomena at very high masses. Many such particle spectroscopies have been suggested and explored in the theoretical literature.[28] With luck, we may find that Nature is even more inventive. In any case, the known set of hypothetical objects possess interesting properties that can be used for a search with the detector proposed here.

2.3.1 Heavy Vector Bosons

A search for additional Z or W bosons can be performed in a similar manner to those that have led to discovery of the standard ones. The possibility that more bosons exist has been incorporated into several grand unification schemes. If one assumes the cross section scales in the usual manner,[20] one finds that the sensitivity for Z' should extend to $m \simeq 230$ GeV and to $m \simeq 150$ GeV for W'. For such searches, we may expect the background sources will be rather small and the main requirement of the experiment will be identification of electrons and muons over the largest possible solid angle. Measurement of the charge sign would be desirable for examination of asymmetries. The transverse momentum spectra of the decay leptons would be expected to peak at roughly m/2, setting the scale for the momentum resolution desired--namely good charge determination to at least 100 GeV/c.

2.3.2 Heavy Leptons

In the absence of any understanding of the number of fermion generations that may exist, it is natural to search for new leptons of mass larger than the current limits.[29] For new charged leptons, $L^{\pm}$ of the standard type (e, μ, τ...), the experimental signatures are well understood. Production of $L^{\pm}$ via the Drell Yan mechanism can occur, but at a rate that precludes detection for masses allowed by the current limits from e^+e^- machines. A more useful means of making $L^{\pm}$ lies in decays such as $W^{\pm} \to L^{\pm}\nu_L$ or $Z^0 \to L^+L^-$, providing the L masses are below the appropriate thresholds. In such a case, the number of $L^{\pm}$ produced is comparable to the number of electrons or muons from W and Z decay, inhibited only by a phase space factor.

The decays of $L^{\pm}$ are expected to proceed in the well understood manner[28]

$$B(L^{\pm} \to \ell^{\pm}\nu_{\ell}\nu_L) = 1/9 \text{ for } \ell = e, \mu, \text{ or } \tau$$
$$B(L^{\pm} \to \nu_L + \text{hadrons}) = 2/3,$$

providing that $m(\nu_L) < m(L^{\pm})$ and $m(L^{\pm}) < m_t$. The ingredients of a search then involve a combination of good lepton identification (e and μ), good missing p_T resolution (due to the presence of several neutrinos in the decays), and good hadron jet identification (for tagging the more prevalent hadronic decay modes of $L^{\pm}$). The decay asymmetry for the decay $W \to L\nu_L$ with $L \to \mu\nu_L\nu_{\mu}$ may also be a useful indicator of the presence of a heavy lepton for $m_L \leq 60$ GeV/c^2.[30]

The number of events of various types to be expected are summarized in Table 2.1. Typically the missing energy carried off by neutrinos in these events will be large, and the ratio of observable electron or muon energy to missing energy small, thus enabling some useful cuts to be made.

There also exists a possibility that heavy neutral leptons, L^0, may exist.[28] Such states may have appreciable two-body decay modes such as $L^0 \to \mu^{\pm}\pi^{\mp}$. With good lepton energy measurement and good hadron calorimetry, these two-body signatures, well isolated from jet-like activity, should be quite distinctive. Using the standard model estimate for the $Z^0 \to L^0\bar{L}^0$ branching ratio of 6% we expect of order 6000 L^0 and $\bar{L}^0$ produced. Taking the branching ratio of $L^0 \to \ell^{\pm}\pi^{\mp}$ of 3% (in analogy with $\tau^{\pm} \to \nu_{\tau}\pi^{\pm}$, with a mixing angle factor included) we then expect 360 cases of $L^0 \to \ell^{\pm}\pi^{\mp}$ with ℓ either electron or muon. The particularly interesting case $L^0 \to e^-\pi^+$ or $\to \mu^-\pi^+$ and $\bar{L}^0 \to e^+\pi^-$ or $\mu^+\pi^-$ would yield 10 events.

In the case of composite models, the possibility of excited leptons exists. Decays such as $e' \to e\gamma$ or $e' \to ee^+e^-$ would then occur and give useful signatures for detection. Good energy resolution and the ability to detect photons are of prime importance here.

2.3.3 Supersymmetry

In supersymmetry models,[30] all fermions acquire boson partners of identical quantum numbers, except for spin (and vice versa for the known bosons). These supersymmetric partners generally possess a common property that is conserved, implying that the lightest of them are absolutely stable (and very weakly interacting). The rational for supersymmetry is that it can be naturally incorporated into grand unified theories giving an explanation for the disparity between observed particle masses and the unification mass, and that such theories are relatively free from divergence difficulties. These powerful theoretical motivations are only slightly tarnished by the complete lack of any experimental sighting of a supersymmetric particle.

The phenomenological aspects of supersymmetry are confused by the large amount of flexibility in the mass scales and ordering of particles in that scale. However it is clear that if the ideas are correct, the counterparts of the gluon (gluino) and quarks (squarks) will be copiously produced in energetic hadronic collisions. Detection of such particles is limited only by the availability of sufficient energy to exceed the appropriate mass thresholds, and by the somewhat indirect means for identification of their decay products.

One of the most favorable cases for search is the reaction $\bar{p}p \rightarrow \tilde{g}\tilde{g}x$ ($\tilde{g}$ is gluino). This process has been studied in some detail[31] for a range of $\tilde{g}$ masses. Supersymmetry allows the cross sections to be calculated using standard QCD. The $\tilde{g}$ decays into $q\bar{q}\tilde{\gamma}$ ($\tilde{\gamma}$ is photino). The Monte Carlo study used detector parameters similar to that we propose. The essential features are good missing p_T resolution for sensitivity to the non-interacting $\tilde{\gamma}$ and good lepton identification. The latter feature is important for tagging the main source of background from heavy quark semileptonic decay in which neutrinos give the missing p_T and in which leptons are always present. Figure 2.10 shows the signal and background events as a function of the maximum "jet" p_T after application of cuts on p_T imbalance and lack of energetic leptons. A signal persists from $\tilde{g}$ production for $m_{\tilde{g}} \leq 100$ GeV/c^2.

Other detection strategies exist which utilize the four jet plus missing energy topology of the gluino pairs production. Since each quark jet in $\tilde{g} \rightarrow q\bar{q}\tilde{\gamma}$ carries on average one third of the gluino rest energy, it is imperative here to have a detector with good hadronic energy resolution and good segmentation.

Finally, it is possible[32] that the C noninvariant gluino decay $\tilde{g} \rightarrow g\tilde{\gamma}$ occurs with appreciable branching ratio. Such a decay mode is experimentally

simpler to isolate (two energetic jets plus large missing p_T). Again, the requirement on the detector is for superior hadron calorimetry.

2.3.4 Heavy Quarks

Another result of our uncertainty on the number of fermion generations (c.f. sections 2.1.2 and 2.3.2) is that we may expect to find additional quark species beyond the presently expected u, d, s, c, b, t. Assuming that the new flavor pair ha a combined mass above the W mass, it is impossible to produce them via $W \to Q_u \bar{Q}_d$. However, for $M_Q > M_W$, the dominant decay mode is $Q \to Wq$, where q is the next lighter quark. The final state for $p\bar{p} \to Q\bar{Q}$ production would then be $W^+W^- q\bar{q}$. The cross section[23] is such that a pair of 120 GeV/c^2 heavy quarks would yield 100 such events (in 5 pb^{-1}). Non-leptonic detection would require identification of W's through di-jet invariant masses in a six jet final state. This rather fanciful scenario would clearly push the hadron calorimetry to its limit! However if one W decays leptonically, the signature would be quite striking; finding it would require good detection of jets, leptons and missing p_T.

2.3.5 Technicolor

The technicolor models[33] were invented to give the Higgs bosons a firm position in gauge theories; this is accomplished with of a large number of new exotic objects. The properties of two of these appear to warrant a useful search in a 5 pb^{-1} run at TeV I. The first is the technicolor octet state, η_T, for which the mass estimate of 200-250 GeV/c^2 is fairly firm. Its decay is expected to be a pair of top quarks. Estimated prodction rates are large (of order 1000 events). A crude calculation[34] showed that with a high

resolution vertex chamber (σ = 20 μ), the η_T signal would survive above background with roughly 10% efficiency.

The second potentially observable technicolor states are the leptoquarks whose mass is estimated at 150 GeV/c^2. The decays would be a lepton and a quark jet. Pair production of leptoquarks should yield about 30 events in 5 pb^{-1} with rather distinctive final states (two isolated leptons and two heavy quark jets). It may even be possible to study lepto quark decays into t + τ, since the energetic τ yields its neutrinos along the lepton axis. Using the τ mass constraint one can infer their magnitude.

2.3.6 Quark-Gluon Plasma

Much theoretical work has been directed recently at the possible formation of new states of matter in very high-energy collisions. One such possible state is a quark-gluon plasma, which is expected to be formed at sufficiently high-energy density. Among the suggested signals for such a state of matter is an increase in the photon/hadron ratio at low-p_T values, resulting from the fact that photons can escape from the interior of a hot region of high-energy density more easily than hadrons can. It appears unlikely that exact predictions can be made as to whether such a plasma could be formed at the TeV I collider, or what the temperature would be if such a plasma were formed. However, if sufficiently accurate measurements can be made of the photon spectrum down to momenta as low as possible, one can investigate, purely experimentally, whether this spectrum changes with $\sqrt{s}$, or with general characteristics of the events such as multiplicity. Note that it is not necessary to develop thermal equilibrium in such a plasma in order to have a detectable effect. Nor is it necessary to form or observe a phase transition. The experimental sensitivity for observing an effect depends on how well one

can detect low-energy photons in an interesting energy range, and on how well one can measure the energy spectrum of such photons in events covering a large range of multiplicities.

Although it is not necessary to observe a phase transition in order to have an interesting signal, the theoretical estimate of the temperature at which such a transition might occur is pertinent in estimating what photon energies are of particular interest. The transition temperature is estimated to be of order 100-200 MeV.[35] The requirement on the detector then is that it be capable of identifying and measuring the energy of photons down to 100 MeV, even in events of abnormally high multiplicity.

2.3.7 Unexpected Objects

When searching in a new energy regime, it is important that we retain a sensitivity to phenomena which have not been foreseen by theory. Although it is rare that something completely unexpected turns up, such occurrences are often harbingers of a major change or advance in our understanding. Historical examples include the discovery of the τ, J/ψ, CP violation and the Υ.

In this sector one cannot test the performance of a detector against expected yields or signatures. Instead, we can only point to the general capabilities of the proposed experiment which may enable some interesting searches. Since the new phase space uncovered at TeV I is the very small distance scale ($\gtrsim 10^{-17}$ cm), we feel that emphasis upon good energy measurement and particle identification at the very largest transverse momenta are the key ingredients for a search for new physics. Our detector is designed to identify all five of the observable particles at the largest accessible p_T: electrons, muons, neutrinos, jets, and photons. Its solid angle coverage is virtually complete. Owing to its emphasis on calorimetry, fractional energy

resolutions will improve as energy increases. The detector is sufficiently simple and homogeneous that sensing the presence of new phenomena should be made more straightforward.

REFERENCES CHAPTER 2

1. See the many discussions in Proceedings of the 1982 DPF Summer Study on Elementary Particle Physics and Future Facilities, ed. R. Donaldson, R. Gustafson, and F. Paige; hereafter referred to as Snowmass 1982.

2. Design Report for the Fermilab Collider Detector Facility (CDF), August 1981. See also Fermilab proposals P714, P724, P726, and P728.

3. UA1 Upgrade Proposal, CERN-SPSC/83-48 August 1983.

4. F. Paige, BNL-27066.

5. W. L. van Neerven, J. A. M. Vermaseren, and K. J. F. Gaemers, NIKHEF-H/82-20a; V. Barger, A. D. Martin, and R. J. N. Phillips, DPT/83/2.

6. J. Smith, W. L. van Neerven, and J. A. M. Vermaseren, ITP-SB-83-11.

7. W. J. Marciano and Z. Parsa, Snowmass 1982, p. 155.

8. M. Veltmann, Nucl. Phys. **B123**, 89 (1977); M. Chanowitz, M. Furman, and I. Hinchliffe, Phys. Lett. **78B**, 285 (1978).

9. V. Shvartsman JETP Letters **9**, 184 (1969); G. Steigman, D. Schramm, and J. Gunn, Phys. Lett. **68B**, 202 (1977).

10. P. Bagnaia et al., Phys. Lett. **129B**, 130 (1983).

11. Fermilab Proposal P714 (LAPDOG) and Addenda.

12. T. Gaisser, F. Halzen, and E. A. Paschos, Phys. Rev. **D15**, 2572 (1977).

13. D. Antreasyan et al., Phys. Rev. Lett. **47**, 121 (1981).

14. C. Kourkemelis et al., Phys. Lett. **91B**, 481 (1980).

15. C. Quigg, Rev. Mod. Phys. **49**, 297 (1977).

16. G. Arnison et al., Phys. Lett. **129B**, 273 (1983).

17. Fermilab Proposal P728.

18. F. Paige and S. D. Protopopescu, BNL 29777 1981.

19. R. W. Brown, D. Sahdev, and K. O. Mikaelian, Phys. Rev. **D20**, 1164 (1979).

20. G. Bunce et al., Snowmass 1982, p. 489.

21. P. Bagnaia et al., CERN-EP/83-94 and CERN-EP/83-135.

22. G. Arnison et al., CERN-EP/83-118 and CERN-EP/83-119.

23. F. Paige, Snowmass 1982, p. 484.

24. E. Eichten, K. Lane, and M. Peskin, Phys. Rev. Lett. **50**, 811 (1983).

25. I. Hinchliffe and R. Kelly, LBL-12274.

26. F. Paige and I. Stumer, Proceedings of the 1981 Summer Workshop (ISABELLE), p. 479.

27. R. L. Engelmann et al., Nucl. Instrum. and Methods **216**, 45 (1983).

28. G. Kane and M. Perl, Snowmass 1982, p. 18.

29. S. Yamada, Proceedings of the 1983 International Symposium on Lepton Photon Interactions at High Energies, Cornell University, August 1983.

30. D. Cline and C. Rubbia, CERN-EP/83-61.

31. S. Aronson et al., Snowmass 1982, p. 505; L. Littenberg, BNL preprint and private communication.

32. G. Kane and H. Haber, UM-TH 83-18.

33. E. Farhi and L. Susskind, Phys. Rept. **74C**, 277 (1981).

34. C. Baltay and H. Gordon, Snowmass 1982, p. 500.

35. M. Jacob and J. Tran Thanh Van, Phys. Rept. **88C**, 321 (1982).

TABLE 2.1

Decay Chain	B. R.	Events	Signature
$W \to L\nu_L$	1/12		mean $p_T(\ell) \sim 10$ GeV;
$L \to \ell \nu_L \nu_\ell$	1/9	1650	large missing p_T;
(ℓ = e or μ)			no hadron jets
$Z \to L^+L^-$	1/30	75	two moderate p_T leptons;
$L^+ \to \ell^{+-} \nu_L \nu_\ell$	1/9	(sum of e and μ)	large acoplanarity and
$L^- \to \ell^- \nu_L \bar{\nu}_\ell$	1/9		missing energy
(ℓ = e or μ)			
$Z \to L^+L^-$	1/30	220	moderate p_T lepton,
$L^+ \to \ell^{+-} \nu_L \nu_\ell$	1/9	(sum of e and μ)	acoplanar with single
$L^- \to \nu_L$+hadrons	2/3		hadron jet. Large
			missing energy.

FIGURE CAPTIONS - CHAPTER 2

2.1 Cross sections from Ref. 4 for $W^{\pm}$ and Z^0 versus energy.

2.2 Distribution of events with transverse mass, m_T, for $W \to e\nu$, from Ref. 6. The solid line assumes $p_T^W = 0$; The dashed line is for $p_T^W = 50$ GeV/c.

2.3 Mass distribution for e^+e^- from Z^0, with no resolution smearing and the finite resolution appropriate for this experiment ($\sigma_M = 1.19$ GeV) and for CDF ($\sigma_M = 2.25$ GeV).

2.4 Error on Z^0 width versus number of events using the mass resolution of this proposal ($\sigma_M = 1.19$ GeV).

2.5 Distribution of events with transverse mass for $W \to e\nu$ with $\Gamma_W = 1$ GeV (dashed), 2.5 GeV (solid), and 5 GeV (dot-dashed).

2.6 Distribution of events with $\cos\theta$, where θ is the angle of the γ with respect to the $\bar{p}$ direction in $pp \to W^{\pm}\gamma x$. The parameter K is related to the gauge coupling and has value 1 in the Standard Model.

2.7 (a) Distribution of events versus E_T for the electron in $t \to be\nu$; $\Delta: m_t$ = 30 GeV, $\cdot: m_t$ = 60 GeV. The points (x) are backgrounds from QCD jets.

(b) Transverse mass, m_T, distributions for $t \to be\nu$ and QCD jet backgrounds.

Detector resolutions have been folded in and a cut E_T (electron) > 5 GeV imposed.

2.8 Distribution of events for $t \to be\nu$ and background (shaded bands) after cuts on an isolated electron, E_T (electron) > 10 GeV, and E_T (missing) > 10 GeV.

2.9 Cross section for single π^0 and γ production versus p_T from Ref. 25.

2.10 Gluino cross section for various gluino masses. The backgrounds shown after missing p_T cuts, with and without lepton veto cuts.

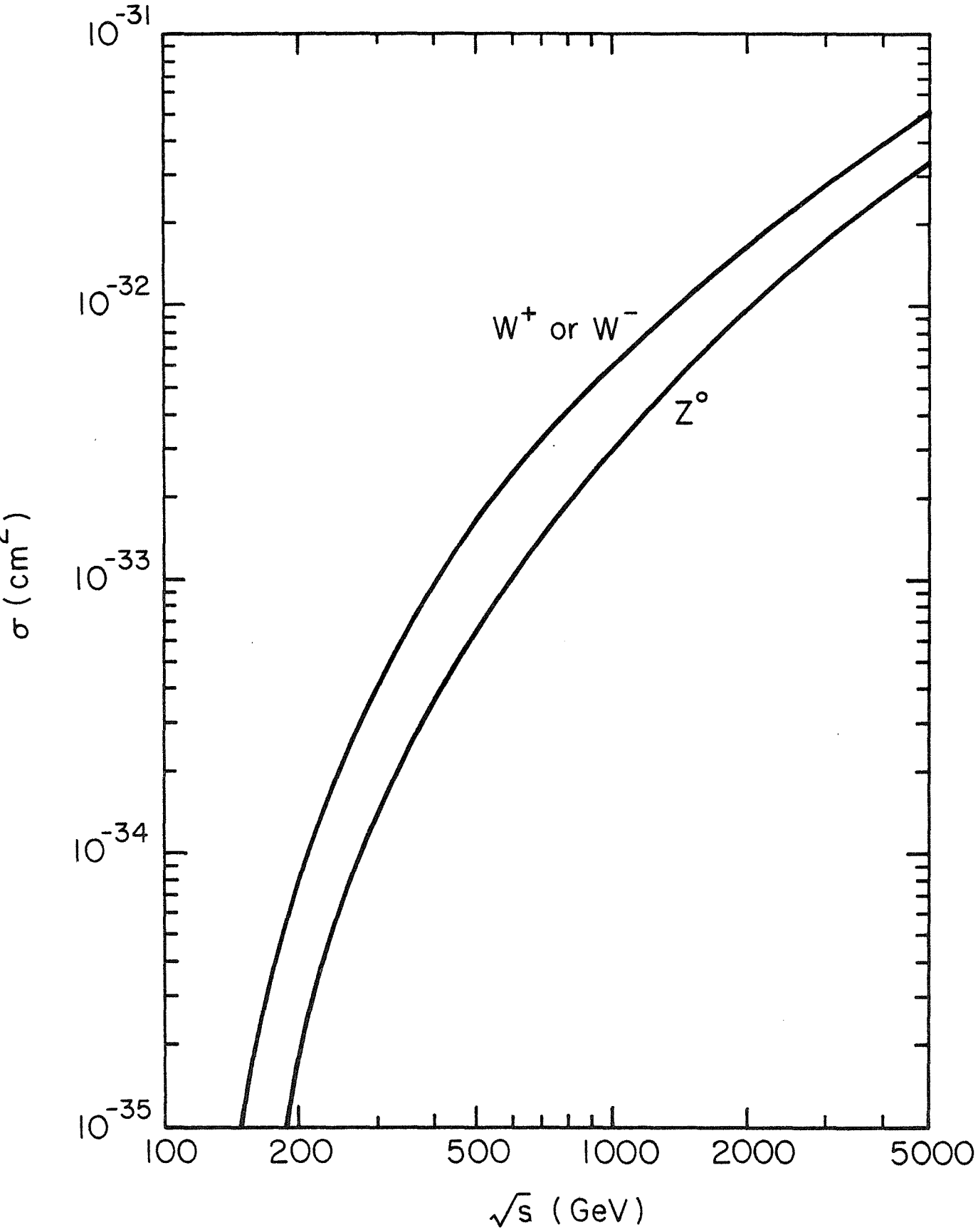
10^{-31}
10^{-32}
10^{-33}
10^{-34}
10^{-35}
σ (cm^2)
W^+ or W^-
Z°
100
200
500
1000
2000
5000
$\sqrt{s}$ (GeV)

Fig. 2.1

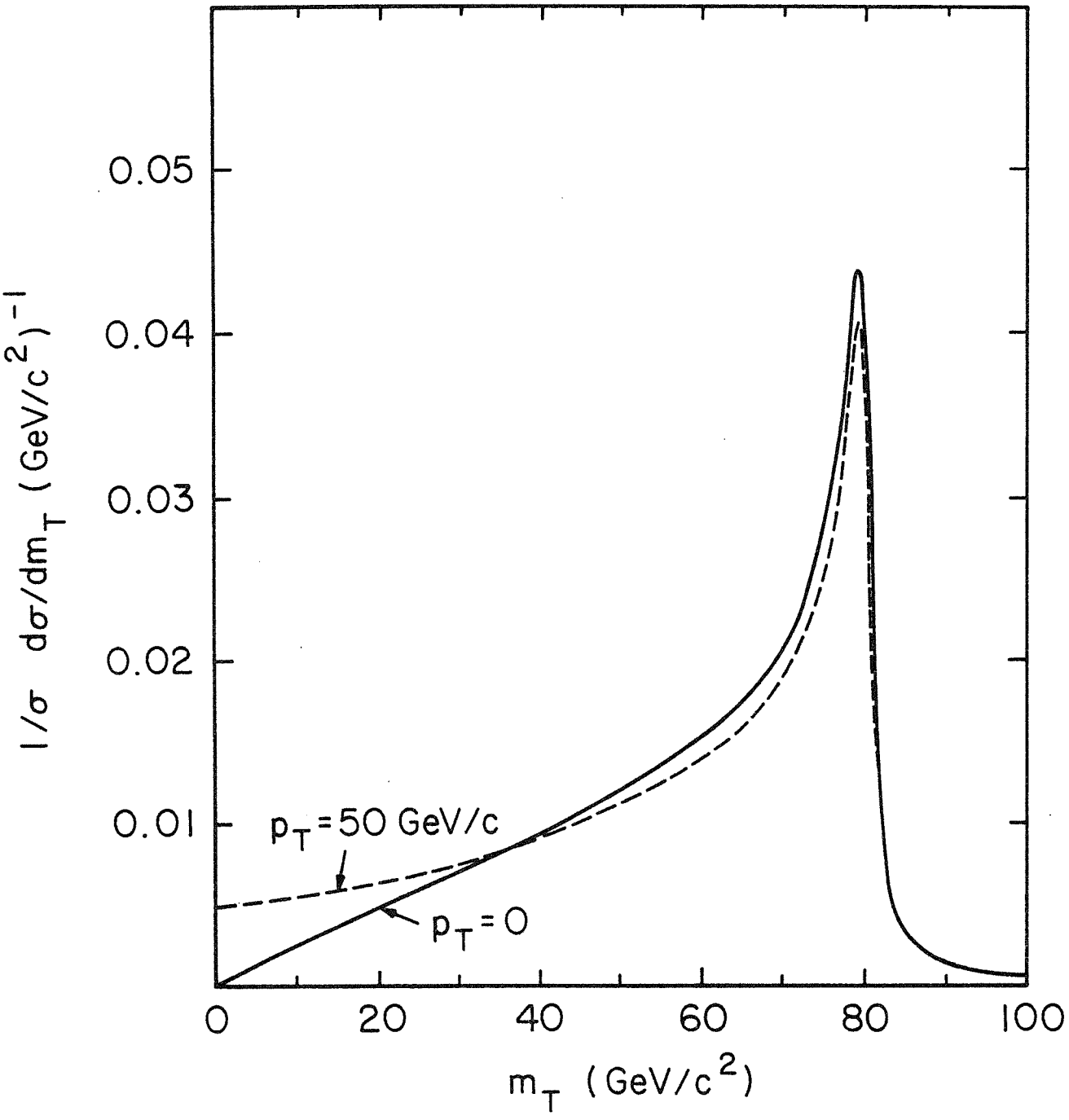
0.05
0.04
0.03
0.02
0.01
$1/\sigma \; d\sigma/dm_T \; (GeV/c^2)^{-1}$
$p_T = 50$ GeV/c
$p_T = 0$
0
20
40
60
80
100
m_T (GeV/c^2)

Fig. 2.2

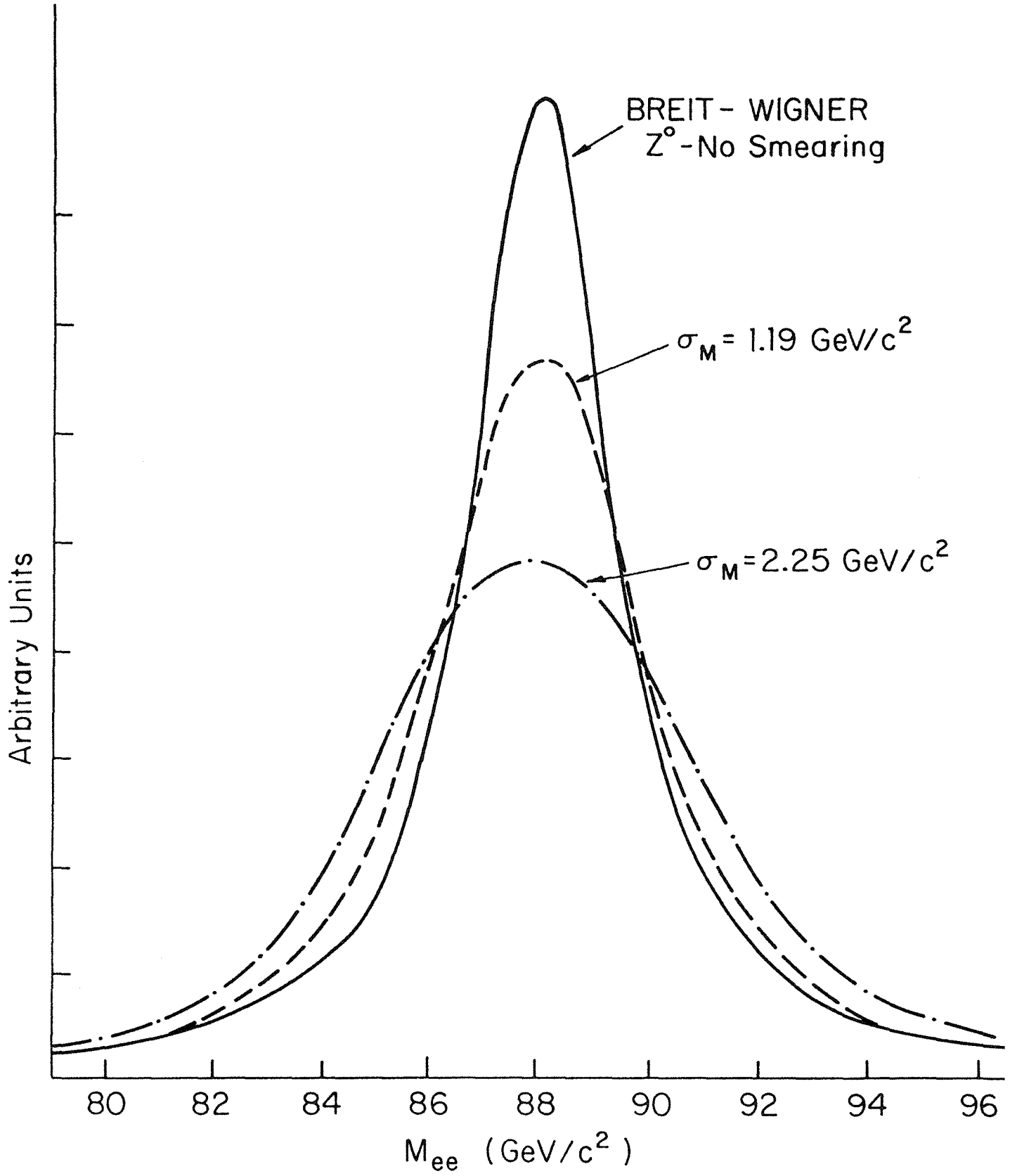
BREIT - WIGNER
Z° - No Smearing
σ_M = 1.19 GeV/c^2
σ_M = 2.25 GeV/c^2
Arbitrary Units
80
82
84
86
88
90
92
94
96
M_{ee} (GeV/c^2)

Fig. 2.3

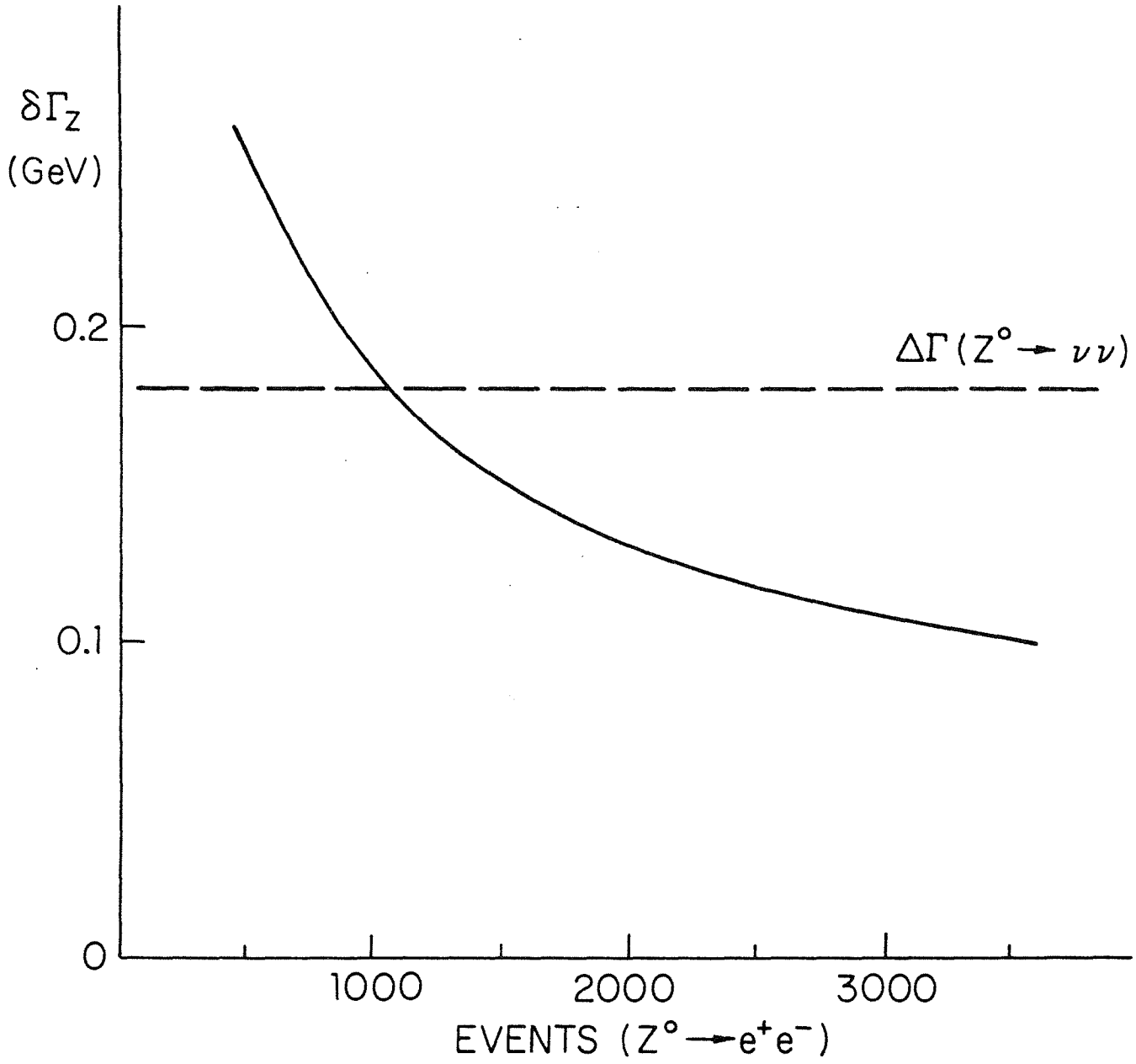
$\delta\Gamma_Z$
(GeV)
0.2
0.1
0
$\Delta\Gamma(Z^\circ \rightarrow \nu\nu)$
1000
2000
3000
EVENTS ($Z^\circ \rightarrow e^+e^-$)

Fig. 2.4

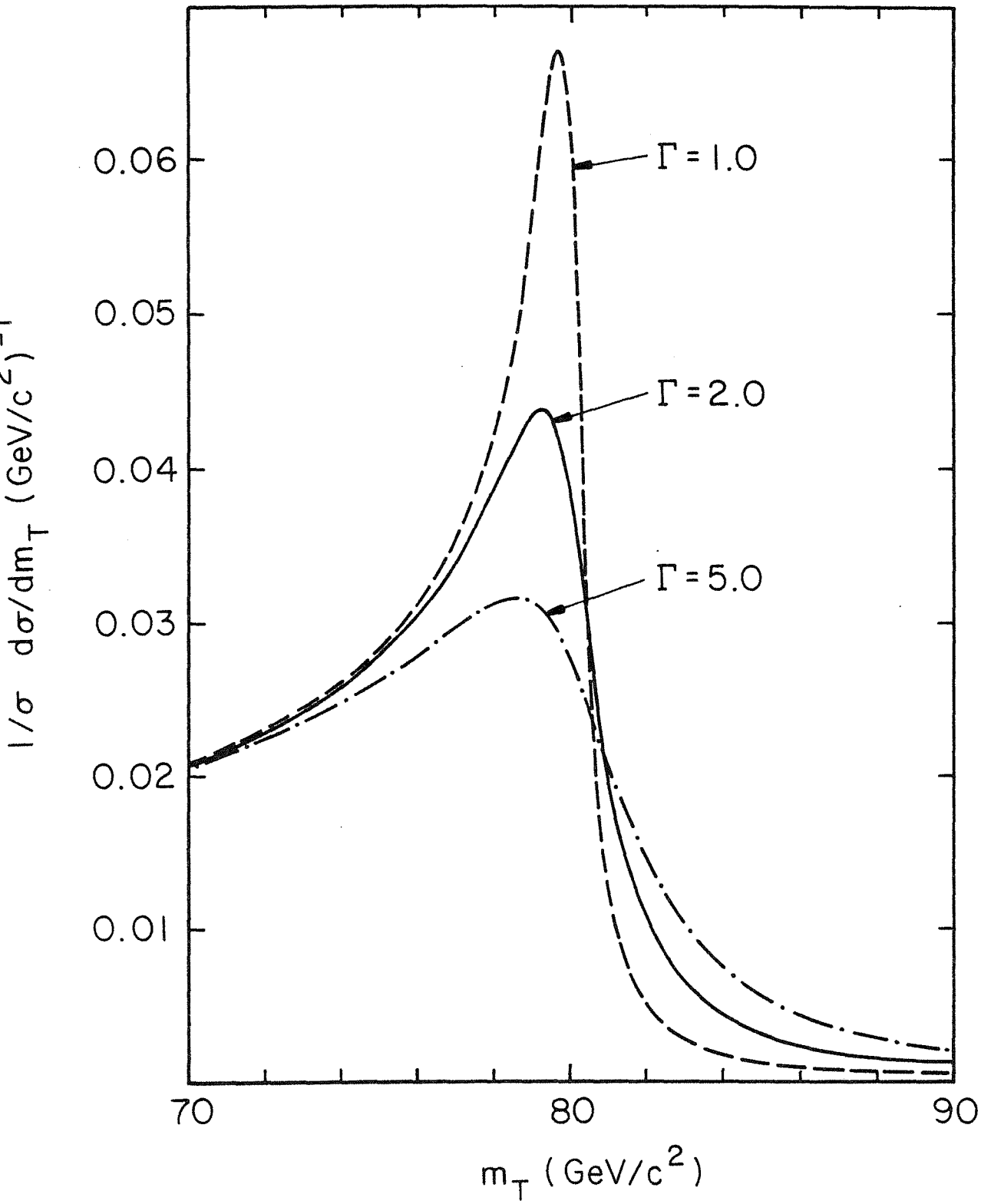
0.06
0.05
0.04
0.03
0.02
0.01
Γ = 1.0
Γ = 2.0
Γ = 5.0
1/σ dσ/dm_T (GeV/c²)⁻¹
70
80
90
m_T (GeV/c²)

Fig. 2.5

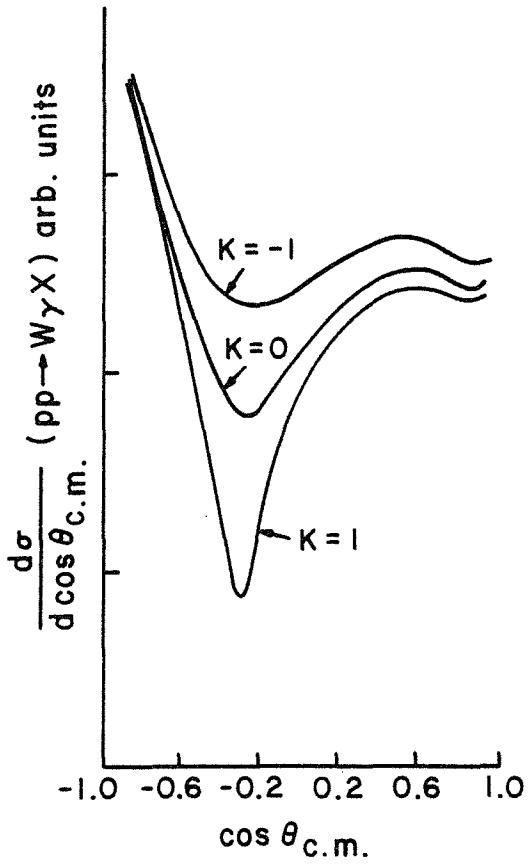
$\frac{d\sigma}{d\cos\theta_{c.m.}}$ (pp→WγX) arb. units
K = -1
K = 0
K = 1
-1.0
-0.6
-0.2
0.2
0.6
1.0
cos $\theta_{c.m.}$

Fig. 2.6

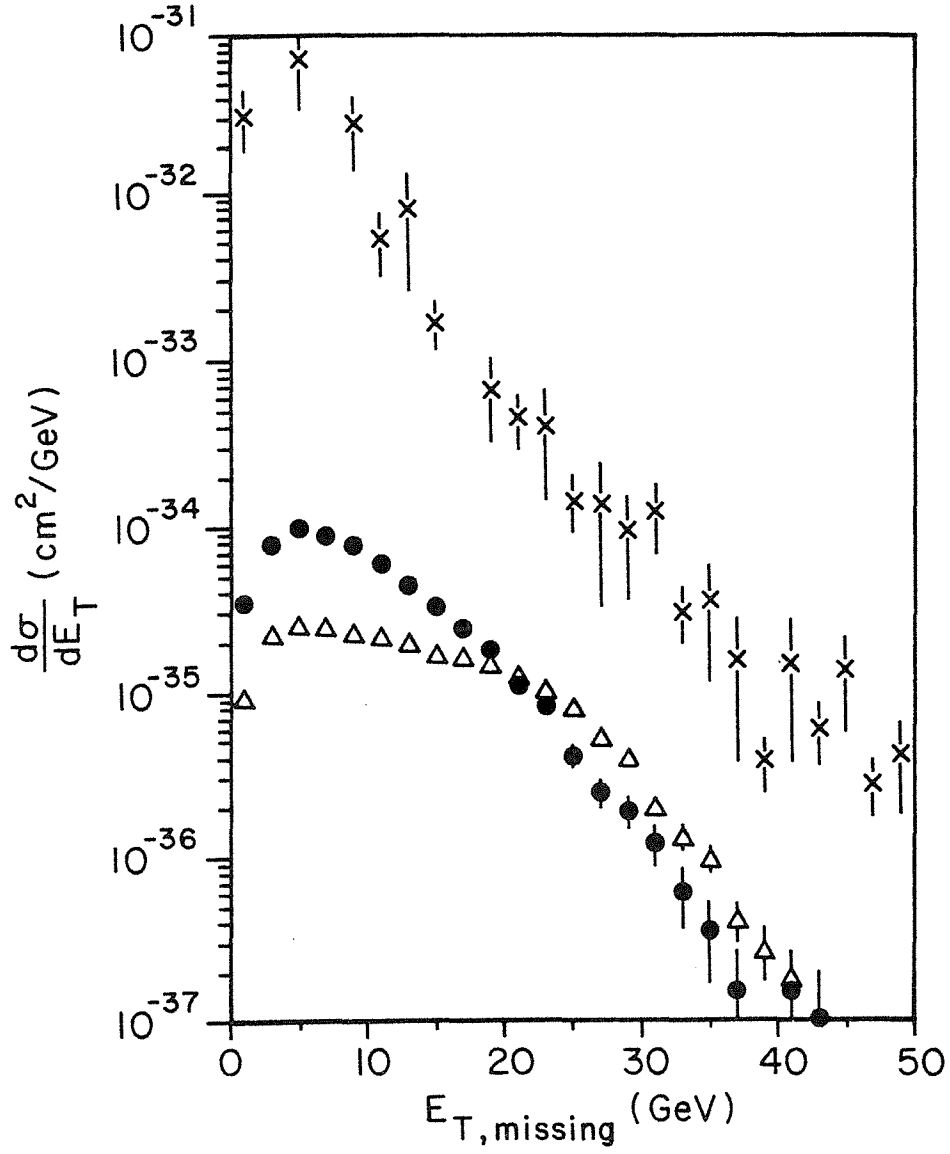
10^{-31}
10^{-32}
10^{-33}
10^{-34}
10^{-35}
10^{-36}
10^{-37}
$\frac{d\sigma}{dE_T}$ (cm^2/GeV)
0
10
20
30
40
50
$E_{T,missing}$ (GeV)

Fig. 2.7a

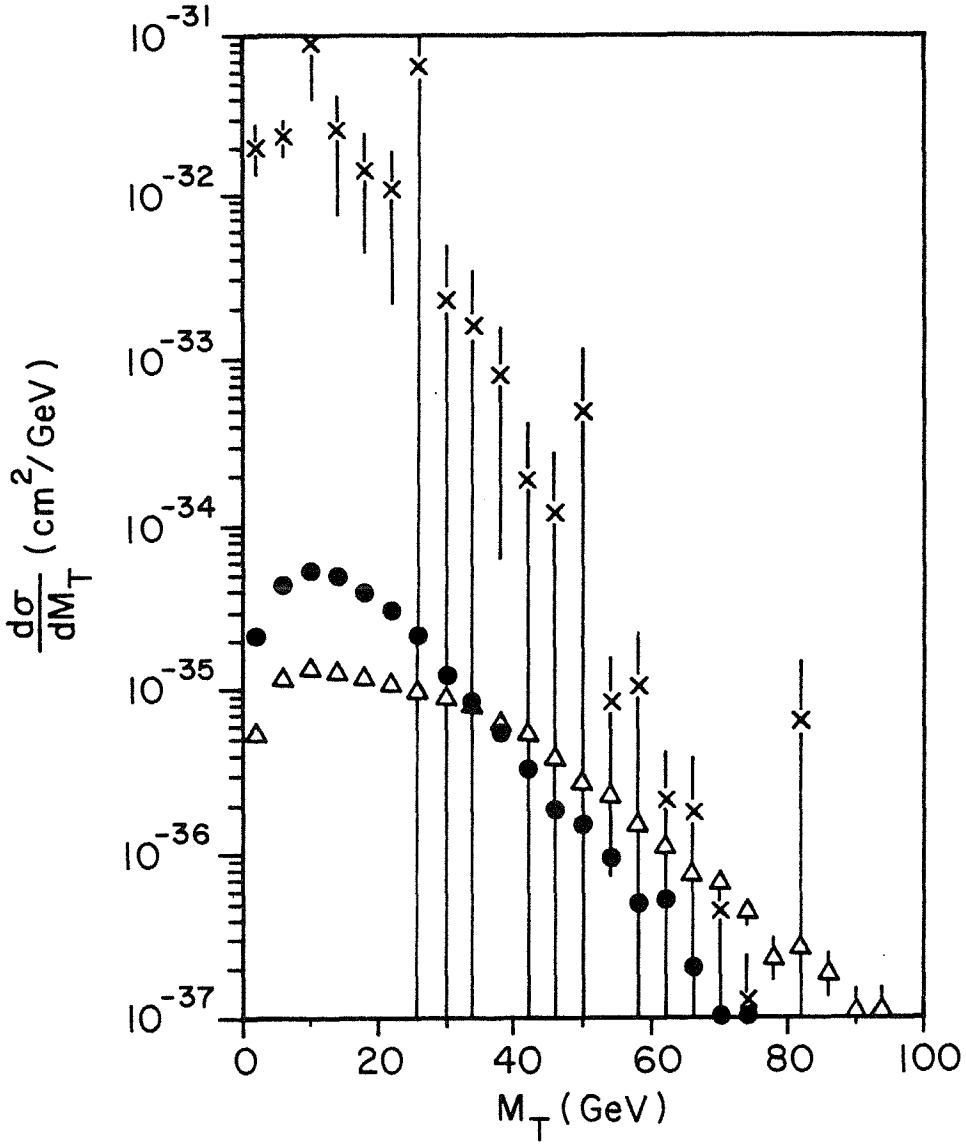
10^{-31}
10^{-32}
10^{-33}
10^{-34}
10^{-35}
10^{-36}
10^{-37}
$\frac{d\sigma}{dM_T}$ (cm^2/GeV)
0
20
40
60
80
100
M_T (GeV)

Fig. 2.7b

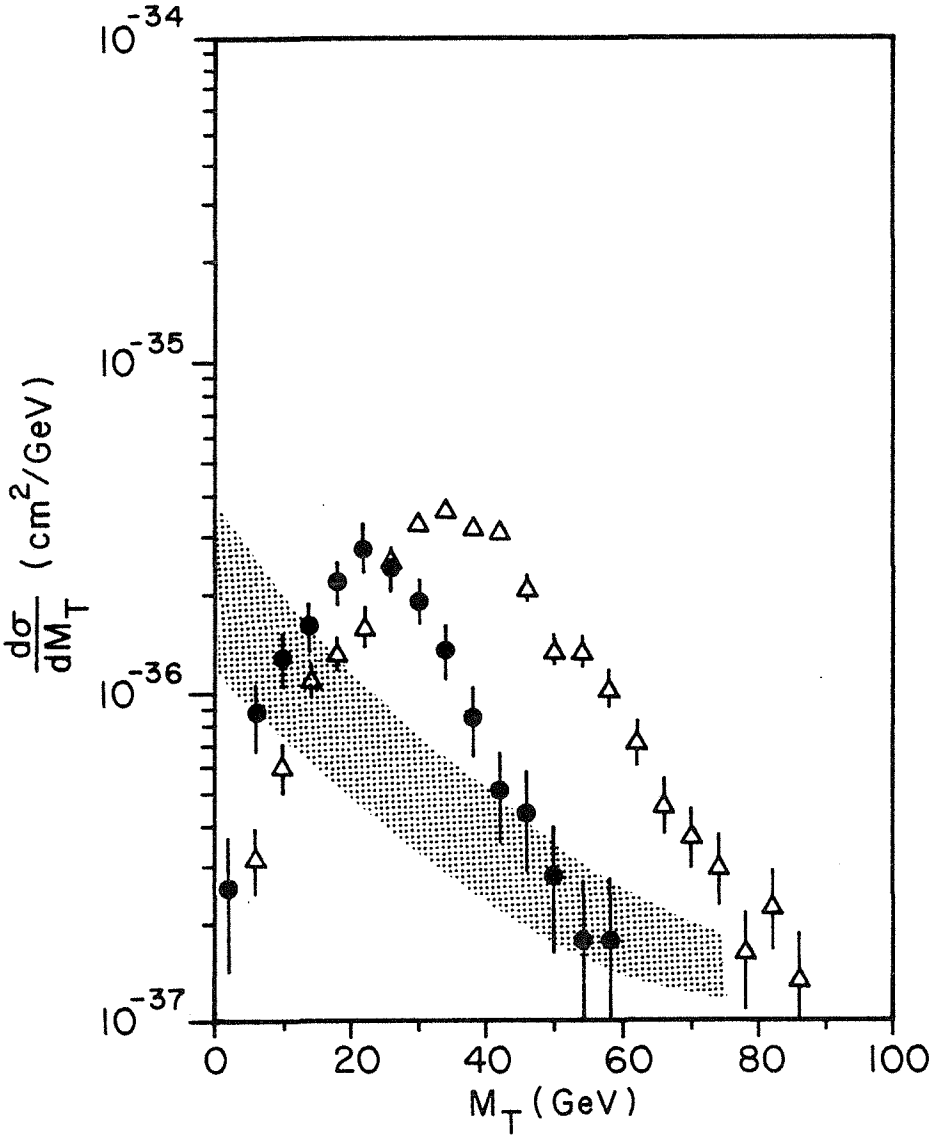
10^{-34}
10^{-35}
10^{-36}
10^{-37}
$\frac{d\sigma}{dM_T}$ (cm^2/GeV)
0
20
40
60
80
100
M_T (GeV)

Fig. 2.8

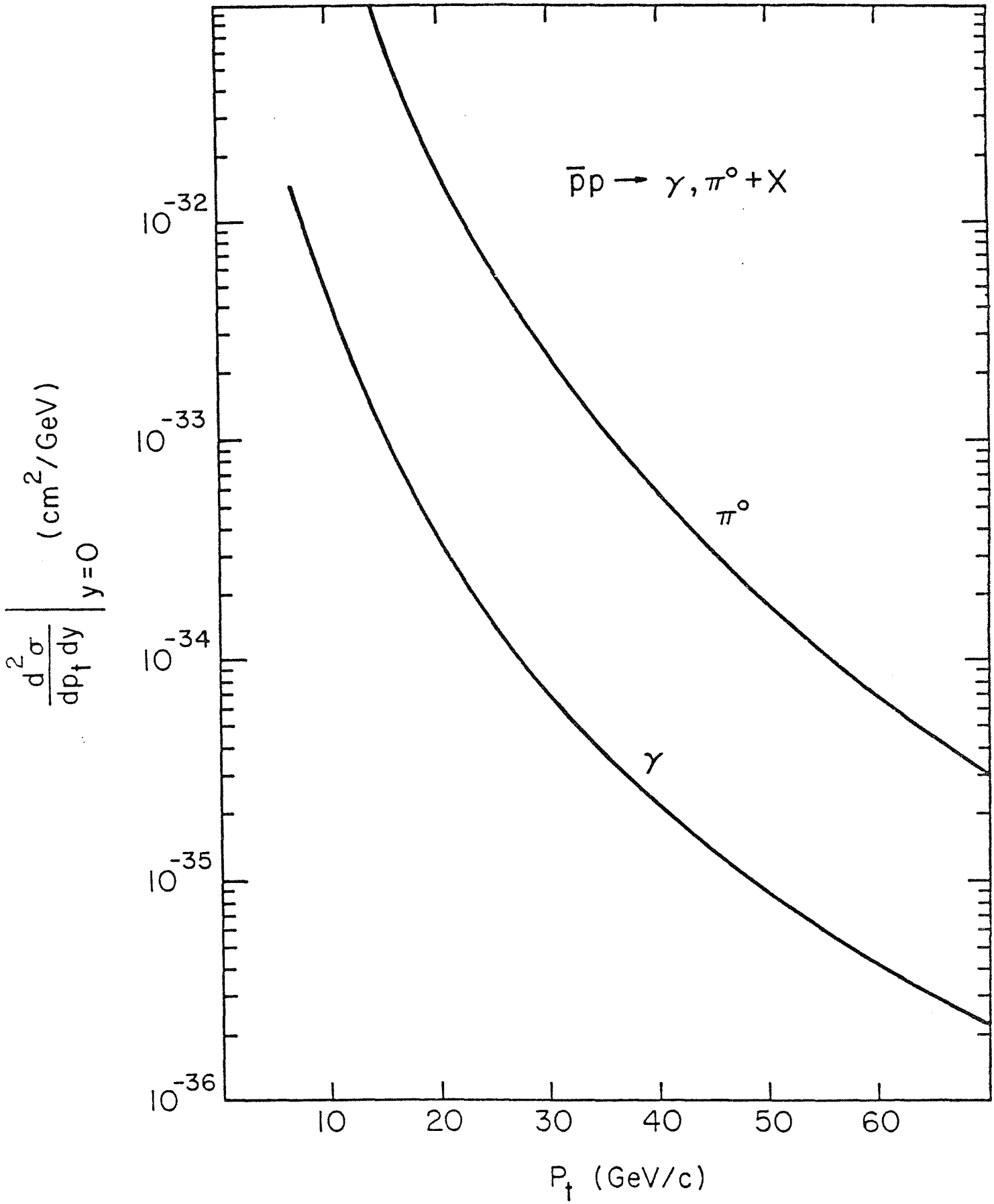
$\bar{p}p \rightarrow \gamma, \pi^0 + X$
π^0
γ
$\left.\frac{d^2\sigma}{dp_t\,dy}\right|_{y=0}$ (cm^2/GeV)
10^{-32}
10^{-33}
10^{-34}
10^{-35}
10^{-36}
10
20
30
40
50
60
P_t (GeV/c)

Fig. 2.9

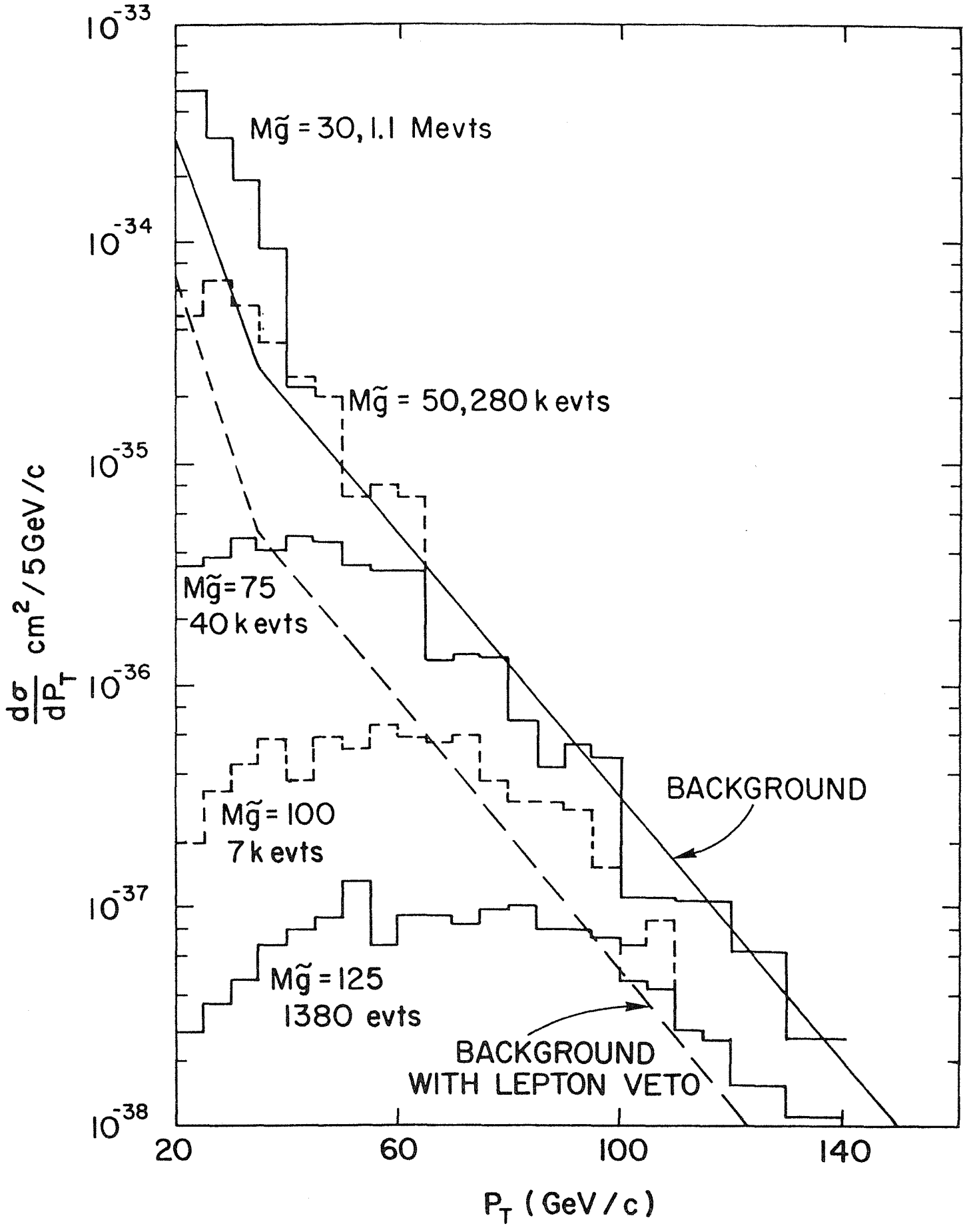
10^{-33}
10^{-34}
10^{-35}
10^{-36}
10^{-37}
10^{-38}
$\frac{d\sigma}{dP_T}$ cm^2/5GeV/c
$M\tilde{g}$ = 30, 1.1 Mevts
$M\tilde{g}$ = 50, 280 k evts
$M\tilde{g}$ = 75
40 k evts
$M\tilde{g}$ = 100
7 k evts
$M\tilde{g}$ = 125
1380 evts
BACKGROUND
BACKGROUND
WITH LEPTON VETO
20
60
100
140
P_T (GeV/c)

Fig. 2.10

3. MAIN FEATURES OF THE DETECTOR

3.1 DESIGN CONSIDERATIONS

The list of physics questions discussed in Chapter 2 has strongly influenced our design of the DØ experiment, as filtered through our collective taste and prejudice. We have also kept in mind the emerging experience with the CERN $Sp\bar{p}S$ detectors and their strengths, weaknesses, and potential upgrades. The CDF detector at BØ has been designed with specific characteristics aimed at a rather broad range of physics topics; inevitably that detector has stressed certain features at the expense of others. To some extent, the DØ detector has been designed to give complementary focus upon the same collection of general questions.

3.1.1 Central Magnetic Field

From the beginning, the DØ group, as did its predecessor proposals,[1] has believed that there should be no magnetic field in the central region, The absence of field allows a more compact detector which can cover the full solid angle more uniformly. Measurement of energies for high transverse momentum particles is not compromised, since calorimetric energy resolution surpasses magnetic momentum resolution at high energies. Although for electrons below 20 GeV there is some loss in the ability to distinguish electrons from hadrons due to the lack of momentum-energy comparison, this is compensated by the smaller surface of calorimetry and the ability to subdivide more finely, both longitudinally and transversely. Finally, analysis of multiparticle events in a non-magnetic detector is likely to be somewhat more straightforward than in a magnetic detector.

3.1.2 Lepton Identification

We have stressed the ability to identify and measure leptons well; both electrons and muons are important in meeting the physics objectives outlined in Chapter 2. For electrons, excellent energy resolution is desired, primarily to permit the accurate study of narrow massive states, as discussed in Section 2.1. Very good energy resolution, for electrons, is readily obtained. We would also like to be able to identify electrons well enough to be able to distinguish them in the vicinity of hadron tracks, or of jets. Searches now under way at CERN for t-quark signatures are apparently limited by the possibility of misidentifying a jet as an electron.[2] We expect to have unusually good electron identification; the quite fine segmentation of the calorimetry should give an e/π discrimination, by itself, comparable to that achieved at CERN--about 1 in 5000. In addition, the use of Transition Radiation Detectors (TRD), in the Central Tracking region, should give another factor of about 100.

The muons on the other hand are less well analyzed (but are sign selected); they can however be identified even when emitted at the core of a high p_T hadron jet due to the containment of hadronic showers. The ability to study muons even inside jets is important for heavy flavor studies, heavy lepton searches, and technicolor searches. It is a capability which is missing, or rather severely restricted, in other collider experiments. Having good identification for both leptons is important in supersymmetry searches, where it is the lack of leptons in the event that can be used to suppress backgrounds.

3.1.3 Missing Transverse Energy

Good missing transverse energy resolution is the key to inferring the existence of neutrinos in an event. Its utility in the discovery of the W has been amply demonstrated. Many of the searches for new phenomena described in Section 2.3 require such a capacity. The detector we propose should be superior in its ability to sense missing E_T. Missing E_T resolution depends primarily upon good hadron energy resolution; use of uranium-liquid argon calorimetry is thus the optimum choice. The effect of cracks in coverage, both at small angle beam-exit holes and in large angle calorimetry is to worsen the missing E_T resolution; attention must be paid in design to minimizing these holes and cracks. Figure 3.1 shows the effects of finite energy and angle resolution, beam hole size, and cracks in detector coverage upon the missing p_T distributions. Given the energy resolution characteristics of uranium calorimetry, we see that coverage down to about 1° with respect to the beams is required for a good match. The effect of 8 azimuthal dead areas in the large angle calorimetry has also been investigated. Allowing 2.5-cm wide dead spaces gives a contribution to missing p_T which is, on average, comparable to that from the energy resolution, although the effect on the tails of the distribution is larger. Thus, it is imperative to design the calorimetry in such a way as to minimize the dead area.

3.1.4 Calorimetry Segmentation

The desire for good segmentation of calorimetry is dictated by much of the physics program in Chapter 2. Figure 3.2 shows the spatial distribution of energy distribution for two events from UA2.[3,4] In Fig. 3.2a, the two jets of approximately 100 GeV/c each are clearly visible, but any detail within a jet is unresolved. In Fig. 3.2b, the $Z^0 \rightarrow e^+e^-\gamma$ event is displayed showing a

small angle separation between one electron and the photon. Clearly e-γ separation could not be much smaller and still be detectable, although study of these events versus opening angle would be highly useful for elucidation of the mechanism. Study of multijet production is also clearly dependent upon a fine-grained subdivision of the calorimetry, subject only to the constraint imposed by the transverse shower sizes themselves.

The control of backgrounds to electron and muon identification also requires relatively fine segmentation. The background consists of near spatial overlaps of charged hadrons and photons; smaller cell sizes will help, as will additional information from fine longitudinal segmentation and positive electron identification in the TRD external to the calorimetry. Similarly, muon identification will be aided if a muon candidate can be seen to be minimum ionizing in a series of calorimeter cells.

3.1.5 Hadron Energy Resolution

Hadron energy resolution plays an important role in many parts of our physics menu. Measurement of jet energies and masses are critically dependent upon it, as is the missing E_T resolution. Hadron calorimetry based upon sampling in iron plates (with appropriate fine early sampling for electromagnetic energy) can probably achieve a resolution of $\sigma/E = 0.7/\sqrt{E}$. This technique for energy measurement is ultimately limited by fluctuations in the energy associated with nuclear breakup and low-energy fragments[5] and also the fluctuation in response to the electromagnetic and hadronic components of the shower. In addition, there is some indication[6] that an iron sampling calorimeter is limited to about 10% resolution for high energy jets. We have felt that obtaining the best available energy resolution, namely that obtained using uranium sampling throughout the calorimetry, will have many extremely

important advantages. Chief among these are an improved ability to isolate two jet decays of W and hence better ability to identify jet flavors. The improvement on missing p_T resolution leads to more accurate measurement of m_W/m_Z and better searches for new phenomena.

3.1.6 Photon Detection

Several of the physics issues at TeV I depend upon the ability to recognize high p_T single photons. The requirements placed upon the detector by this goal are quite severe. For example, at p_T = 30 GeV/c, the minimum separation distance for the two photons from a $\theta = 90°$ $\pi°$ is 0.65 cm at 70 cm. Since this is considerably less than the shower size, it is not possible to distinguish $\pi°$ from single γ solely on this basis.

There are, however, additional properties of two photon showers which can be used to give a statistical means for identifying them. The longitudinal profile of energy distribution changes with energy; shower maximum increases like ℓnE. One published result[7] shows that with 12 depth samples, a pair of equal energy photons can be distinguished from a single photon of twice the energy 90% of the time, on the basis of the differences in longitudinal energy deposit.

Another way of distinguishing single photons from overlapping multiple photons from $\pi°$, η, or ω uses the depth of first conversion. This distribution has been used in a crude way to isolate single γ's at the ISR[8] with only two depth segments. Figure 3.3 shows the distribution of first conversion for single and multigamma showers. Studies have shown [9] that the fraction of single gammas can be found in a sample of 1, 2, 3, and 6 γ events with a precision of a few percent, for a sample of 10,000 events. Given the

importance of sensing single photons, our aim is to use as many means as possible (good lateral and longitudinal sampling) to signal their presence.

3.2 SUMMARY OF THE DETECTOR

The evolution of a detector design beginning from the recommendations of the PAC in June 1983 has taken a somewhat circuitous path. The first attempt was based upon an amalgamation of the various proposals considered by the PAC. It incorporated EM calorimetry using segmented scintillation glass blocks, iron plates with gas PWC sampling for hadronic energy measurement, and magnetization of the iron plates to give the muon momentum measurement. A somewhat parallel study was based upon a unified uranium-liquid argon calorimeter system (ULA) for both EM and hadronic sections.

The collection of disadvantages with either system are summarized in Table 3.1. Both designs were investigated in some detail. The physics capability of the glass/iron sampling design stresses the best EM energy resolution (but with worries on its achievability due to calibration problems and inaccessibility of phototubes). The ULA design stresses hadron energy resolution and missing p_T resolution (with worries connected to mechanical engineering difficulties). After extensive study and discussion, we have chosen the ULA option for our proposal. This choice allows us to focus on a relatively more limited set of problems for design and construction. Its major defect, electromagnetic energy resolution, is alleviated by the fact that calibration problems are much simpler than in the scintillating glass version. For electron energies above 50 GeV/c we expect that the ULA calorimeter will give equal or better resolution than the glass. Since much of our physics program (Z° width , heavy particle searches) involves very high energy electrons, this seems a reasonable compromise to take.

Figure 3.4 shows a schematic plan view of one half of the detector. There is symmetry both around the beam axis and the $\theta = 90°$ line. In this view, one can see the eight major systems comprising the detector: central tracking (CT); central (CC), end (EC), and plug (PC) calorimeters; central (CF), intermediate (IF), and end (EF) iron toroidal magnets; and the set of muon chambers surrounding nearly all the detector. Each of these systems is discussed in detail in subsequent chapters.

The angular coverage of the central tracking system extends down to approximately 5°, constrained by the size of the Saver beam pipe. Calorimetry in the three separate regions extends to a minimum angle of 1°; the division between end and plug calorimetry is shown at 5° although more detailed studies may alter this choice somewhat. The muon coverage extends down to 8° with respect to the beams.

It should be understood that several details of the detector layout are not finalized; effort is proceeding to refine, improve, and simplify the detector in several ways. For example, it may prove beneficial to amalgamate the iron toroids CF and EF. The choice of the angle dividing EC and PC calorimetry is under study, as is the longitudinal placement of PC. Final placement of the various subsystems is being evaluated with attention paid to the needs for electronics space on the detector, cable pathways, and access to the detector for maintenance.

3.2.1 Central Tracking

The central tracking system consists of three separate subsystems in angular coverage. A central cylindrical drift chamber occupies the volume bounded by radius $r \leq 70$ cm and longitudinal coordinate $z \leq 72$ cm. Two end sections of planes perpendicular to the beams extend to $z = \pm 137$ cm. The

central chamber contains two regions of cylindrical gaps separated by a 30 cm gap for Transition Radiation Detectors. The inner region has 12 separate gaps with an inner radius of 10 cm (chosen to reserve space for the later inclusion of a micro-vertex chamber). The outer region has 6 separate gaps with an outer radius of 68 cm. Each gap contains 24 or 48 separate drift cells in azimuth with alternate gaps staggered by one half cell. The sense wire in each cell is parallel to the beam. It is sistered with a delay line, parallel to the sense wire; each delay line is read out from both ends. Multihit electronics is required for sense wires and delay lines in order to retain sensitivity to the large number of produced particles. The function of the delay lines in each cell is to give z-position resolution within a few millimeters. They also provide a space point approximation for each track crossing.

The end track sections have a similar separation into tracking, TRD, and tracking regions. Sense wires run in alternating vertical and horizontal directions again with delay lines giving the coordinate along the wire. The sense wire pulses are timed for coordinate determination and measured for pulse area. The dE/dx information is required in order to give good rejection against close e^+e^- pairs from internal or external conversion.

The TRD compartments within the tracking system are repetitive layers of amorphous radiating surfaces (polyethylene fibers) followed by Xenon- Argon filled proportional chambers for detection of the transition radiation x-rays. Tests of a similar system of four such repetitive layers[10] give electron/pion separation factors of about 100.

We require some triggering information from the tracking; a determination of the z-coordinate of the interaction vertex is needed for establishing muon momentum and for calculation of p_T. This will be supplied from a special circuit using the delay-line signals on two of the gaps of the central chamber.

3.2.2 Calorimetry

Each of the five modules of uranium liquid-argon calorimeters consists of a fine sampling front-end section spanning 24 radiation lengths for electromagnetic shower energy, a medium sampling section out to 4-5 absorption lengths for the bulk of the hadron shower energy, and a coarse sampling section for the last part of a hadron shower. It is our intent to standardize the uranium plate-gap-readout structure in all of the calorimetry in order to simplify some of the construction procedures. Current plans call for a 3 to 5 mm argon gap for ion collection. The subdivision of the readout electrodes into pads or strips is special to each part of the detector, according to the physics needs and geometry.

The basic readout geometry will be two-dimensional pads, ganged together in depth to form a set of tower compartments. There are four compartments in the EM sections of depth 2, 2, 6, and 14 x_0 each. The sampling frequency is chosen to be about two per radiation length (1.5 mm U plates). In the third EM compartment, we propose to interleave pads with sets of strips (1 cm width) whose function is to give accurate profiles of shower tranverse energy deposits. The hadronic section is divided into three or four compartments. The first several employ 4 mm U plates in order to retain the compensation mechanism. The last (hadron leakage) compartment uses thick (20 mm) U plates since the energy compensation mechanism is not required in the last two absorption lengths. All hadronic compartment readout planes are divided into pads, ganged together within the compartment.

The total number of EM towers in the central ULA detector is about 3000; the number of hadronic towers is about 800. With the eightfold depth segmentation and strip readouts, we have about 25,000 channels for readout in the Central ULA detector. The end detectors each have about 10,000 channels in 1000 towers. The smaller plug calorimeters each have about 5000 channels and

360 towers. The arrangement of pads in towers is a very good approximation to projective geometry in end and plug calorimeters. The central calorimeter is projective in the ϕ-coordinate; in the θ-coordinate, the finite length of the interaction region makes such a projective solution less exact.

Trigger information from the calorimeters will be obtained from fast signals which represent the sum of about 10 adjacent calorimeter towers. These fast trigger signals will exist separately for EM and hadronic sections.

3.2.3 Muon Detector

The muon identification and momentum measurement is accomplished with five separate iron toroids, excited to a mean field of 20 kG. The iron thickness is about 1 m (6 absorption lengths) at $\theta = 90°$; at smaller angles the thickness increases in such a way as to keep equal punchthrough at fixed p_T for all angles. The toroids are arranged with gaps between them to allow access corridors for cables emerging from the inside of the detector.

Measurement of muon tracks is accomplished with planes of proportional drift tubes (PDT's) located between calorimeters and toroids, just outside the toroids and further outside near the walls of the collision hall. Some additional help in muon tracking is given by knowledge of the vertex location and the central tracking system. This information has limited usefulness due to the large amounts of scattering material in the calorimeters.

Measurement of muon momenta depends upon which tracking systems are useful for a particular muon candidate. Isolated muons seen in all three systems will be measured to about $\pm$ 20% out to about 200 GeV/c, where measurement errors begin to be dominant. Muons within jets may be difficult to find in the central tracking detector; they should be observable in the

PDT's between calorimeters and toroids (7 to 9 absorption lengths into the showers) and would lead to slightly poorer momentum resolution.

Triggering for muons will employ a line segment taken from the struck cells of the PDT outside the iron toroids, together with a fast determination of the interaction vertex position. The quantization imposed by PDT cell sizes implies that a trigger threshold at p_T = 5 GeV/c can be set.

With a total thickness of absorber in excess of 13 absorption lengths, we anticipate little background to muons from hadron punchthrough. In order to leave some flexibility for future help in muon identification or momentum resolution, we plan to leave three 2.5 cm gaps in the iron toroids.

3.2.4 Hall Size Requirements

The dimensions of the volume required to encompass the detector of Fig. 3.4 are ± 6 m in both transverse dimensions and ± 9.8 m along the beam line. These dimensions include the lever arm required for establishing the muon exit track angle and a minimum amount of space for personnel access and detector movements for access to the inner detectors.

The entirety of the assembled detector, with the exception of the most upstream and downstream muon PDT's, fit within the space between the low-β quadrupoles at ±6.75 m from the intersection point.

REFERENCES CHAPTER 3

1. Fermilab proposals P714, P724, P726, P727, and P728.

2. P. Darriulat, private communication.

3. P. Bagnaia et al., CERN preprint CERN-EP/83-94.

4. P. Bagnaia et al., CERN preprint CERN-EP/83-112.

5. W. J. Willis and V. Radeka, Nucl. Instrum. Methods **120**, 221 (1974); J. H. Cobb et al. Nucl. Instrum. and Methods **158**, 93 (1979).

6. S. Iwata in Proceedings of the 1979 TRISTAN Workshop, DPNU 3-79.

7. R. L. Engelmann et al., Nucl. Instrum. and Methods **216**, 45 (1983).

8. A. L. S. Angelis et al., Phys. Lett. **94B**, 106 (1980).

9. Fermilab proposal P714, addenda 6, 12, and 29.

10. A. Bungerer et al., Electron Identification Beyond 1 GeV by Means of Transition Radiation, Siegen Univ. Preprint (1983); C. Fabjan et al., CERN-EP/83-45.

TABLE 3.1

Disadvantages of Alternate Designs

Scintillating Glass/Iron Sampling Calorimetry	Uranium Liquid-Argon Calorimetry
1. Many phototubes (~10^4), most in inaccessible locations	1. Uranium metal procurement and difficulties in maintaining plate thickness and flatness tolerance
2. Calibration difficulties - many independent elements whose calibration must be transferred from beam tests using optical reference systems	2. Mechanical support is difficult
3. Relatively long radiation length of glass (4.35 cm) yields tight packing requirement	3. Need for cryogenic enclosures, fill lines, etc.
4 Assembly difficulties with finely segmented iron toroids, keeping gap tolerances for interleaved chambers	4. Tight specifications on electronic noise of preamplifiers
5. Mixed media, noncompensating, calorimetry yields hadronic energy resolution ~ ($80\%/\sqrt{E}$).	5. Energy resolution for low-energy electrons and photons is limited to ($10\%/\sqrt{E}$)

FIGURE CAPTIONS - CHAPTER 3

3.1 Cross section vs. missing p_T for various contributions. The solid line is for losses in a 1° beam hole only; -o- is for 1° beam hole and energy resolution in calorimetry. The dashed line includes the effect of beam hole, energy resolution, and angular smearing effects (all hadron impact points are smeared with σ_x, σ_y = 2 cm). The effect of 8 azimuthal cracks of width 2.5 cm over the central calorimeter (not shown) is to broaden the missing p_T-distribution for $p_T^M > 10$ GeV/c without appreciable effect below 10 GeV/c. The contributions from signals due to ν (heavy quark) production and 100 GeV gluinos are also shown.

3.2 (a)Energy deposition pattern for a two-jet event from UA2 (Ref. 3). (b)Energy deposition pattern for a candidate $Z \to e^+e^-\gamma$ event from UA2 (Ref. 4).

3.3 Distribution of first conversion point for single photons and multiphoton events from π^0, η, and ω.

3.4 Plan view of the detectors showing the major systems. CT is the central tracking; CC, EC, and PC are central, end, and plug uranium liquid-argon calorimeters; CF, IF, and EF are magnetized iron toroids in the central, intermediate, and end regions. The dashed lines represent the locations of muon PDT tracking chambers.

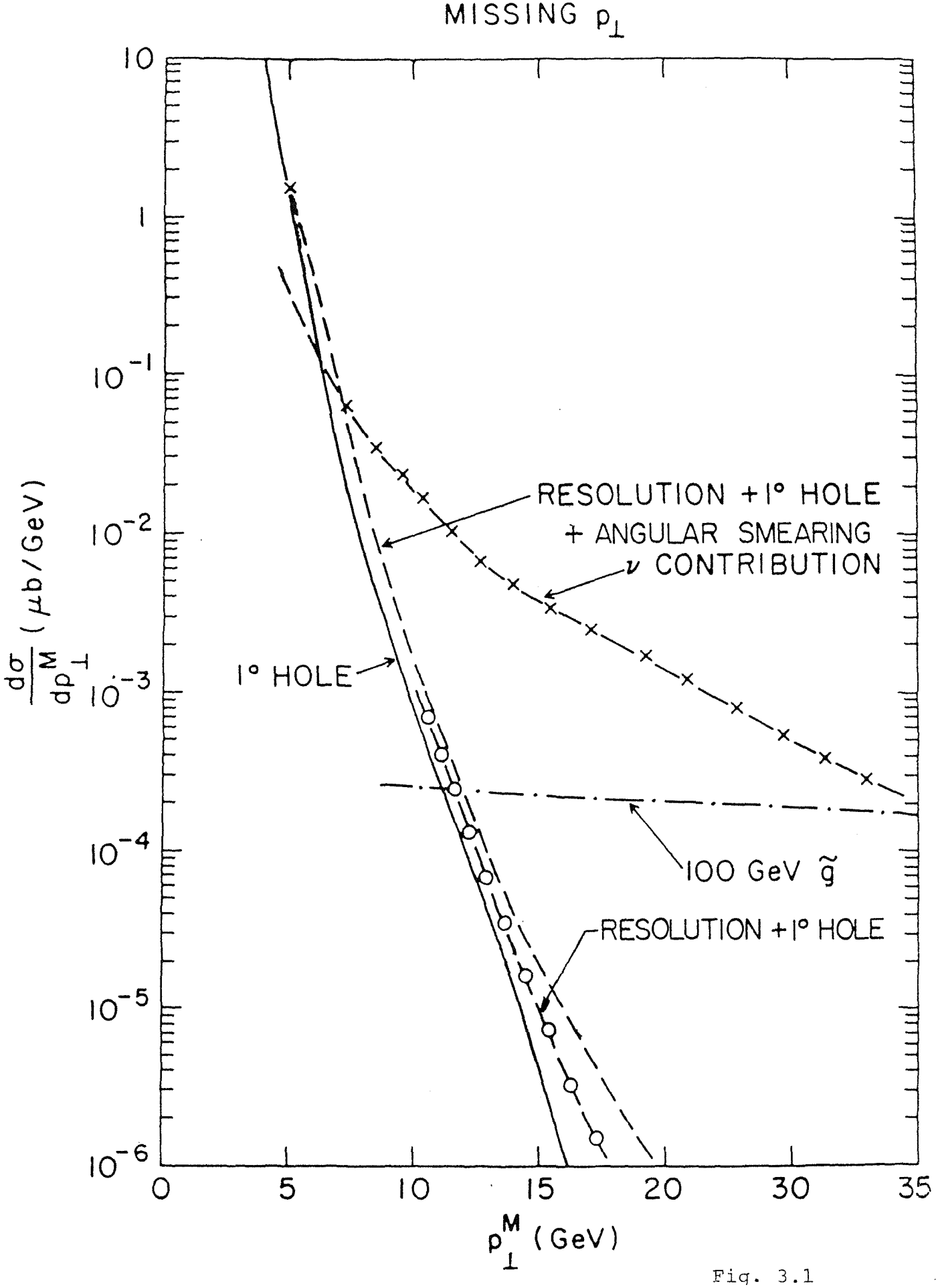
MISSING $p_\perp$
10
1
10^{-1}
10^{-2}
10^{-3}
10^{-4}
10^{-5}
10^{-6}
$\frac{d\sigma}{dp_\perp^M}$ (μb/GeV)
RESOLUTION +1° HOLE
+ ANGULAR SMEARING
ν CONTRIBUTION
1° HOLE
100 GeV $\tilde{g}$
RESOLUTION +1° HOLE
0
5
10
15
20
30
35
$p_\perp^M$ (GeV)

Fig. 3.1

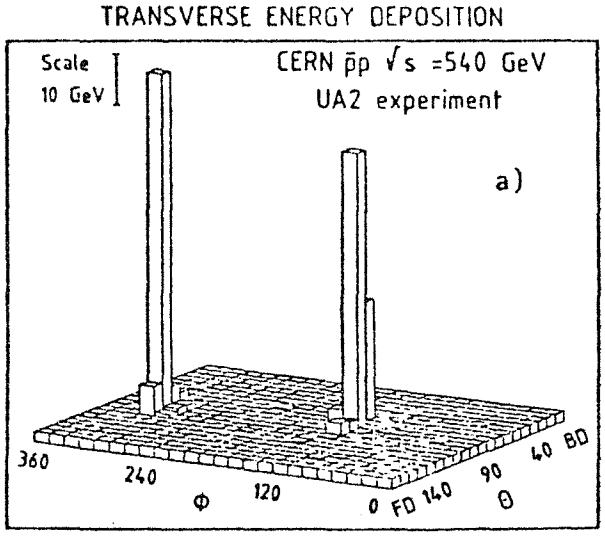
TRANSVERSE ENERGY DEPOSITION
Scale
10 GeV
CERN p̄p √s =540 GeV
UA2 experiment
a)
360
240
120
0 FD 140
90
40 BD
Φ
θ
Run NO. 1465
Trigger NO. 43978
Total transverse energy 213 GeV

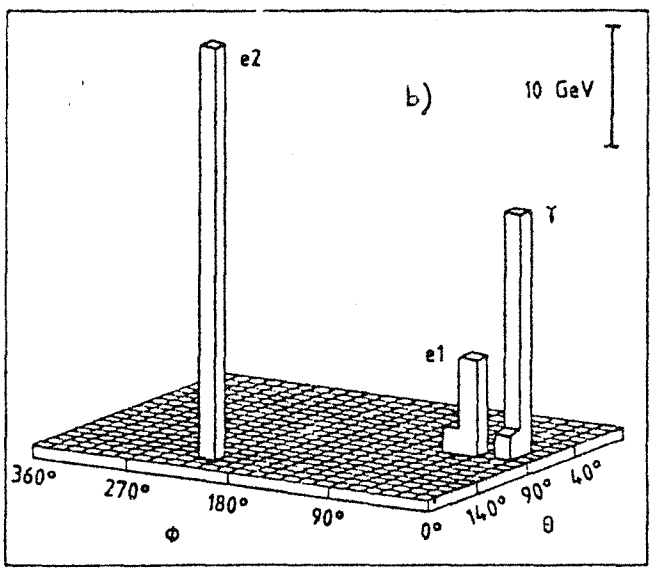
e2
b)
10 GeV
γ
e1
360°
270°
180°
90°
0°
140°
90°
40°
Φ
θ

Fig. 3.2

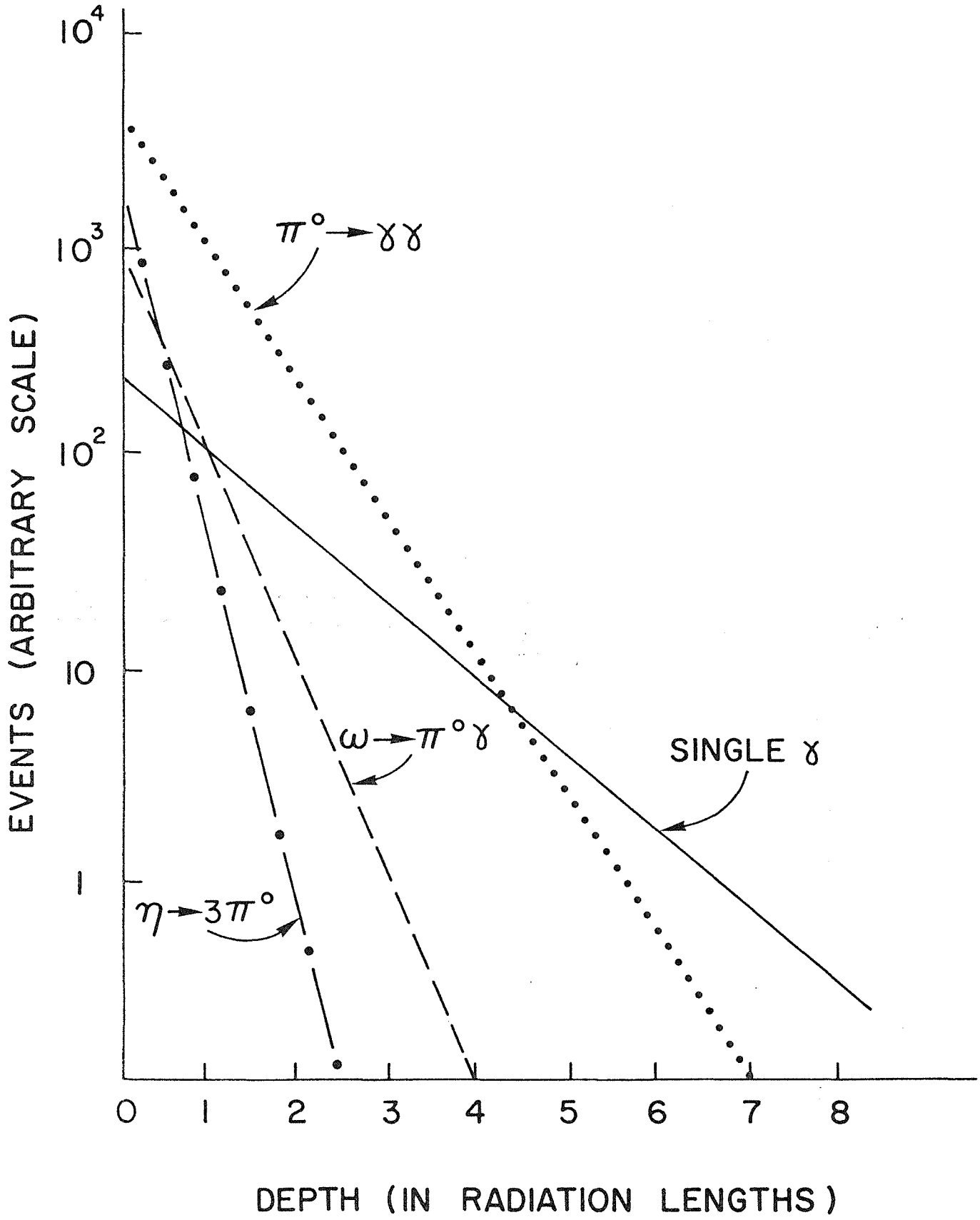
10^4
10^3
10^2
10
1
EVENTS (ARBITRARY SCALE)
$\pi^\circ \rightarrow \gamma\gamma$
$\omega \rightarrow \pi^\circ\gamma$
SINGLE γ
$\eta \rightarrow 3\pi^\circ$
0 1 2 3 4 5 6 7 8
DEPTH (IN RADIATION LENGTHS)

Fig. 3.3

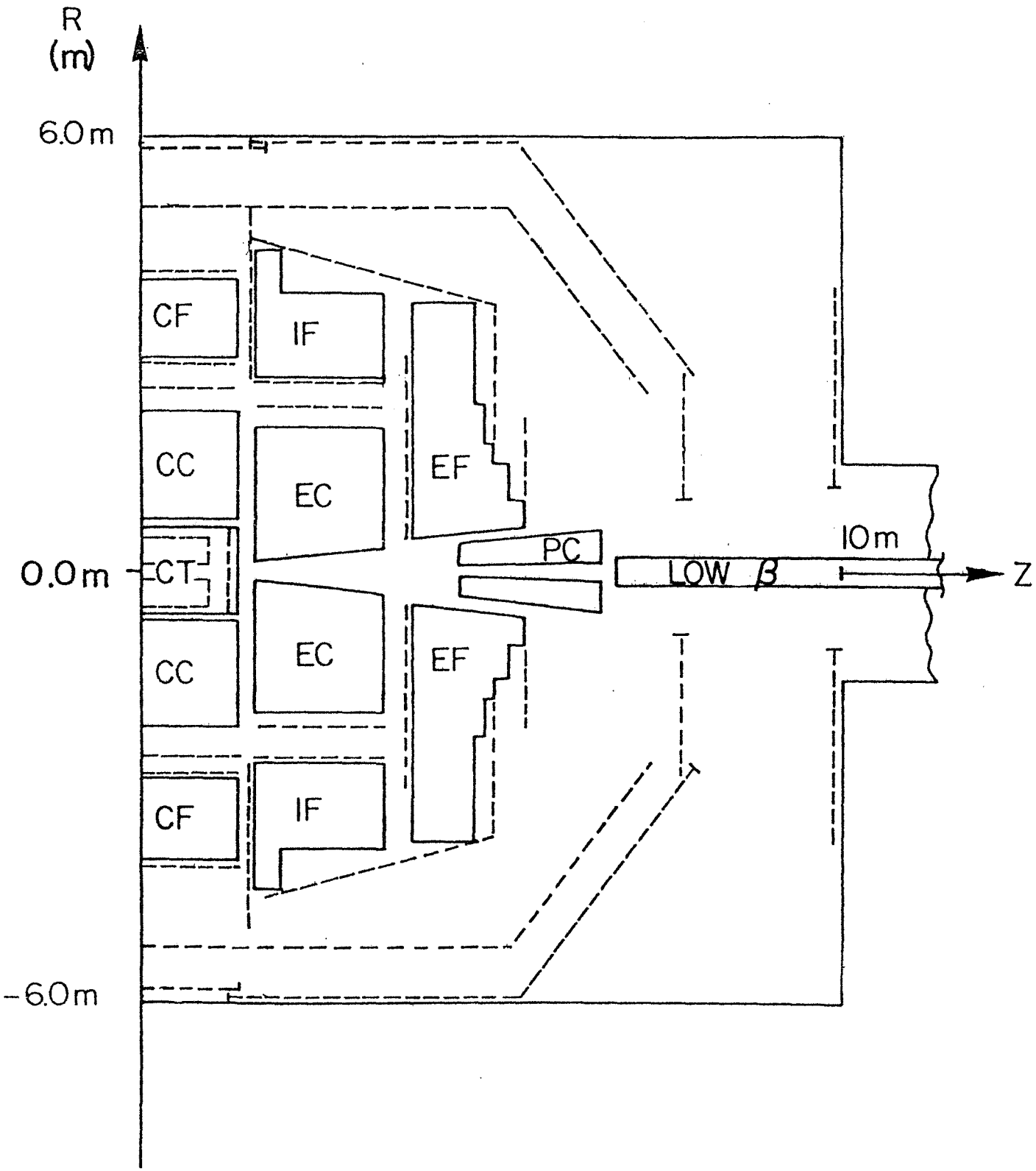

E 740 LAYOUT

Fig. 3.4

4. CENTRAL DETECTOR SYSTEM

4.1. INTRODUCTION

The features of the central detector system, including particle tracking and particle identification are determined by the emphasis of this experiment on electrons, muons, and photons.

a. Electron identification. The central drift chambers must reconstruct tracks with sufficient angular precision to allow unambiguous correlation of charged tracks with electromagnetic showers in the calorimeter. The required precision is $\Delta\theta \simeq \Delta\phi \simeq \pm 1.5$ mrad, comparable to shower centroid determination. This precision is also sufficient to keep fake electron triggers (due to overlap of a photon and a charged hadron) at an acceptably low level.[1]

In addition to charged particle tracking, the central detectors will include transition radiation detectors (TRD) capable of π/e discrimination at the level of up to 1/100.[2] The drift chambers will also have sufficient gas sampling to distinguish (by dE/dx) one minimum ionizing track from two (spatially unresolved) tracks. This will help discriminate electrons from converted photons.

b. Photon detection. In addition to the ability to distinguish γ's from e's mentioned above, it is desirable that the central detectors be low in mass and have a minimum of dead regions. We plan for all elements of the central system to comprise $\leq$ 10% of a radiation length.

c. Muon identification and triggering. The central drift chambers will be equipped with circuitry for determining the location of the event vertex quickly ($\leq$2 μsec) and with reasonable resolution ($\pm$10 mm along the beams). Vertex information of this quality is important in

forming a muon trigger with a clean threshold in p_T (i.e., not swamped by resolution broadening effects).

The drift chambers must have sufficient multi-track efficiency for identifying leptons near jets although total reconstruction of all tracks in narrow jets is not at a premium. However, it is foreseen that high precision reconstruction of tracks may be desirable at a later stage for the study of lifetimes of heavy states. With this in mind we reserve the radial space between the beam pipe and r = 10 cm for future implementation of a mini-vertex detector.

In Section 4.2 we discuss the mechanical and electronic details of the drift chambers. The fast vertex-finding electronics is described in Section 4.3 and the TRD system is presented in Section 4.4.

4.2 DRIFT CHAMBERS

Figure 4.1 shows the space available for the central detector system and the outlines of the components of the system. We divide the central space into three regions: a central region (centered on z = 0) and two end regions. We treat the drift chambers in these regions separately below.

4.2.1 Central Drift Chambers

The central drift chambers are grouped into two concentric cylindrical shells, spaced as far apart in radius as possible for good angular resolution. The space between the shells is occupied by the TRD system. The cross section of the cylinder is a 12-sided polygon; this will be cheaper to construct than cylinders and also simplifies the field shaping, since all drift cells are planar. The inner module performs the major part of the tracking and comprises 12 gaps. The outer module (which would be sensitive to

tracks back-scattered from the calorimeter) serves to improve the resolution of tracks projected from the inner module and has 6 gaps. The unusually high number of gaps assures adequate redundancy, even for high-multiplicity events.

A schematic of the cross-section of the modules in the $r\phi$-plane is shown in Fig. 4.2. Each gap in the inner (outer) module is divided into 24 (48) azimuthal sectors (or drift cells) each subtending 15° (7.5°). The support medium is composed of layers of closed-cell polyurethane foam (specific gravity $\simeq$ 0.2) between successive gaps. Calculations show that 6mm foam layers provide adequate support for the wires; the function of the end plates is to provide accurate wire positioning and closure of the drift volume.

Each drift cell has a sense wire and a delay line at the center and field wires at the ends (adjacent cells within a gap have field wires in common). Each cell also has field-shaping strips lining the inner face of the kapton. The drift space is 15 (44) mm at the inner (outer) radius.

Cells in alternate planes are rotated in ϕ by half a cell width. Left/right ambiguities are thus resolved, and edge effects are reduced. Such a configuration is also essentially self-calibrating in drift velocity, and measures close pairs of tracks better; one member of the pair is detected in a cell with one orientation--the second member in a cell with the other orientation.

The sense wires stretch the entire length (z) of the detector, and are foreseen as having one readout equipped with multi-hit electronics. (The utility of charge division for aid in pattern recognition needs to be investigated.) In addition to the drift time, the pulse amplitude will also be recorded, integrated in a ~50 ns gate using CCD or flash ADC electronics. This information can be used to identify tracks very close in θ and ϕ and externally converted electron-positron pairs. Based on previous results,[3] it should be possible to achieve $\pm^{2-3}$ mm precision on delay lines up to 150 cm in

length. This is sufficient to achieve the desired angular precision, using both inner and outer modules. If tests currently underway show that lines of this length have too much attenuation, or if one wishes to obtain better resolution using the inner module only (for example, for $K \to \mu\nu$ kink detection), we will segment the delay lines. The pulses from both ends of each segment will be brought out on fine twisted pairs embedded in the foam and separately digitized. The number of separate electronics channels for the central detectors (see Table 4.1) is based on the assumption that no delay line segment is longer than 50 cm.

Such techniques have been used successfully in two ISR experiments. The CCOR Collaboration[4] used a system with 8 cylindrical gaps in a 1.4 T magnetic field. The delay lines had lengths up to 150 cm and a specific delay of 2.3 ns/cm. The position resolution achieved was ±5 mm. Experiments R209[5] and R210 used planar chambers equipped with shorter delay lines giving 7.5 ns/cm. They achieved a position resolution of ±1.6 mm. We can, therefore, expect to obtain resolutions close to ±1 mm using short delay lines with specific delays of 10 ns/cm. (The delay lines will need some development to find the best compromise between specific delay, attenuation, impedance, thickness of material, etc.)

Assuming a resolution of ±1.5 mm in a single gap, the resolution in θ would be about ±2 mr for the inner module as a whole, and could be improved to ±1 mr by reconstructing the event vertex with several tracks. Using, say, 9 tracks, the vertex could be located to about ±0.25 mm, not taking systematic effects into account.

4.2.2 End Drift Chambers

For small angle tracks ($\theta \leq 30^0$), tracking is done in a pair of drift chamber modules whose wire planes are perpendicular to the beam direction. These chambers are built along the same principles as the central chambers: sense wire and delay line readout, polyurethane foam supports, etc. The wires run in the x and y directions: x, x', y, y',..., where the prime indicates a shift of a half-drift cell relative to the preceding plane. The electronic functions of the readout are also the same as in the central drift chamber: digitization of drift time and pulse height (in 50 ns slices) on the sense wires and time digitization on both ends of the delay lines. Because the sense wires give good spatial coordinates in two directions (x and y) in the end chambers, the delay lines can be thought of as serving primarily a pattern-recognition function. Therefore, they probably do not require the same degree of segmentation; we have assumed 75 cm in Table 4.1.

4.3 FAST VERTEX FINDER

The vertex finder uses two gaps of the central drift chamber only: one in the inner module and one with the same orientation in the outer module. If studies should show that this twofold coincidence is inadequate, a threefold coincidence could be envisaged. The amount of electronics and cost of the vertex finder increases linearly with the number of gaps used. (See however the tests reported on the method in Section 10.2.1.)

The vertex finder is subdivided into azimuthal sectors corresponding to single cells in the chambers. Within a sector one and only one track is considered: that which occurred closest to the sense wire.

Let us consider the logic for a single sector. The sense wire signals ($r\phi$ coordinate) determine whether the inner- and outer-gap space points

project back to the crossing point in the rϕ-plane. The beam-crossing signal gates the sense-wire pulses and starts two integrators (Fig. 4.3). The integrators are stopped by the flip-flops set by the sense-wire pulses, creating levels proportional to the drift time. The inner and outer gap levels are then combined linearly to give a level monotonic in the distance of closest approach of the projected track to the beam-crossing point. A comparator generates a gate (the Gϕ gate) only if this distance is less than a fiducial amount ε.

The delay-line logic is sketched in Fig. 4.4. The associated sense-wire flip-flops start integrators which are stopped by the pulses from both ends of the delay-line segment. The delay-line times are both added (length of segment) and subtracted (z coordinate of track). Since the integrators are started by the sense wires, only the corresponding tracks should give the correct sum among the various segments associated with each sense wire. Window discriminatiors exclude the incorrect sums, and the appropriate segment number is recorded in a priority encoder.

The time-difference levels enter a linear multiplexer instructed by the priority encoder to pass only the appropriate segment. This level is added to a level set via a DAC by the priority encoder giving the z-offset corresponding to the selected segment.

It is conceivable that the earliest sense-wire signal and the earliest delay-line signals do not all three correspond to the same track. In such a case the delay-line summed-time criterion would not be met, and the sector would be treated as if it were empty--not contributing an estimate of the vertex z coordinate.

The vertex coordinates obtained from several sectors could be histogrammed, and a best estimate determined with peak-finding circuitry. Given a sufficiently efficient peak finder, this method would be sensitive to double

vertices. We estimate that a z resolution of less than ± 10 mm could be achieved. A study of the algorithm described here is presented in Section 10.2.1.

For on-line testing we foresee a system whereby artificial pulses in the appropriate timing configuration are injected into the system, and possibly a separate digitization of the pulses used for vertex finding, which could then be compared directly with the normal data acquisition.

4.4 TRD SYSTEM

The e/π ratio for $p_T > 10$ GeV/c is expected to be $\sim 10^{-4}$. The pion rejection power of the electromagnetic calorimeter will probably be $\sim 10^3$ at 5 GeV/c (and perhaps somewhat better at higher p_T). Cuts on event topology (such as electron isolation cuts) make this rejection factor adequate for $W \to \ell\nu$ because in this case e/π is more like 10^{-2}. But for other processes we need to improve the rejection factor by at least a few ×10. For example, study of heavy quark jet production and of supersymmetric particles require identification of leptons down to relatively low p_T ($\lesssim 5$ GeV/c). Since most ν's are accompanied by e's or μ's, in order to reduce their contribution to missing p_T it is necessary to detect the presence of such e's and μ's even if they are not well isolated. The calorimeter by itself cannot distinguish an electron from a photon/hadron overlap within ~1 cm.

The above issues can be addressed with a TRD before the calorimeter. Using a design similar to that of Büngener et al.[2] with polyethylene fiber radiators one can expect rejection factors ($p_e > 2$ GeV/c) of 50-100 with 4 radiator-detector modules. The detectors are multiwire proportional chambers filled with a 50-50 Xe-Ar mixture. Figure 4.5 shows the 4 module lay-out designed to fit in the space between central drift chamber modules. A planar

array of similar construction fits between the end-drift chamber modules as well. Table 4.1 contains more details. Track-to-track separation of 5 mm is achievable and overlaps within 5 mm do not appreciably affect the π/e rejection factor because the readout electronics will be sensitive only to charge deposits above a threshold. This suppression of the response to minimum ionizing particles will be accomplished either with discriminators on each output or with more sophisticated cluster counting electronics.[2]

REFERENCES CHAPTER 4

1. F. E. Paige et al., "Monte Carlo Simulation of High p_T Jets," Proceedings 1983 DPF Workshop on Collider Detectors: Present Capabilities and Future Possibilities, p. 30. See also addendum 12 to Fermilab Proposal 714 (LAPDOG) (11/14/82).

2. A. Bungener et al., "Electron Identification Beyond 1 GeV by Means of Transition Radiation," Siegen University Preprint (unpublished); C. Fabjan et al., CERN-EP/83-43.

3. A. Breskin et al., Nucl. Instrum. Methods **119**, 1 (1973).

4. L. Camilleri et al., Nucl. Instrum. Methods **156**, 275 (1978).

5. A. Bechini et al, Nucl. Instrum. Methods **156**, 181 (1978).

TABLE 4.1 CENTRAL DETECTOR PARAMETERS

I. DRIFT CHAMBERS	DIMENSIONS	THICKNESS	GAPS	SENSE WIRES	DELAY LINE SEGMENTS	READOUT CHANNELS
A. Inner Cylindrical	r_{inner} = 10 cm r_{outer} = 27.4 cm ℓ = 144 cm	0.046 X_0	12	24/gap = 288	3/sensewire = 864	288 sense, 1728 delay
B. Outer Cylindrical	r_{inner} = 59 cm r_{outer} = 68 cm ℓ = 144 cm	0.023 X_0	6	48/gap = 288	3/sensewire = 864	288 sense, 1728 delay
C. Inner End	z_{inner} = ±77 cm z_{outer} = ±94.4 cm r_{inner} = 7.5 cm r_{outer} = 68 cm	0.046 X_0	12	24/gap = 288	2/sensewire = 576	288 sense, 1152 delay/end
D. Outer End	z_{inner} = ±128 cm z_{outer} = ±137 cm r_{inner} = 11.6 cm r_{outer} = 68 cm	0.023 X_0	6	12/gap = 144	2/sensewire = 288	144 sense, 576 delay/end
II. TRD						
A. Cylindrical	r_{inner} = 29 cm r_{outer} = 57 cm ℓ = 144 cm	0.040 X_0	4	200/gap = 800	-	800
B. End	z_{inner} = 97 cm z_{outer} = 125 cm r_{inner} = 9.7 cm r_{outer} = 68 cm	0.040 X_0	4	100/gap = 400	-	400/end

FIGURE CAPTIONS - CHAPTER 4

4.1 Arrangement of the tracking and transition radiation detectors.

4.2 Cross-section view of the central tracking chambers.

4.3 Vertex finder schematic diagram (sense-wire logic).

4.4 Schematic diagram for delay-line logic yielding the z coordinate of an interaction.

4.5 Cross-section view of the central TRD detectors.

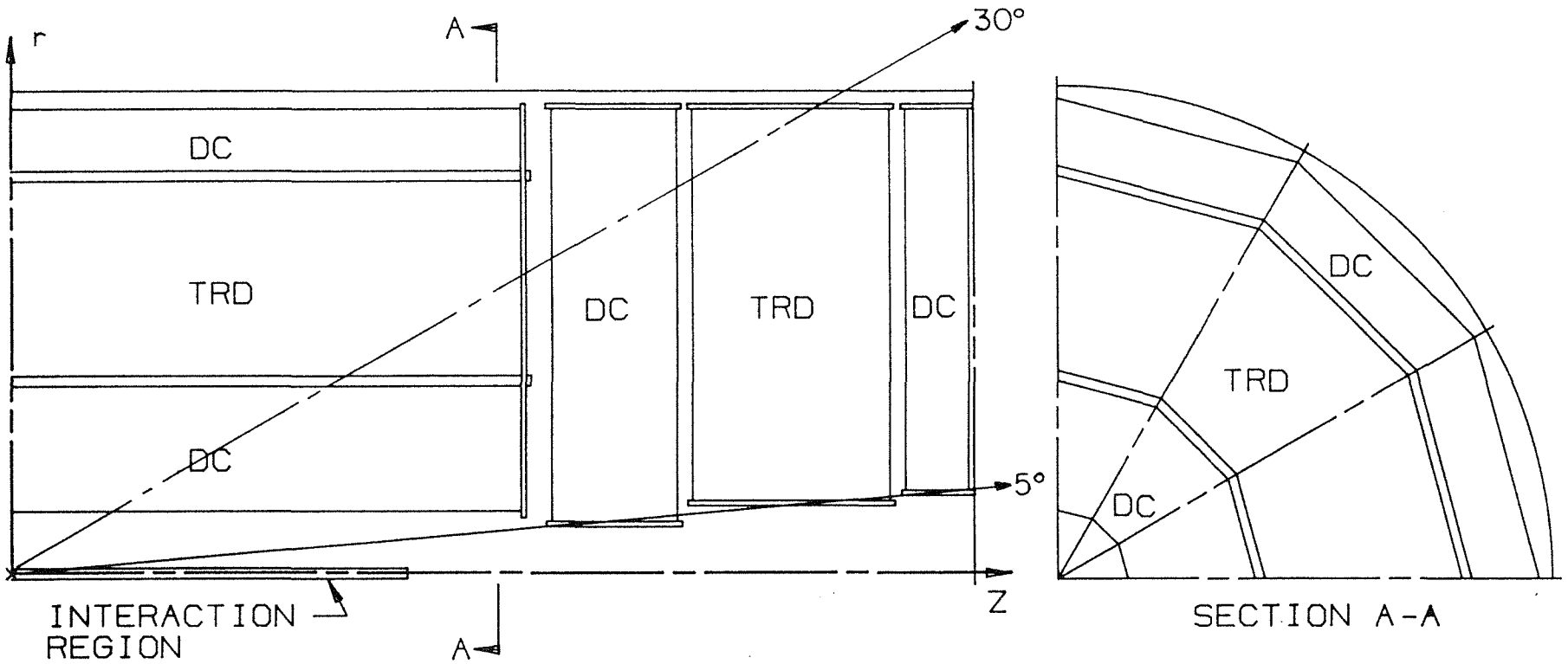
r
A
30°
DC
TRD
DC
DC
TRD
DC
5°
Z
INTERACTION
REGION
A
DC
TRD
DC
SECTION A-A

Fig. 4.1

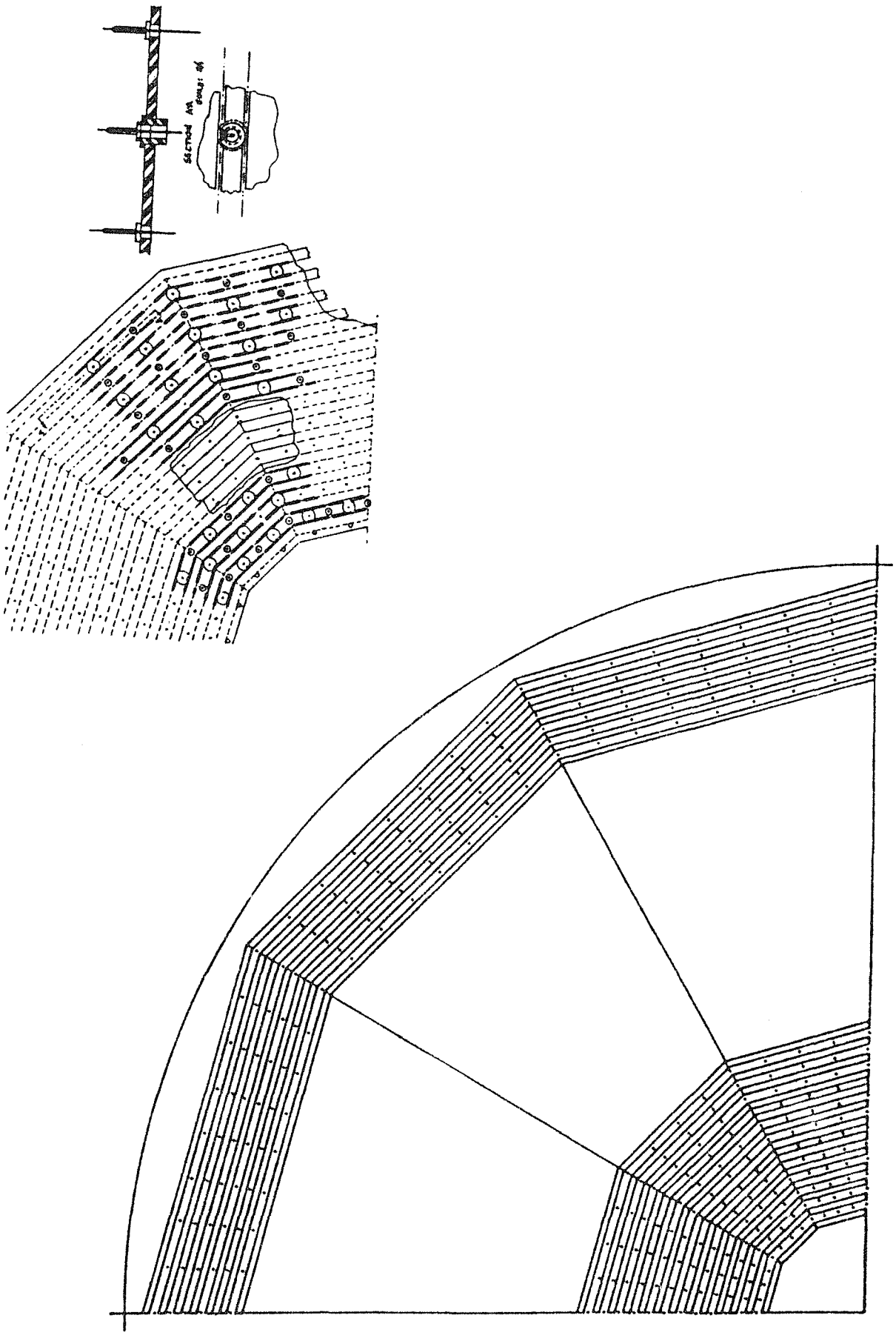

Fig.4.2

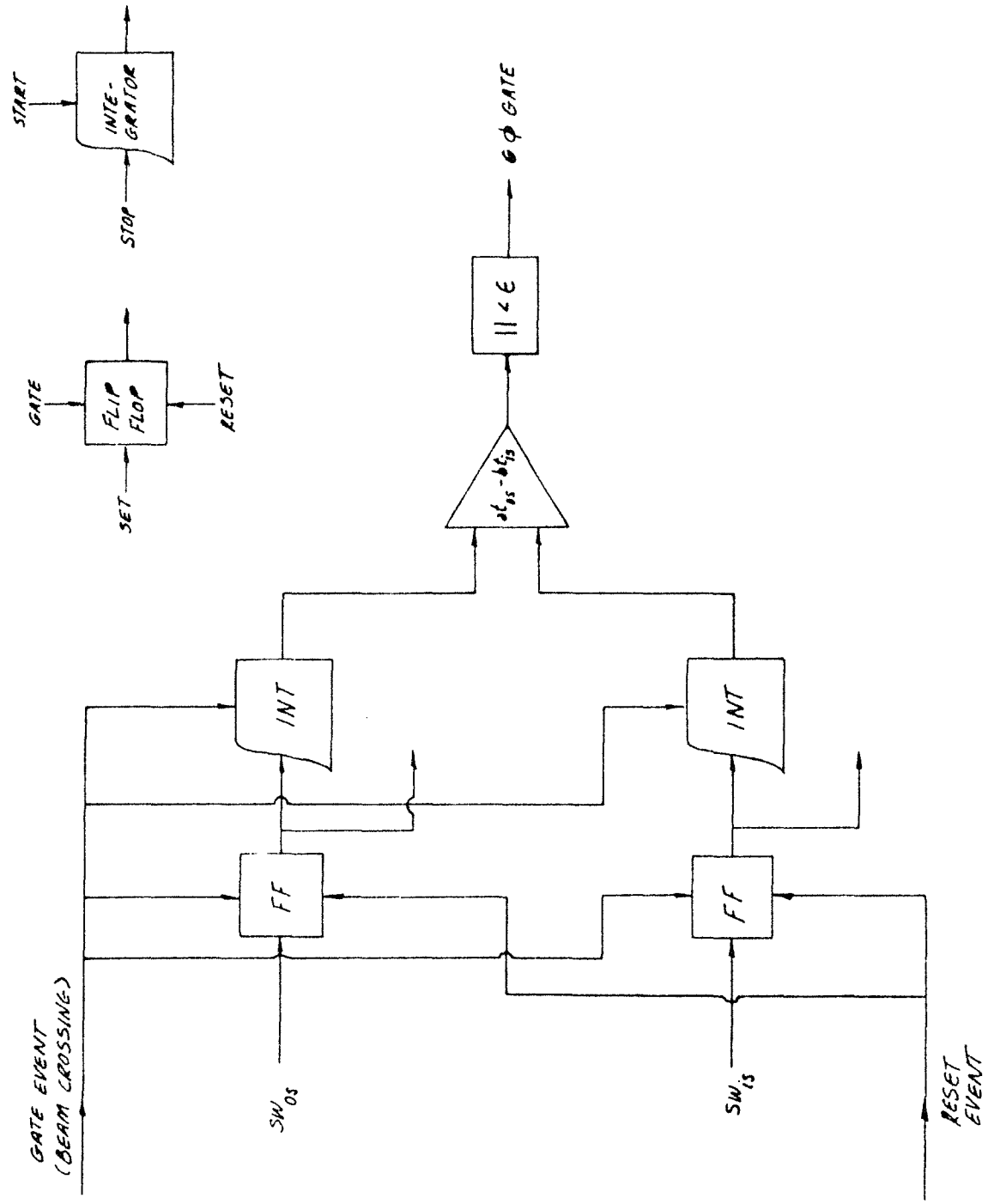
START
INTE-
GRATOR
STOP
GATE
FLIP
FLOP
RESET
SET
ϕ GATE
$|| < \epsilon$
$\Delta t_{05} - \Delta t_{13}$
INT
INT
FF
FF
GATE EVENT
(BEAM CROSSING)
SW_{05}
SW_{13}
RESET
EVENT

Fig. 4.3

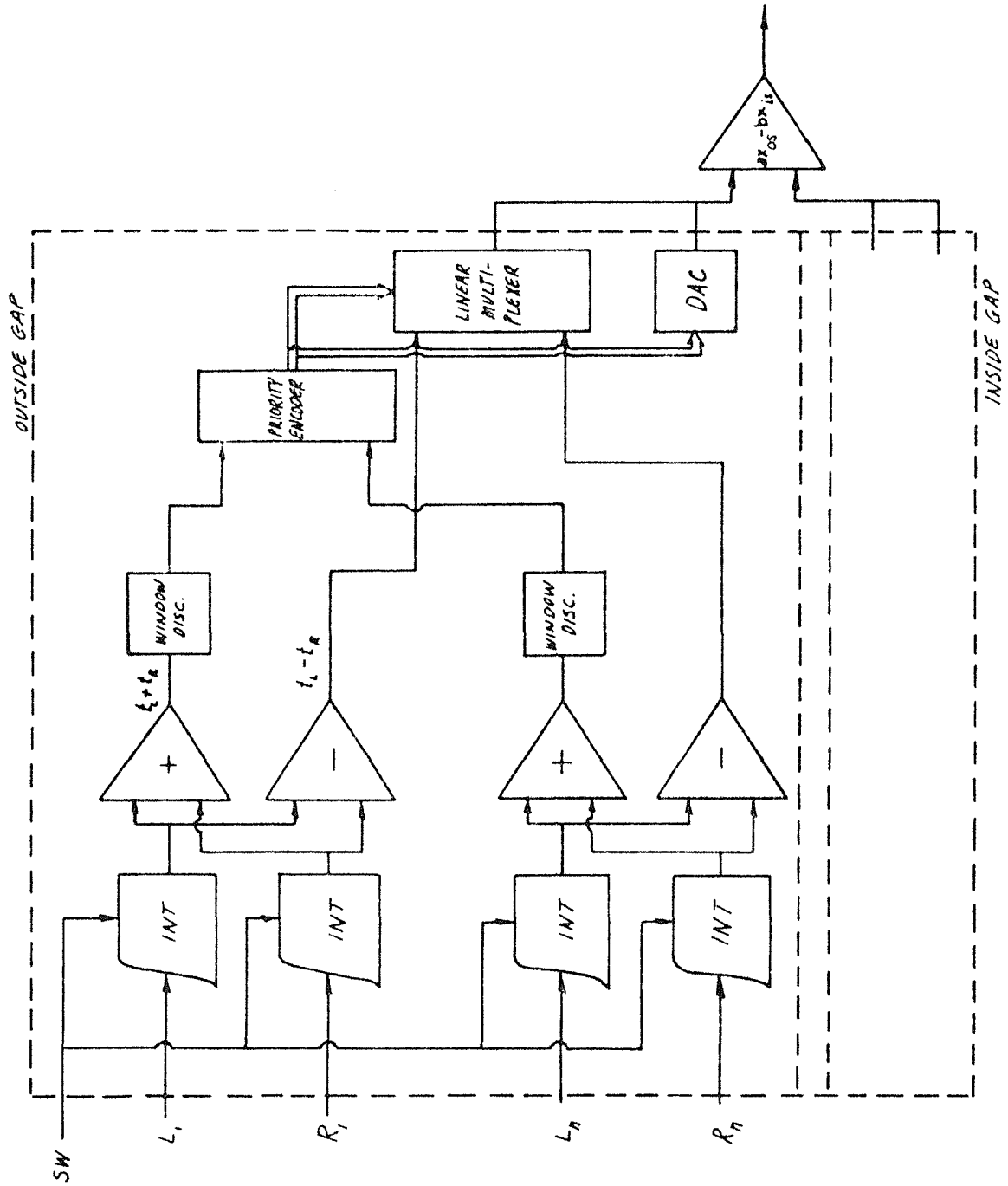
OUTSIDE GAP
INSIDE GAP
LINEAR MULTI-PLEXER
DAC
PRIORITY ENCODER
WINDOW DISC.
WINDOW DISC.
$t_L + t_R$
$t_L - t_R$
+
−
+
−
INT
INT
INT
INT
SW
L_1
R_1
L_n
R_n

Fig. 4.4

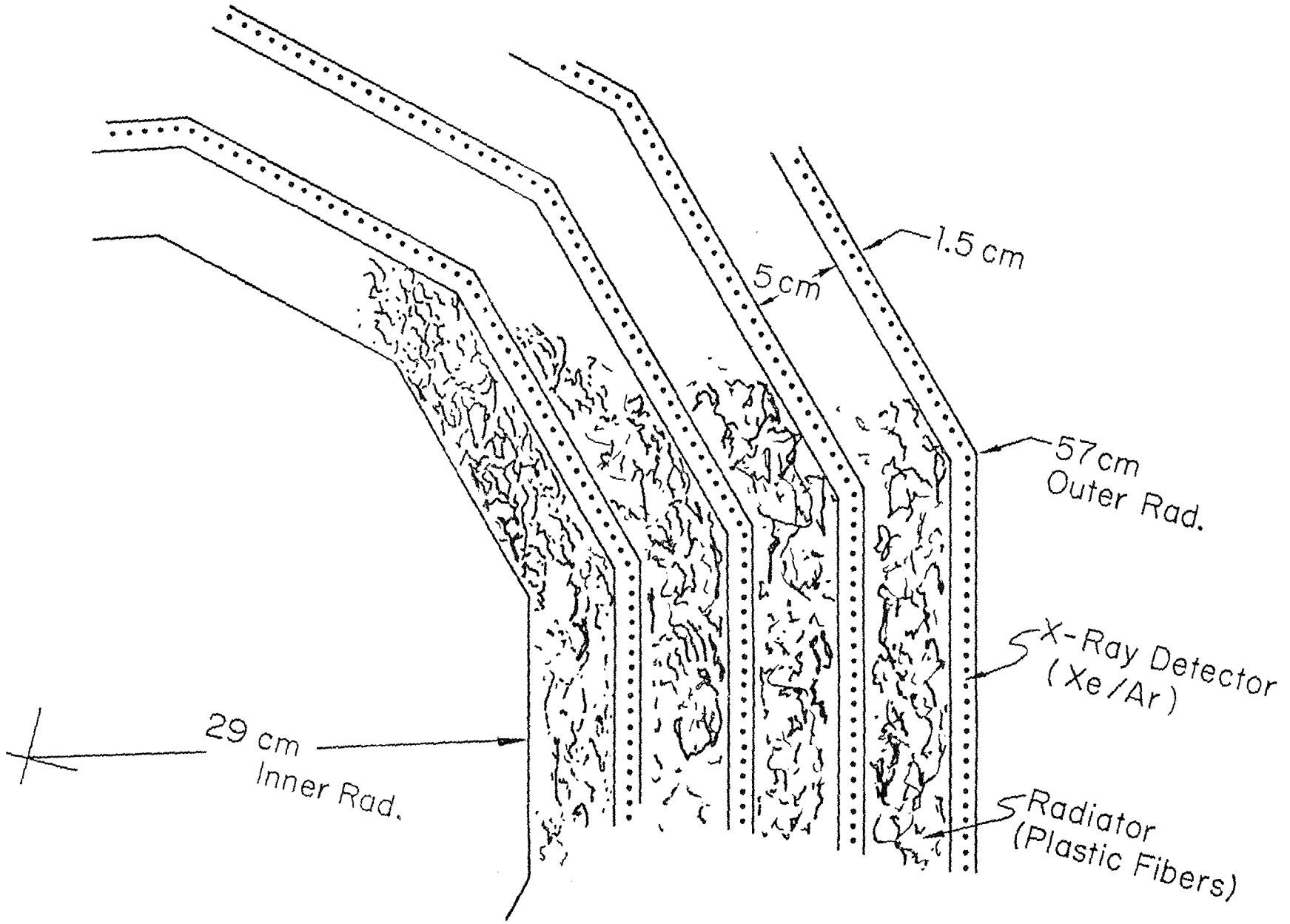
1.5 cm
5 cm
57 cm
Outer Rad.
X-Ray Detector
(Xe/Ar)
Radiator
(Plastic Fibers)
29 cm
Inner Rad.

5. THE CENTRAL CALORIMETER

5.1 INTRODUCTION

In designing a calorimeter for this experiment, we have been guided by a number of considerations that reflect the physics we intend to address.

For the electromagnetic section of the calorimeter we require:

1. Good energy resolution;
2. Fine transverse segmentation to help identify electrons emitted close to other particles;
3. Fine longitudinal segmentation to ensure adequate $\pi^{\pm}/e$ separation and to improve γ/π° separation.

In addition, to achieve the ideal energy resolution in a large system ($\sim 10^4$ channels) the basic technique has to be such that the systematics of calibration and monitoring can be kept under tight control.

For the hadronic region we require:

1. Good energy resolution for jet studies and, particularly, for estimating missing p_T, E_T, etc.
2. Minimal dead spaces in order to benefit from this energy resolution;
3. Adequate transverse segmentation so that the p_T resolution is limited by the resolution in energy rather than in angle.

Finally, there are spatial constraints. We have reserved an inner space of radius 70 cm in which to perform good central tracking. Outside the calorimeter, the more space that is available, the better the measurement of muons. This argues for a compact and, therefore, dense calorimetric medium.

We investigated a number of options and arrived at a conclusion, based on the above guideline, which we felt to be unique and inescapable; a monolithic Uranium/liquid-Argon (ULA) detector incorporating both electromagnetic and

hadronic calorimetry over the full solid angle would be superior in performance to all feasible alternatives.

We have made an attempt to specify the design of such a calorimeter, which we present in this and the following two chapters. The parameters of the design have been given considerable attention, but we regard them as flexible and subject to review, at least until such time as we have completed a thorough study both on paper and in a test beam.

5.2 CELL STRUCTURE AND LONGITUDINAL SEGMENTATION

The central calorimeter is roughly cylindrical, subdivided in azimuth (ϕ) into 16 identical trapezoidal sectors (Fig. 5.1). Each sector contains 3 equal modules of length 84 cm in the longitudinal coordinate (z). Care has been taken to minimize the dead spaces due to the side walls ($r\phi$-plane) of the modules: they are thin (0.5 cm aluminum) and do not project to the source (angle between wall and radius vector is 5°). As a result, particles traverse at most one radiation length (X_0)--the hadronic loss is negligible.

The segmentation in depth is shown in Fig. 5.2 and listed in Table 5.1. Each module has an electromagnetic compartment followed by a hadronic compartment, both with 4 depth layers. Each layer comprises several cells. A cell consists of a (variable) thickness of Uranium, a 1.5 mm liquid-argon gap, a 1.0 mm G10 printed-circuit (P/C) board, and another 1.5 mm liquid-argon gap. The P/C boards have the same pad (or strip) structure on both sides, homologous pads being connected to the same internal signal lines. An insulating layer separates the pads from the outer surface--a resistive coating held at positive high voltage. This method of readout has the advantages of keeping the pads away from ground to reduce noise, and eliminating blocking capacitors

in the liquid volume. Within a layer, cells in the same tower are combined by internally ganging signal lines.

The four layers of the electromagnetic compartment, A through D, have 1/2 X_0 (1.5 mm) Uranium plates throughout. The total thickness is 24 X_0, apportioned 2 X_0, 2 X_0, 6 X_0, and 14 X_0 among the layers. The fine longitudinal segmentation in the early part of the shower gives excellent e/π discrimination. The first two 2 X_0 layers are split in equal halves ganged externally rather than internally. This is done to give us the option of further subdivisions to improve γ/π° discrimination, if experience indicates the need. The energy resolution obtained is expected to be $\sigma/E \simeq 11\%/\sqrt{E}$. The systematic term to be added to this is small ($\lesssim 1\%$); liquid-argon calorimetry is the only proved technique in which instrumental effects can be held at such a level.

The hadronic compartment has a total thickness of 6.2 absorption lengths (λ_0), plus 0.7 λ_0 in the electromagnetic compartment. The subdivision into layers is 1.0 λ_0, 1.4 λ_0. 1.8 λ_0, and 2.0 λ_0, with fine sampling in the first 3 layers (0.04 λ_0/4 mm plates) and coarser sampling in the last (leakage) layer (0.2 λ_0/20 mm plates). Using a comparable detector, ISR Experiment R807 found an energy resolution of $\sigma/E \simeq 37\%/\sqrt{E}$.[2] We expect to match or improve on this, since our calorimeter has greater thickness (6.9 λ_0 compared with 3.8 λ_0). The system is very compact; the overall depth of a module is 134.4 cm.

Several alternate designs for the cell structure in the calorimetry are being investigated. It may be possible to substitute some non-compensating absorber (Cu or Fe instead of U) in the rear of the calorimeter. The earlier sections of calorimetry may also have an admixture of Cu or Fe without severe degradation of energy resolution or equality of response to EM particles and hadrons, as in the R807 detector.[3] We are also considering the possibility of subdividing alternate absorber planes into tiles, thereby eliminating the need for making the pad structure on the P/C boards.

5.3 TRANSVERSE SEGMENTATION

We have chosen the transverse segmentation to yield a tower geometry which is projective in ϕ and has towers of constant width in z (Fig. 5.2). This leads to a solution which is not physically projective in θ; for any given interaction point, software construction of projective towers can be made. The segmentation is achieved at the level of the readout by segmenting the P/C boards into pads (or strips). The dimensions of the pads in both the electromagnetic and the hadronic compartments were chosen to minimize the number of channels while not compromising the angular resolution. Details of the segmentation are listed in Table 5.2.

In the relatively short electromagnetic compartment, the pad sizes hardly change with depth. A size of 6×6 cm^2 gives a position resolution of a few millimeters for isolated showers.[4] The resulting number of towers is $(14\times3)_z \times (5\times16)_\phi = 3{,}360$, with a total channel count of 13,440 for the 4 layers. To improve the separation of electrons from other tracks the segmentations around the shower maximum (layer C) is more complicated: of the 12 cells in this layer, 4 have ganged pads, 4 have ganged z strips with a width of 1 cm, and 4 have ganged ϕ strips with a width of 1.1 cm which are further segmented into 3 equal lengths in z (Fig. 5.3). The strips add 8,352 channels.

In the hadronic compartment the pad sizes chosen approximate the transverse size of hadronic showers, with pads varying in size from 14.0×15.2 cm^2 to 14.0×20.4 cm^2. The result is segmentation into 6 towers/module in z and 2 (4) towers/modules in ϕ in layers E, F, (G, H). The front layers, therefore, have $(6\times3)_z \times (2\times16)_\phi = 576$ towers, and the rear layers have $(6\times3)_z \times (4\times16)_\phi = 1152$ for a total of 3456 hadronic channels.

5.4 CONSTRUCTION

5.4.1 Mechanical Support

Each of the 48 modules would have trapezoidal end plates bridged by many shelves to make a rigid box structure.

The Uranium plates and G10 P/C boards are separated by ceramic spacers, and held together by rods passing through the plates and boards. Each module is enclosed in a thin aluminum skin welded onto the skeleton to contain its own independent liquid-argon volume.

Three modules are attached to form a sector weighing about 20 tons. Another possibility is to construct an arch as in the CDF calorimeter.

5.4.2 Cryogenics

We have not as yet developed a prototype design for the central cryostat. The Mark II calorimeter[5] at SLAC is of similar mechanical design to ours, and we intend to benefit as much as possible from their experience.

The inner vacuum wall is easy to construct from a thin aluminum cylinder. For the other vacuum walls we would follow Mark II. Whether to partition the vacuum into 16 vessels or to have a single vessel has still to be decided. We will almost certainly adopt the same methods as Mark II for the feedthrough of signal and high-voltage cables, using the same hermetically sealed 55-pin connector.[6]

We calculate a cool-down time of ≈10 days, assuming that 80% of the outer surface is covered with a liquid-nitrogen heat exchanger, assuming free convection only.[7]

5.5 SIGNAL CONSIDERATIONS

The signals from pads are ganged into low-impedance wire pairs, which lead to connectors on the outer cryostat wall along the end plates of the modules. The maximum signal length in the cryostat is ≈150 cm.

The pad capacitances are listed in Table 5.3. The noise, as discussed in Chapter 6, is a function of the square-root of the capacitance, whereas the signal varies as the product of the dE/dx and the path length of charged particles in the liquid argon. Our estimate of the signal/noise ratio for individual compartments due to electronic noise is $\sigma_{A\to D}$ = 0.3 GeV $\sqrt{C(\mu F)}$, [8] $\sigma_{E\to G}$ = 1.0 GeV $\sqrt{C(\mu F)}$, and σ_{H} = 4.0 GeV $\sqrt{C(\mu F)}$. Therefore, if one assumes that 10% of the detector were to be used for a trigger, the noise contribution would have $\sigma \simeq 2.3$ GeV.

5.6 DEPLETED URANIUM PROCUREMENT

We have already begun to develop contacts with commercial firms dealing in depleted Uranium (most U^{235} has been removed).

National Lead Ohio (NLO) has as a byproduct of its smelting operations 250 tons of "top-crop" Uranium, which is available at present. This form of Uranium is unsuitable for military applications because the carbon content exceeds 500 ppm, but has been used for calorimetry at CERN. The projected requirements of the U. S. weapons program assure a continuing supply of top-crop, perhaps sufficient for the entire calorimeter.

There may also be alternative sources of the metal at various DOE sites, but, in the event that not enough of the metal can be found, NLO will reduce UF_4 (green salt) to metallic Uranium at a price of $5/kg.

The uranium plates used in Experiment R807 were rolled and sheared by Rockwell International at their Rocky Flats plant in Golden, Colorado. The 150 tons of 2 mm and 3 mm plates were produced in approximately one calendar year for a cost of $1 M ($6/kg). This plant has the capacity and the expertise to handle the rolling and shearing of the ≈700 tons required by this experiment.

A new company, Material Science Corp., plans to found a Uranium rolling mill at Oak Ridge, Tennessee. They have entered a bid to supply over 200 tons of Uranium plates for the proposed upgrade of UAl at a cost of about $9/kg. The price includes recasting the base uranium (e.g., top crop) into suitable ingots, then rolling and shearing. They estimate they will need ≈0.5 calendar years for this amount. The plates needed for this experiment could be fabricated in about 1 year.

REFERENCES CHAPTER 5

1. W. J. Willis and V. Radeka, Nucl. Instrum. Methods **120**, 221 (1974); J. H. Cobb et al., Nucl. Instrum. Methods **158**, 93 (1979); C. W. Fabjan et al., Nucl. Instrum. Methods **141**, 61 (1977).

2. T. Åkesson et al., Phys. Lett. **118B**, 185 (1982).

3. ISR Experiment R807 internal note 263 (6/24/81).

4. A. Guy and P. Mockett, SLD Note 102.

5. G. Abrams, D. Hitlin, and A. Langford, draft paper and private communication.

6. Hermetic Seal Corporation, part number XP960504-22B-55P-1.

7. D. Brown, BNL, private communication.

8. V. Radeka, private communication.

TABLE 5.1 LONGITUDINAL SEGMENTATION OF THE CENTRAL CALORIMETER

Layer	Plate Thickness (mm)	# cells	Layer Thickness (X_0)	Layer Thickness (λ_0)	Distance From Front Plate (cm)
A	1.5	4	2		0.0
B	1.5	4	2	0.7	2.2
C	1.5	12	6		4.4
D	1.5	28	14		11.0
E	4.0	25		1.0	26.4
F	4.0	35	192	1.4	46.4
G	4.0	45		1.8	74.4
H	20.0	10		2.0	110.4
Total	-	163	216	6.9	134.4

TABLE 5.2 TRANSVERSE SEGMENTATION IN CENTRAL CALORIMETER

Layer	Type of Readout	# Towers Within Module ($z \times \phi$)	Dimensions of Cell (cm) in z	in ϕ	# Readouts
A	pads	14 × 5	6	≃6.1	3360
B	pads	14 × 5	6	≃6.3	3360
C	pads	14 × 5	6	≃6.6	3360
C	z strips	84 × 1	1	≃33.2	4032
C	ϕ strips	3 × 30	30,30,24*	≃1.1	4320
D	pads	14 × 5	6	≃7.6	3360
E	pads	6 × 2	14	≃22.6	576
F	pads	6 × 2	14	≃27.5	576
G	pads	6 × 4	14	≃17.1	1152
H	pads	6 × 4	14	≃20.2	1152
				Total	25248

*These dimensions are chosen to align edges with tower boundaries.

TABLE 5.3 READOUT CAPACITANCES IN THE CENTRAL CALORIMETER

Layer	Type of Readout	Total Area (m^2)	<C>/Readout (nF)	C_{tot} (μF)
A	pads	49	0.276	0.93
B	pads	50	0.284	0.95
C	pads	160	0.301	3.03
C	z strips	160	0.251	3.03
C	ϕ strips	160	0.30	3.03
D	pads	426	2.40	8.06
E	pads	454	14.90	8.58
F	pads	1123	25.46	14.66
G	pads	1237	20.20	23.39
H	pads	324	5.33	6.14
Total		3823		65.74

FIGURE CAPTIONS - CHAPTER 5

5.1 End view of central ULA calorimeter.

5.2 Pad boundaries for central ULA calorimeter in r-ϕ and r-z views of a typical module.

5.3 Pad ϕ-z segmentation in EM section (layers A, B, C, D) and hadronic section (layers E, F, G, H). Also shown are the strips in layer C.

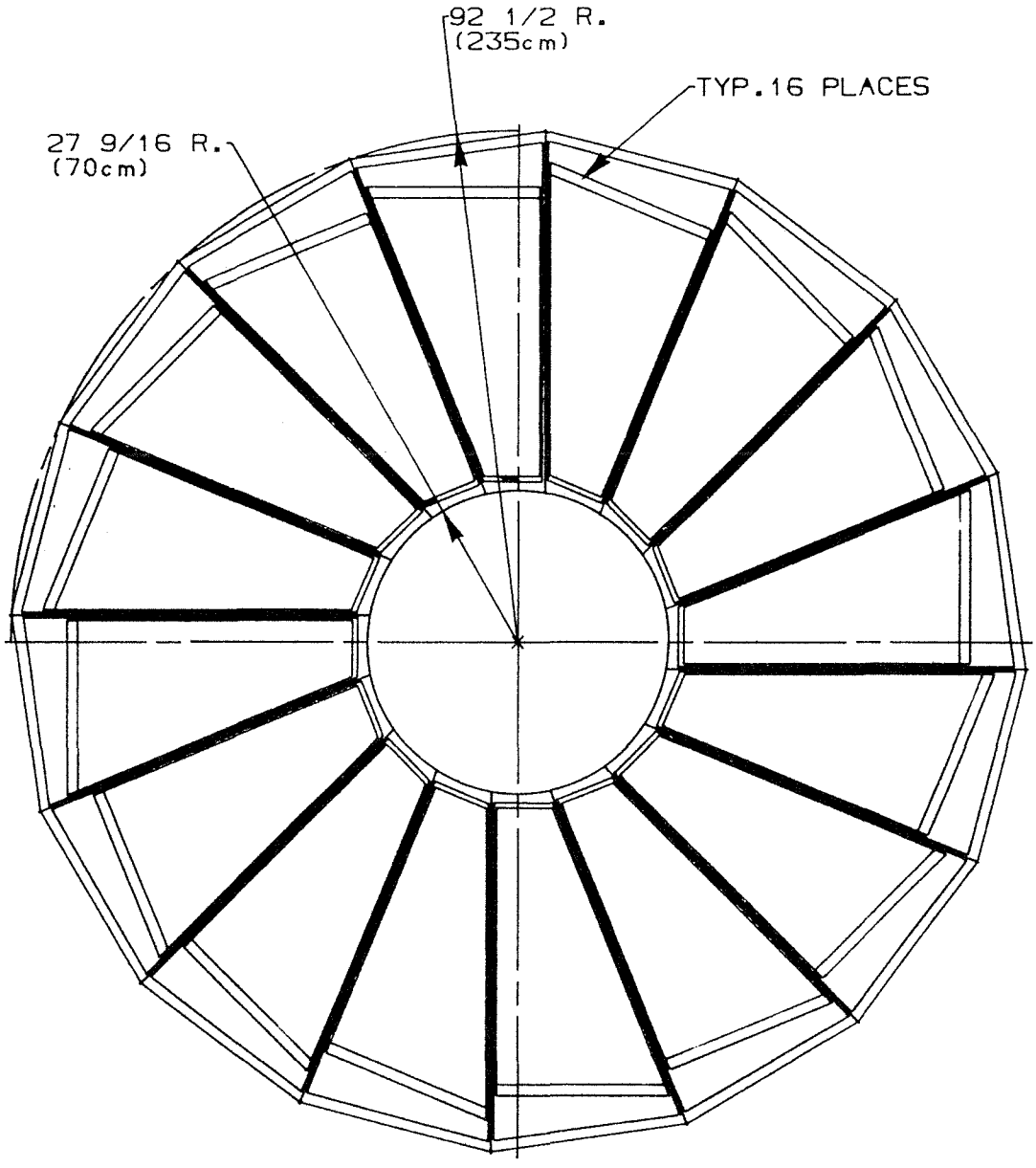

VIEW SHOWN WITHOUT ENDPLATES

Fig.5.1

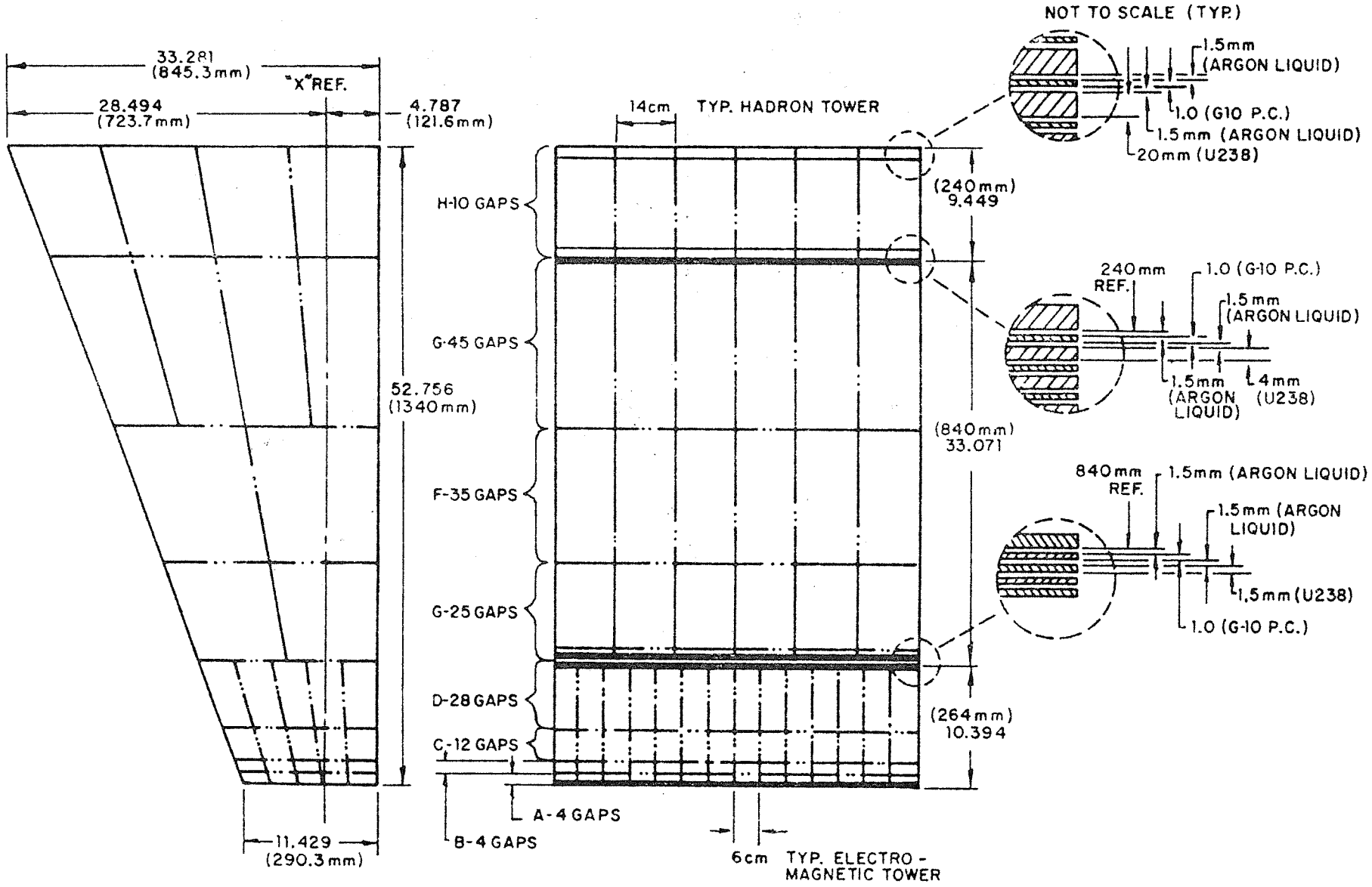
NOT TO SCALE (TYP.)
33.281
(845.3mm)
"X" REF.
28.494
(723.7mm)
4.787
(121.6mm)
52.756
(1340mm)
11.429
(290.3mm)
14cm TYP. HADRON TOWER
H-10 GAPS
G-45 GAPS
F-35 GAPS
G-25 GAPS
D-28 GAPS
C-12 GAPS
A-4 GAPS
B-4 GAPS
6cm TYP. ELECTRO-MAGNETIC TOWER
(240mm)
9.449
(840mm)
33.071
(264mm)
10.394
1.5mm
(ARGON LIQUID)
1.0 (G10 P.C.)
1.5mm (ARGON LIQUID)
20mm (U238)
240mm
REF.
1.0 (G-10 P.C.)
1.5mm
(ARGON LIQUID)
1.5mm
(ARGON LIQUID)
4mm
(U238)
840mm
REF.
1.5mm (ARGON LIQUID)
1.5mm (ARGON
LIQUID)
1.5mm (U238)
1.0 (G-10 P.C.)

Fig. 5.2

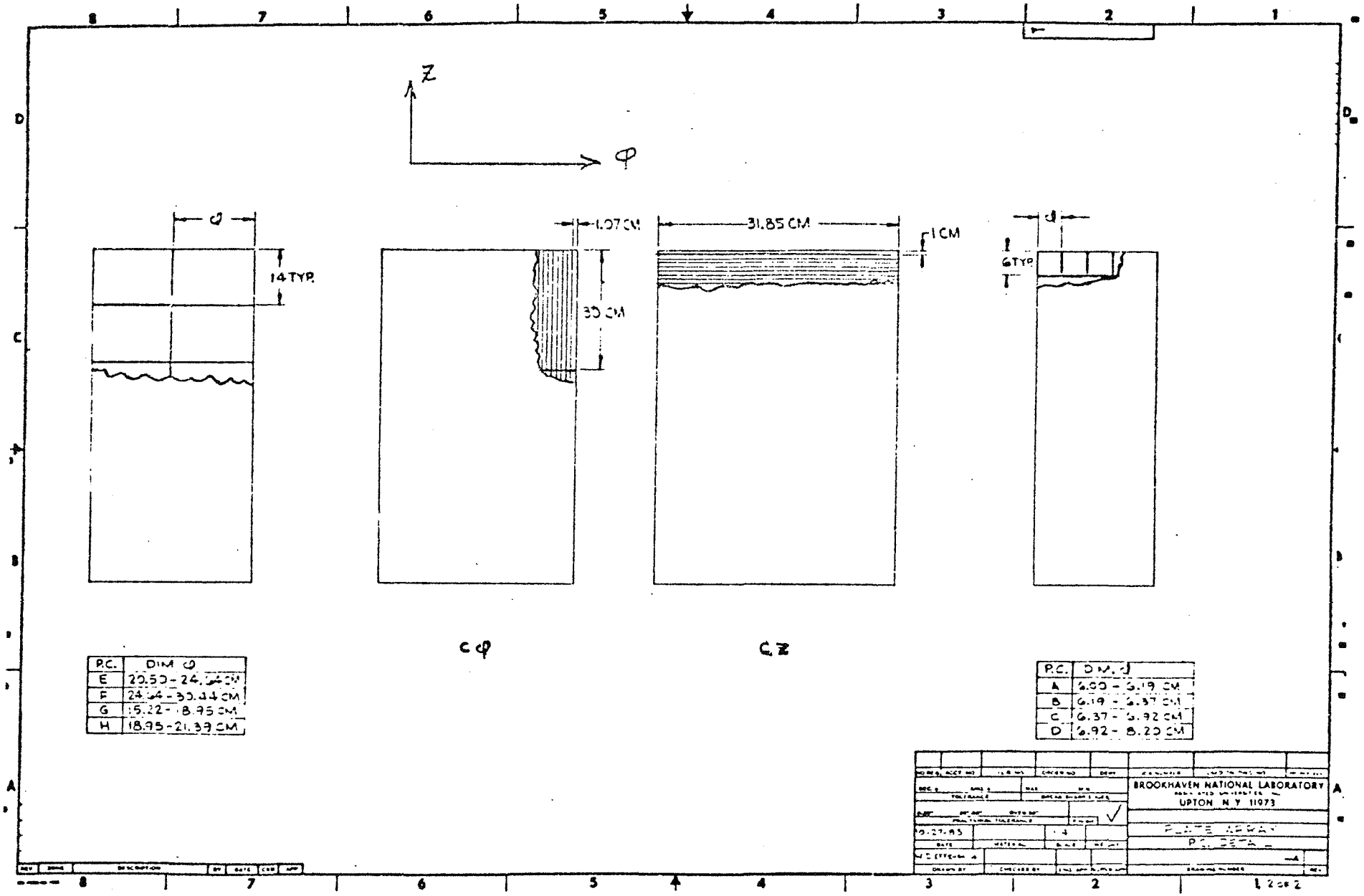
Z
φ
d
14 TYP.
1.07 CM
31.85 CM
1 CM
30 CM
d
6 TYP.
c φ
c z
P.C. | DIM d
E | 20.50 - 24.64 CM
F | 24.64 - 30.44 CM
G | 15.22 - 18.95 CM
H | 18.95 - 21.39 CM
P.C. | DIM. J
A | 4.00 - 5.19 CM
B | 5.19 - 6.37 CM
C | 6.37 - 6.92 CM
D | 6.92 - 8.20 CM
BROOKHAVEN NATIONAL LABORATORY
UPTON N.Y. 11973

Fig. 5.3

6. THE END-CAP CALORIMETERS

6.1 INTRODUCTION

The Uranium Liquid-Argon end-cap calorimeters which cover the forward and backward beam directions from 5° to 45° provide both electromagnetic and hadronic energy measurements. The electromagnetic (EM) section of the end is 24 radiation lengths (X_0) in depth and is expected to give an energy resolution for EM particles of $0.11/\sqrt{E}$. The entire end cap is 8.9 absorption lengths (λ_0) and is expected to have a hadronic energy resolution of $0.35/\sqrt{E}$.

The end caps shown in Figs. 6.1 and 6.2 cover the angles from 5° to 30° without obstruction and from 30° to 45° shadowed by the central calorimeter. The active volume of the detector extends from 1.6 m to 3.4 m along the beam, relative to the center of the interaction region. The radius of the active area is 2.0 m.

6.2 CELL STRUCTURE AND LONGITUDINAL SEGMENTATION

6.2.1 Cell Structure

The basic cell structure for both EM and hadronic parts of the end cap calorimeter is shown in Fig. 6.3. Each cell consists, in sequence, of a uranium plate, a 2 mm-thick liquid argon gap, two copper-clad G-10 boards with a total thickness of 1.6 mm, and a final 2 mm liquid argon gap. The G-10 boards have an identical pad configuration for each cell (see Section 6.3). The pads face the argon gaps; readout leads are carried between the pair of G-10 boards to the periphery of the detector. This cell structure repeats throughout the depth of the detector with the only difference being the thickness of uranium plates in the various longitudinal segments.

There are three functionally distinct longitudinal sections for the detector. The first is a very finely segmented EM calorimeter; second is a less fine-grained hadronic section; and finally there is a coarsely segmented hadronic "leakage" section. The uranium plate thickness for each longitudinal section are 1.5 mm, 4.0 mm, and 20.0 mm respectively. The general parameters of each type of cell are given in Table 6.1.

As discussed in Section 5.2, various alternatives to this cell structure and longitudinal arrangement are being considered.

6.2.2 Longitudinal Segmentation

The design goal of 24 X_0 for the EM calorimeter and the overall space restriction on the length of the end cap, along with the cell structure set the basic parameters of the longitudinal structure. The lengths, in various units, of the several sections are given in Table 6.2

6.3 READOUT BOARDS, PADS, SEGMENTATION

6.3.1 General Pad and Lead Considerations

Identical pads from both sides of the G-10 boards are OR'ed together between the boards and brought radially to the periphery of the G-10 on etched signal lines. Signals are ganged together along the edge of the calorimeter to form the longitudinal segments and brought to the backplate of the end cap by twisted-pair wire where they make the transition from liquid argon to the outside via feed-thru connectors.[2] (Liquid argon to vacuum and vacuum to air connectors are necessary.) These signal cable lengths are up to 200 cm for this geometry.

6.3.2 Pad Transverse Segmentation

In all sections of the EM and hadronic end cap calorimeters, pads have a Δr, $\Delta\phi$ structure. The design criterion for Δr is taken from

$$\Delta\eta = \frac{\Delta r}{r} \frac{1}{\sqrt{1 + r^2/d^2}} = 0.1,$$

where d is the distance along the beam to the readout plane and r is the radial distance from the beam in the plane of the G-10 boards. The specification for $\Delta\phi$ is $\Delta\phi = 2\pi/64 = 5.625°$, to match the anticipated segmentation of the boards themselves. Therefore the polar angle interval from $\theta = 5°$ ($\eta \simeq 3$) to $\theta = 40°$ ($\eta \simeq 1$) is subdivided into 20 segments and the ϕ region into 64 segments. This pad structure is shown in Fig. 6.4. This transverse pad structure is continued through the depth of the detector. While this fine granularity leads to pads smaller than 3×3 cm^2 near 5° in the hadronic sectors, considerably finer than needed for hadronic showers, the strategy has been adopted to maintain the fine pad structure and gang pads together where appropriate.

In addition to the pads, there will be a very fine-grained set of r, ϕ strips in the 6 X_0 EM subsection. These are shown in Figs. 6.5 and 6.6. These are included for photon position determination and for fine structure of jets.

6.3.3 Longitudinal Ganging of Pads

Figure 6.7 shows the longitudinal ganging of pads and illustrates the projective nature of the pad structure. In general, this ganging will be done inside the cryostat but flexibility will be retained to bring out more longitudinal segments in the case of the EM section. The EM sections are

subdivided into 2, 2, 6, 14 X_0 portions ($0.95\lambda_0$), while the hadronic sections are 3.0, 3.0, 2.0 λ_0.

6.3.4 Detector Capacitance and Signal/Noise

With the detector pad structure and longitudinal ganging as described above, the capacitance and signal to noise ratios can be computed for each cell. For example, the largest cell in the EM portion ($A = 0.14 \times 0.11$ m^2) has C = 204 pF. Ganging 4 such cells yields 816 pF. If we take into account the twisted pair lead capacitance for the most inaccessible pad, this capacitance increases to 1130 pF.

For this particular set of cells, the noise is estimated by $5\times10^5 \sqrt{C(\mu F)}$. With $dE/dx = 2.5\times10^6$ eV/cm, ionizing energy = 23.6 eV, and 1.6 cm path length, we estimate

$$\text{Signal/Noise} = 8.45 \times 10^4 \text{ electrons}/1.62 \times 10^4 \text{ electrons}$$
$$\sim 5/1,$$

for minimum ionizing particles.

6.3.5 Channel Count

The number of channels required to instrument the pad structure shown in Figs. 6.4 and 6.7, segmented into 4 EM sections and 3 hadronic sections is approximately 10^4. If in the inner section of the hadronic calorimeter, we gang together adjacent Δr and $\Delta\phi$ pads, the count is reduced to about 7000. The r, ϕ strips contribute another 2320 channels (784 for ϕ and 1536 for r) to make a grand total of about 9300 channels of electronics required per end cap.

6.4 MECHANICAL CONSTRUCTION

6.4.1 Detector Mechanics

The mechanical construction of the detector plate assembly is dictated to some extent by the size of uranium plates that can be constructed. Plates of 27 inches in width, 1.5 mm thick with thickness tolerances of ± 0.04 mm can be fabricated.[3] A design in which each two-meter radius detector plate is assembled from smaller pieces, welded, ground, and dressed to form the full plate is being investigated. The full plate with suitable spacers and the G-10 readout boards are then bolted together in manageable longitudinal portions of the complete detector. These longitudinal subassemblies are then hung from the support structure which is inserted into the cryostat in the final detector assembly.

If tolerances cannot be maintained on the full plate structure, an alternate scheme is suggested in which a module comprising 1/16 of the detector would be assembled as a unit. The 16 modules would then be held relative to each other by a mechanical support structure inside the cryostat. This alternative technique would have the advantage of allowing 1/16-size subunits to be assembled for testing at the expense of having to support and position the submodules separately. Preliminary engineering studies for this scheme are shown in Figs. 6.8 and 6.9. In either case, the modules that have to be handled would be approximately 10-20 tons. Neither assembly technique will result in any cracks for the detection of particles.

6.4.2 Cryostat and the Cryogenic System

A cylindrical cryostat, large enough to contain the entire end-cap detector provides vacuum thermal insulation for the liquid argon inventory (~10 tons/end cap). Access to the cryostat volume for insertion of the detector

would be from the rear of the cryostat. Indium seals form the wet seal for the liquid argon volume at the 5° hole, on the front surface of the liquid argon container and at the outer surface of the argon container at the rear plate of detector. If the indium seals prove impractical, a totally welded argon container can be used. Such a vessel would be ground open if necessary. The outer air-vacuum wall will be sealed with conventional techniques. Figures 6.1 and 6.2 show the general configuration of such a cryostat.

While the rear wall of the cryostat may be thick, care must be taken to insure that the upstream end of the cryostat be thin to maintain good energy resolution of the electromagnetic section. A torispherical surface is planned which would bow outward to withstand the atmospheric pressure on the vacuum space. With this surface contour a thickness of $\leq$ 2 cm of steel (1.14 X_0) can be achieved. The argon container can be $\leq$ 1 cm (0.56 X_0) thick. It is expected that an optimized design will reduce the space and thickness required for the front wall. In order to minimize the effect of this wall, an argon-G-10-argon cell will precede the first uranium plate. The wall of the cryostat will then effectively be incorporated into the detector structure.

The refrigeration for the liquid argon volume will be provided by a liquid N_2 system composed of a N_2 storage dewar (15,000 liters) which supplies liquid N_2 to a simple heat exchanger placed at the top of the end-cap cryostat above the liquid-gas interface. A liquid argon storage vessel of comparable size will be needed. The flow rate will be regulated by the pressure of argon gas in the detector which will be maintained at approximately 1 ± 0.05 atmosphere absolute. (For safety purposes, relief valves on the liquid argon volume will be set at 2 psi gauge). The ports for the liquid N_2 and liquid argon plumbing and for the cryogenic instrumentation will be situated at the top rear of the end cap. Considering heat leaks due to the large number of signal wires and the support, 300 liters/day of liquid N_2 will be required.

The O_2 contamination will be monitored to better than 0.1 ppm by commercially available instrumentation. Sampling the argon in the cryostat, the level of contamination will be kept to less than 1 ppm by recirculation of the liquid argon through a molecular sieve purification system. Operation with methane is not necessary, thereby eliminating one usual source of electron attaching impurities.

The need for circulation to maintain uniform temperature and density to better than 1% is recognized. Natural convection and forced convection techniques are being studied.

REFERENCES CHAPTER 6

1. We are grateful to the E706 collaboration for making their internal memos available to us and for sharing their expertise on liquid argon systems. We also acknowledge useful conversations with W. Carrithers and D. Hitlin.

2. Hermetic Seal Corp., part number X960504-22B-55P-1.

3. Tolerance source: D. Floyd, Manufacturing Sciences Corporation.

TABLE 6.1

	Uranium	Liquid Argon	G-10	Total
E.M.	1.5 mm/0.47 X_0/0.014 λ_0	4 mm/0.029 X_0/0.0049 λ_0	1.6 mm/0.010 X_0/0.0029 λ_0	7.1 mm/0.509 X_0/0.0221 λ_0
Fine Hadron	4.0 mm/1.25 X_0/0.038 λ_0	4 mm/0.029 X_0/0.0049 λ_0	1.6 mm/0.010 X_0/0.0029 λ_0	9.6 mm/1.289 X_0/0.0459 λ_0
Coarse Hadron	20.0 mm/6.25 X_0/0.191 λ_0	4 mm/0.029 X_0/0.0049 λ_0	1.6 mm/0.010 X_0/0.0029 λ_0	25.6 mm/6.289 X_0/0.1983 λ_0

TABLE 6.2

	Thickness	No. of Cells	Weight
EM	33.4 cm/24 X_0/0.95 λ_0	47	~18.5 tons
Fine Hadron	121.0 cm/162 X_0/5.92 λ_0	126	~130.4 tons
Coarse Hadron	25.6 cm/63 X_0/1.98 λ_0	10	~51.4 tons
Total	180.0 cm/249 X_0/8.85 λ_0	183	200.3 tons

FIGURE CAPTIONS - CHAPTER 6

6.1 Side view of End-Cap Calorimeter

6.2 Front view of End-Cap Calorimeter

6.3 Cell structure of Uranium/Argon/G10

6.4 Pad segmentation at front face of calorimeter

6.5 Strip layout in one sector (r-strips)

6.6 Strip layout in one sector (ϕ-strips)

6.7 Schematic side view of readout segmentation

6.8 Preliminary engineering study for end-cap plate supports

6.9 Preliminary study for support of end-cap submodules

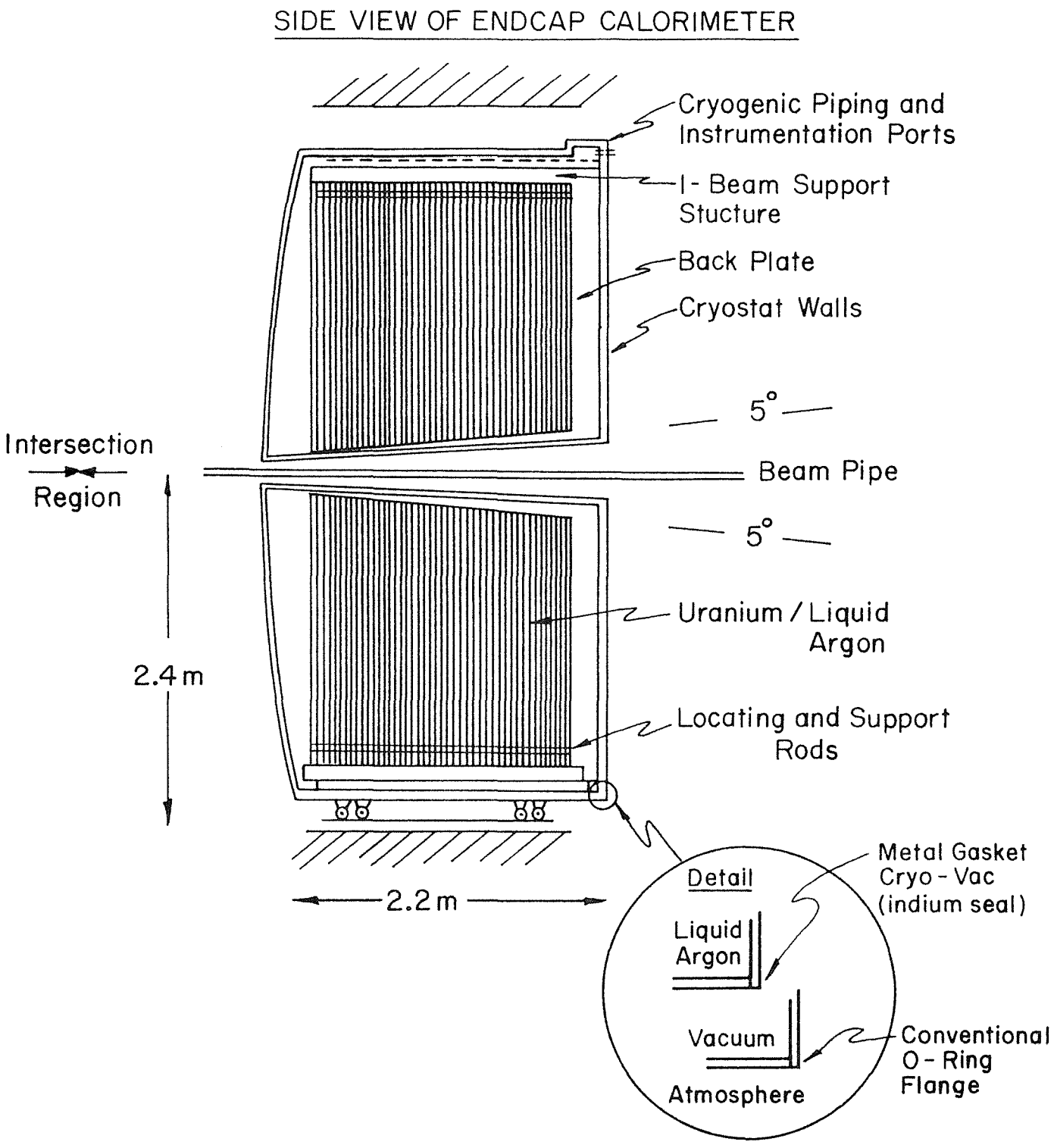
SIDE VIEW OF ENDCAP CALORIMETER
Cryogenic Piping and Instrumentation Ports
I- Beam Support Stucture
Back Plate
Cryostat Walls
5°
Intersection Region
Beam Pipe
5°
Uranium / Liquid Argon
2.4 m
Locating and Support Rods
2.2 m
Detail
Metal Gasket Cryo - Vac (indium seal)
Liquid Argon
Vacuum
Atmosphere
Conventional O - Ring Flange

Fig. 6.1

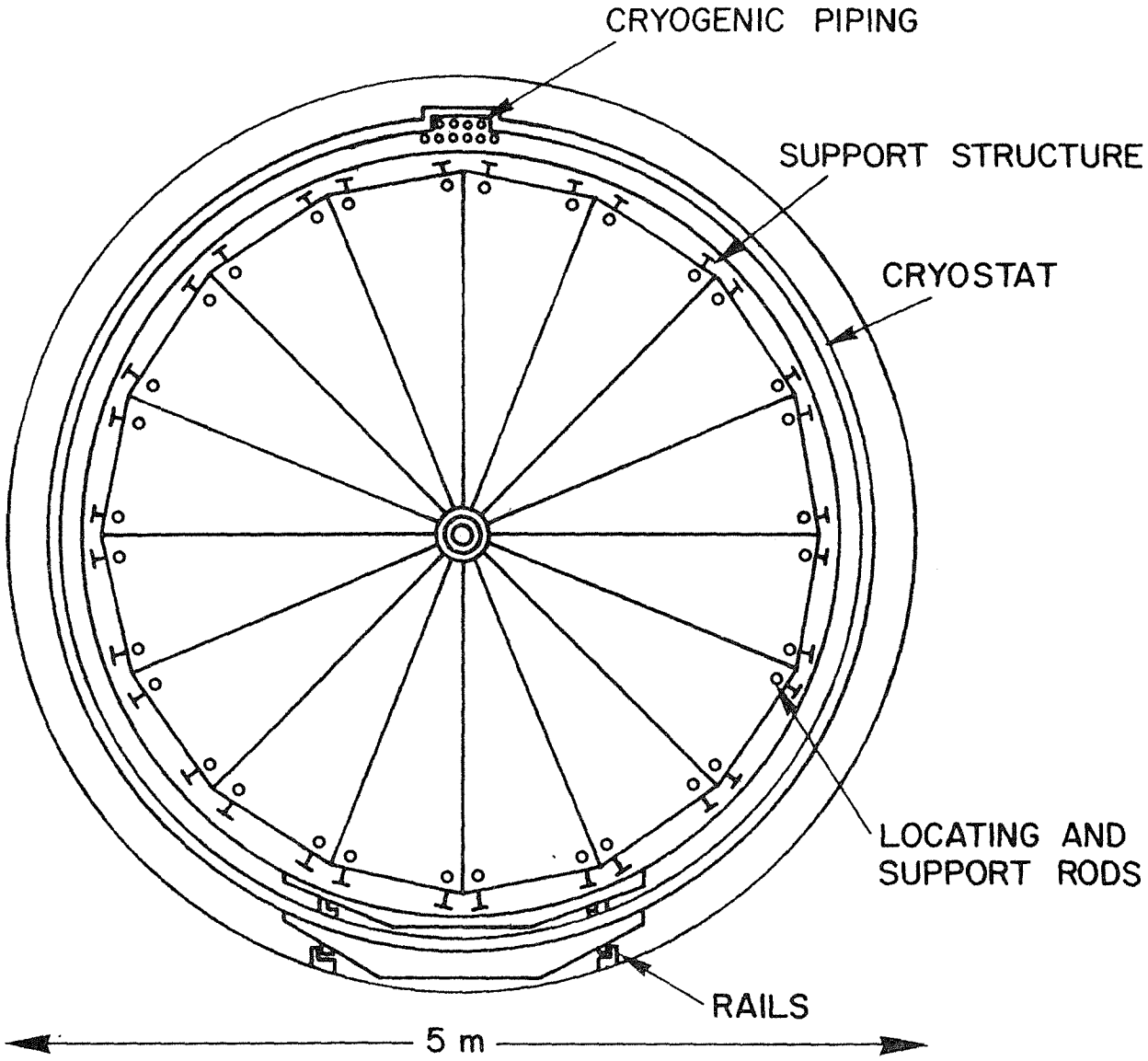
CRYOGENIC PIPING
SUPPORT STRUCTURE
CRYOSTAT
LOCATING AND
SUPPORT RODS
RAILS
5 m

Fig. 6.2

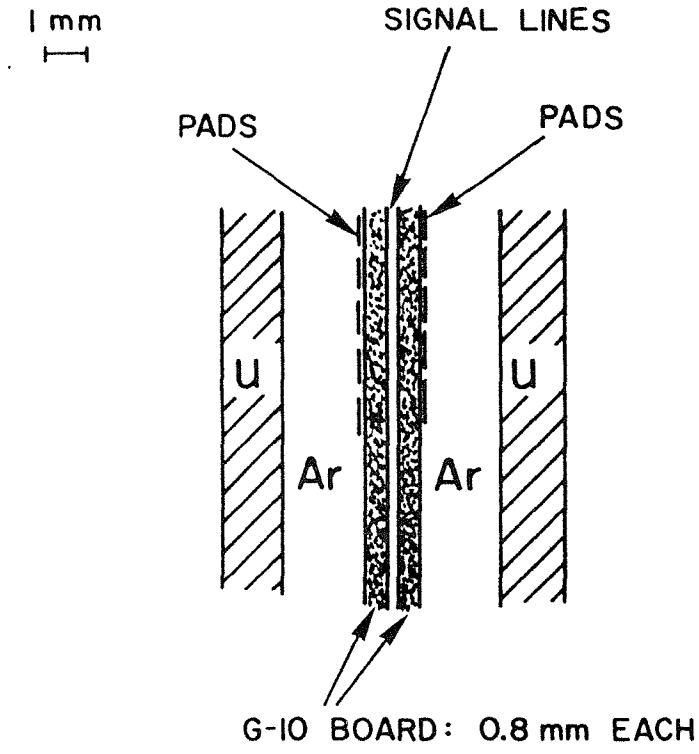

- Identical Pad Structure on Both Sides of G-10.
- Resistive Coated Mylar Covering Pads.
  Resistive Coat Faces The Argon and is at Positive HV.

CELL STRUCTURE IN EM SECTION OF ENDCAP

Fig. 6.3

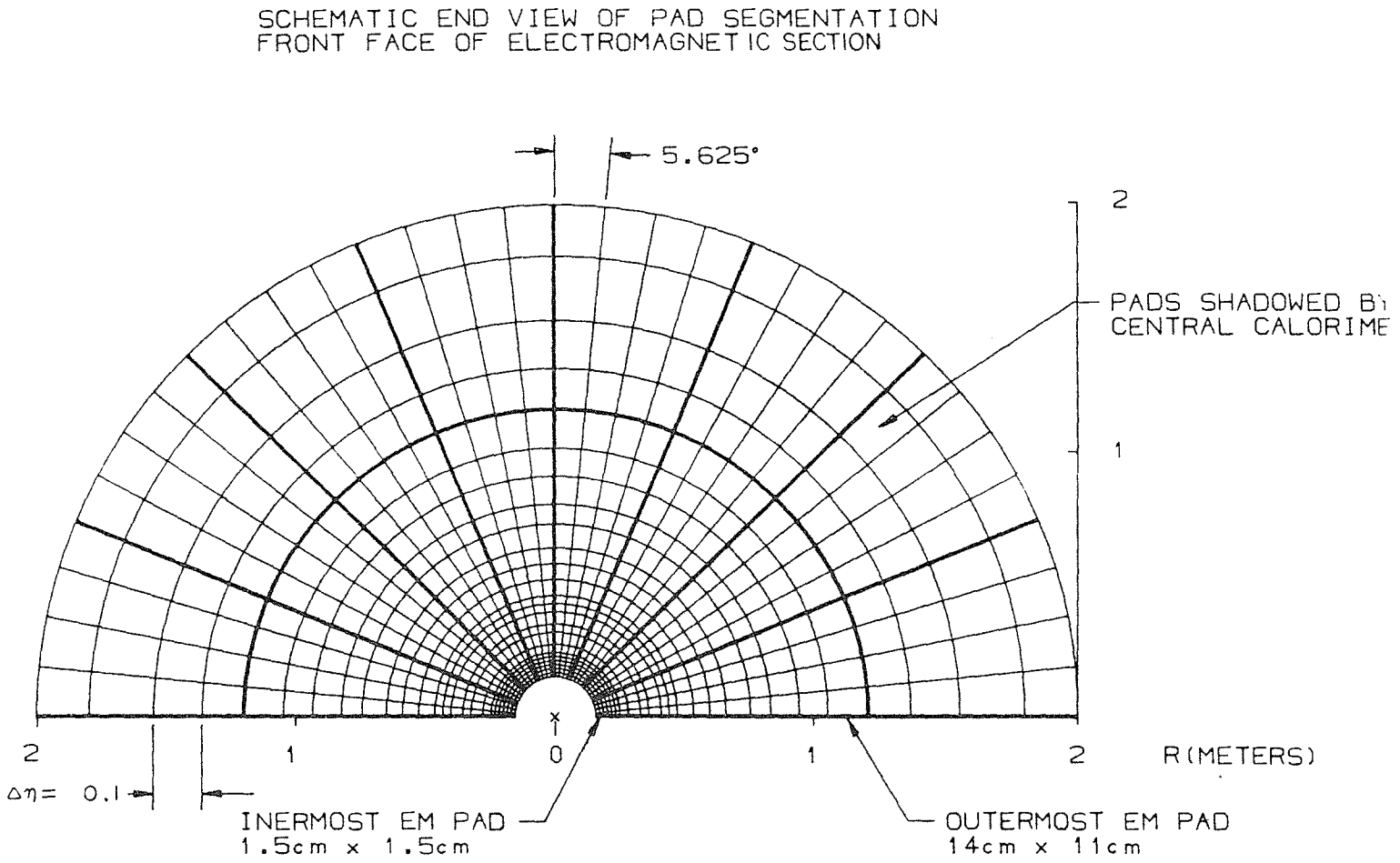
SCHEMATIC END VIEW OF PAD SEGMENTATION
FRONT FACE OF ELECTROMAGNETIC SECTION
5.625°
2
PADS SHADOWED BY
CENTRAL CALORIME
1
2
1
0
1
2
R(METERS)
Δη= 0.1
INERMOST EM PAD
1.5cm x 1.5cm
OUTERMOST EM PAD
14cm x 11cm

Fig. 6.4

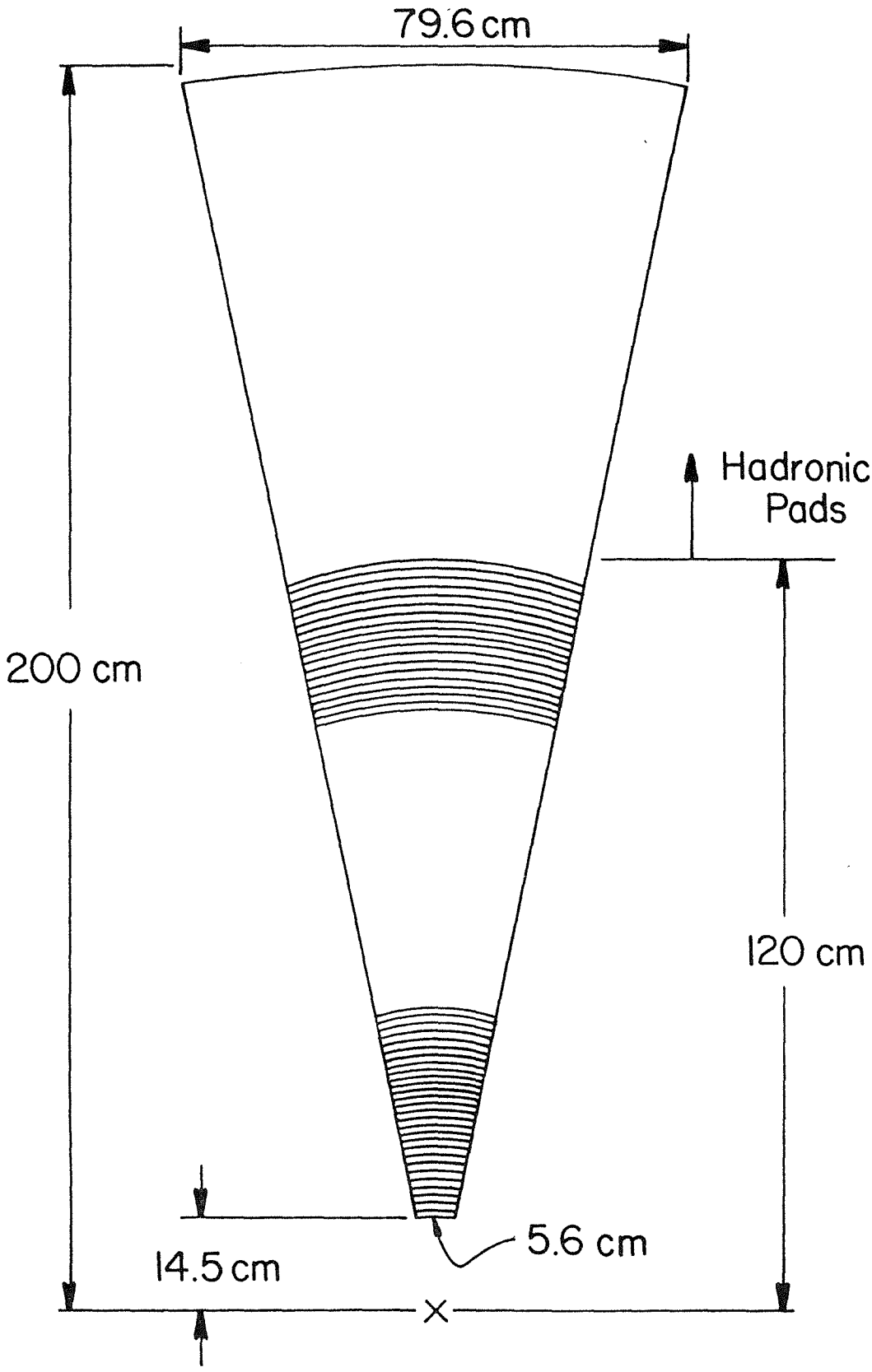

Total No. Strips is 96, each 1cm wide with a space of 0.1 cm

Fig. 6.5

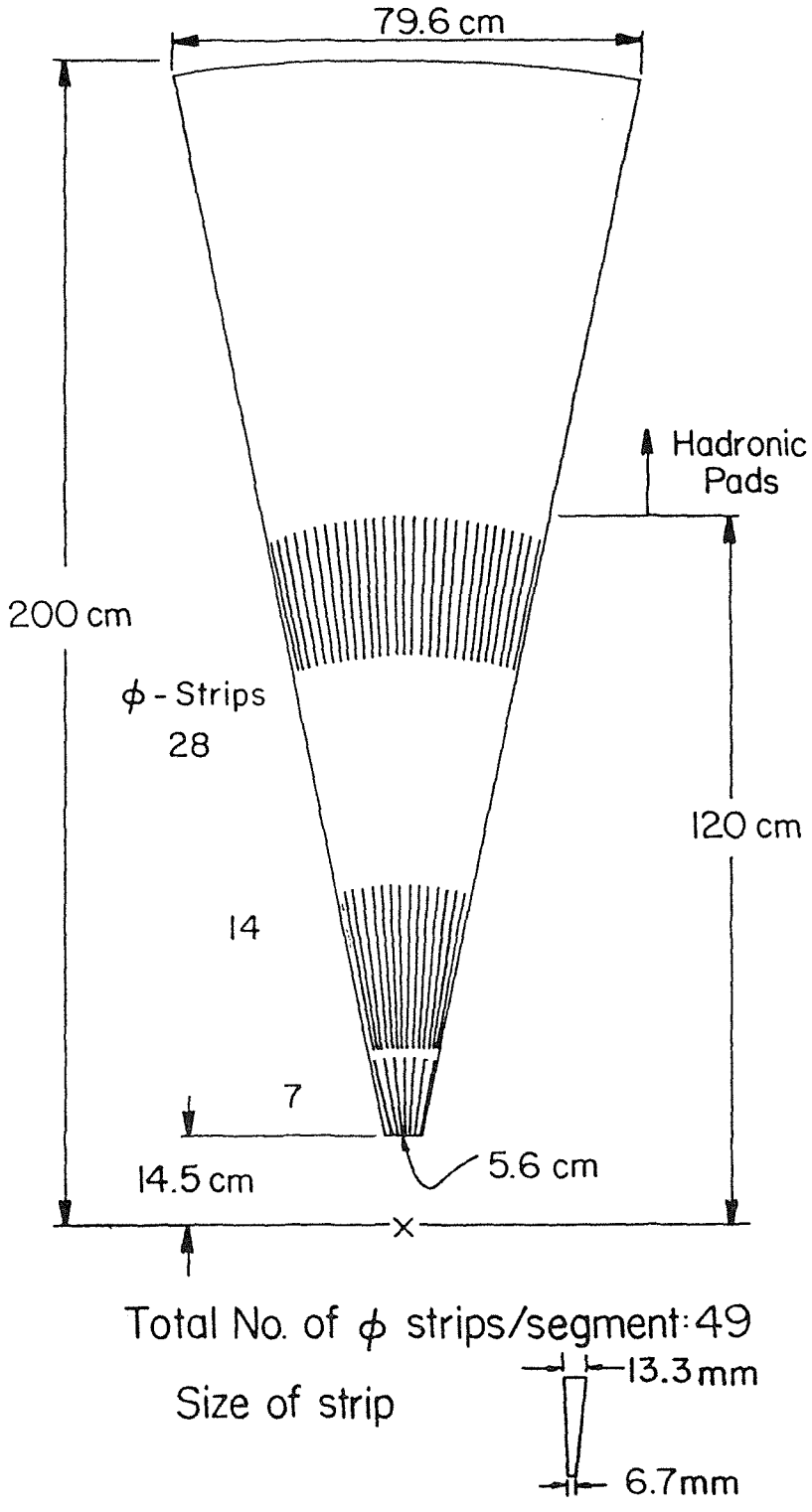
79.6 cm
Hadronic
Pads
200 cm
φ - Strips
28
14
7
120 cm
14.5 cm
5.6 cm
Total No. of φ strips/segment: 49
Size of strip
13.3mm
6.7mm

Fig. 6.6

SCHEMATIC SIDE - VIEW OF READOUT SEGMENTATION

END CAP CALORIMETER

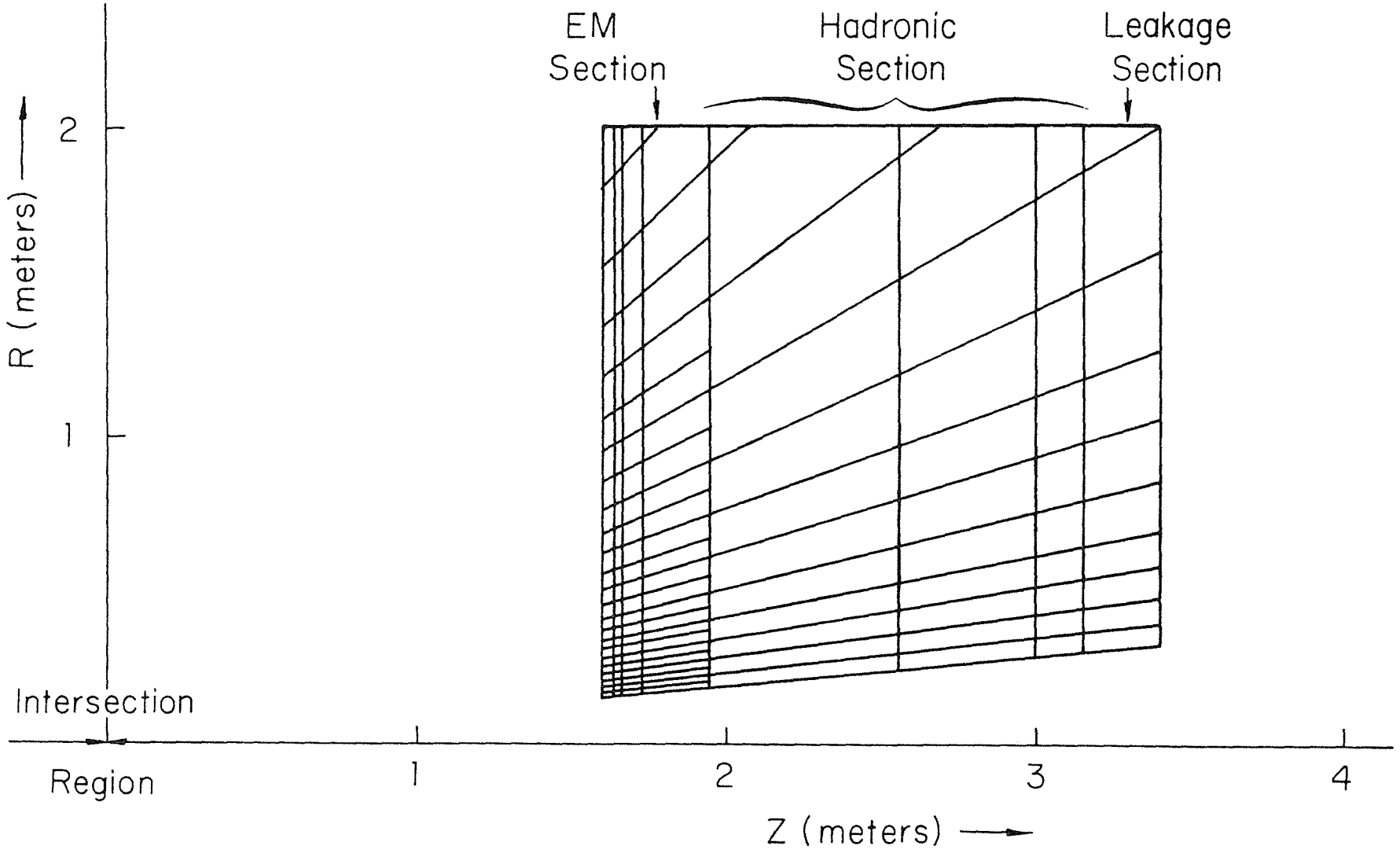

Fig. 6.7

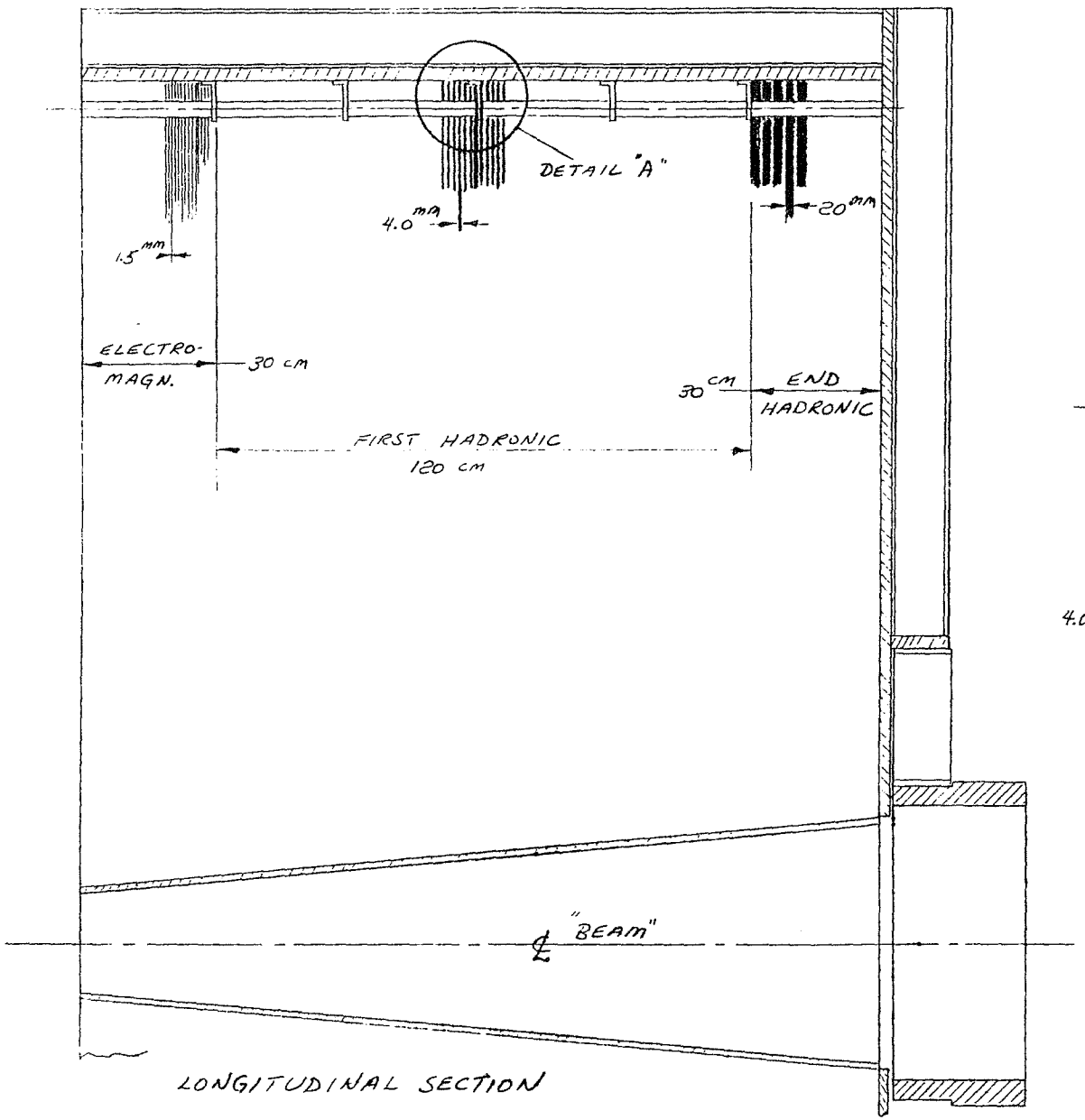

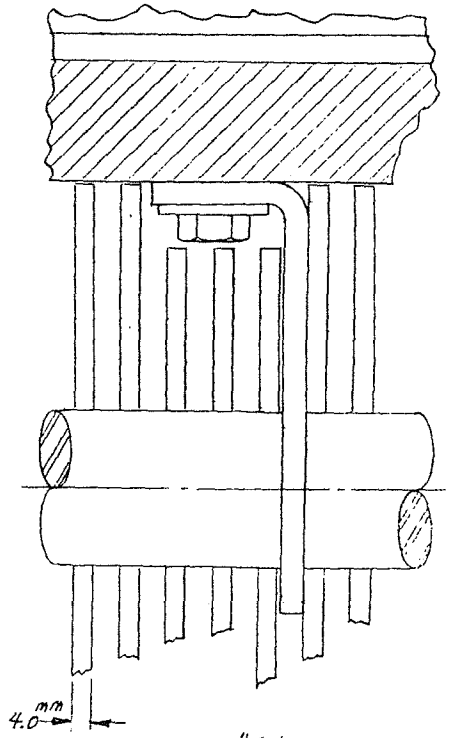

Fig. 6.8

DEPT. OF PHYSICS MICHIGAN STATE UNIVERSITY		
CALORIMETOR U-L.A.		
FEF	11-1-83	1005
10:1	173-23	

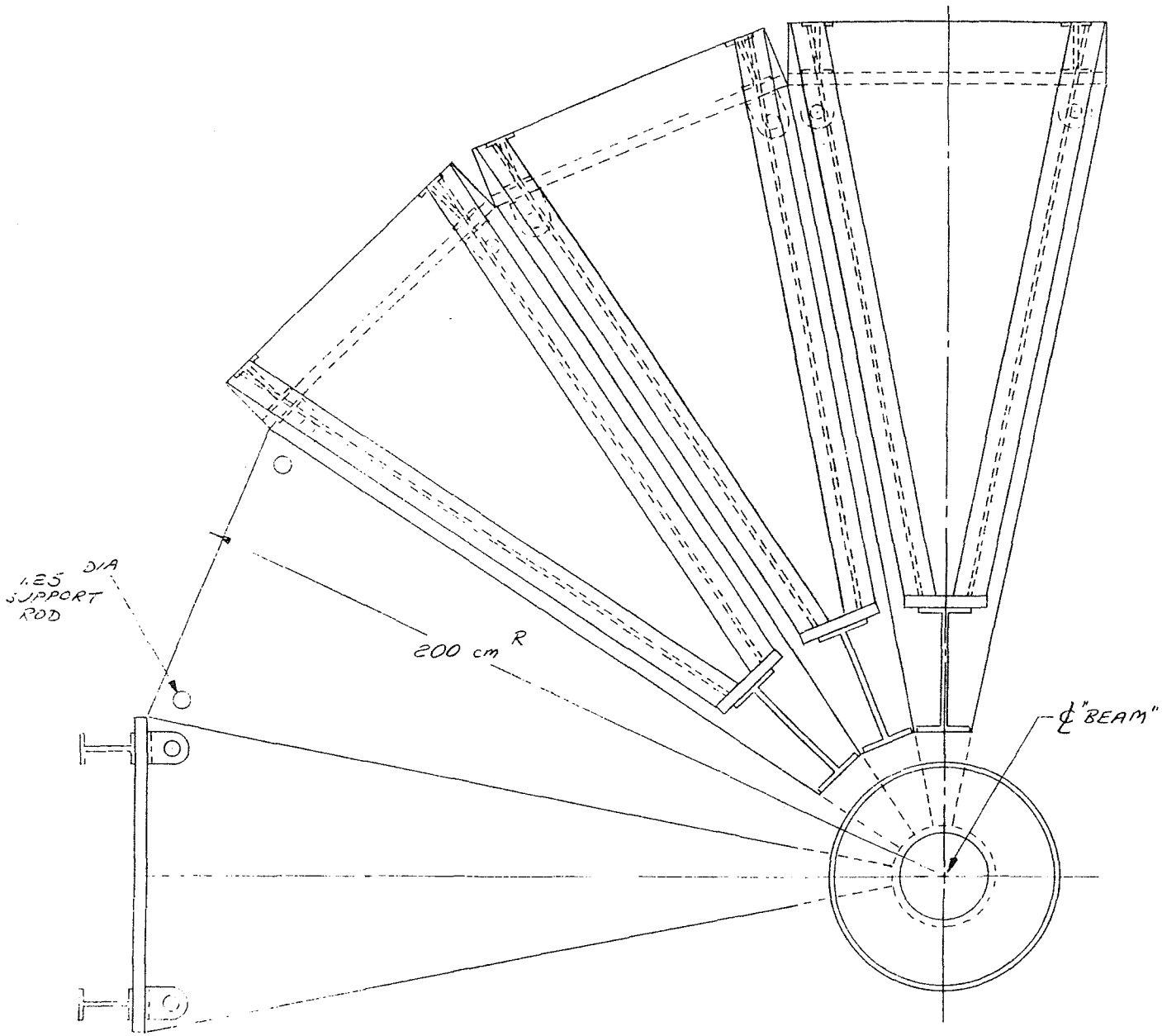

SUPPORT STRUCTURE
END VIEW
LOOKING "UP-BEAM"

Fig. 6.9

DEPT. OF PHYSICS MICHIGAN STATE UNIVERSITY		
CALORIMETOR U-L.A.		
FEF	11-1-83	1004
10:1	173-23	

7. THE END-PLUG CALORIMETER

7.1 INTRODUCTION

The small angle region, with angles below 5 degrees is an important one for two reasons:

1. Calculations show that missing-p_T studies will have a large background from particles lost down the beam hole unless measurements with good resolution are made down to about 1 degree (see Fig. 3.1).
2. A large part of rapidity phase space is represented by angles below 10 degrees--close to half of the total useful rapidity range lies in this interval.

Point 2 has several consequences. Two of the most important are the following:

a) Many events will have significant or dominant energy contributions from the outgoing particles in this angular range.

b) The typical event will have at least 10 to 15 "soft" particles in the region within 10 degrees of each beam; the p_T vectors of these particles must be measured with good accuracy in order to determine whether p_T is or is not balanced by the visible particles in the event.

7.2 DESIGN CONSIDERATIONS

The above considerations, when examined quantitatively, lead to the conclusion that the small angle region covered by the end plug should have towers of size not much larger than $\Delta\eta = 0.15$. At the same time the minimum useful tower size, in transverse dimensions, is of order 5 cm, the scale being set by the shower size and position uncertainty for hadron cascades for

energies of principal interest in high-p_T events--energies of 10 to 200 GeV at 5 degrees, for example. Uranium has an appreciable advantage over iron, not only because of the much better energy resolution obtainable for hadrons and jets, but also because the short absorption length results in reduced shower size and thus permits the use of smaller towers.

7.3 TRANSVERSE AND LONGITUDINAL SEGMENTATION

The end-plug design derived from these considerations is shown in Fig. 7.1 and Fig. 7.2, and is described in some detail in Tables 7.1 and 7.2. Below 2 degrees the inner rings are more limited in $\Delta\eta$ resolution but are still quite useful. The innermost and outermost rings serve in effect as guard rings. The end-plug has a total length of about 2 meters, and a mass of about 15 tons (10 tons U and 5 tons Fe) for coverage to about 5 degrees.

The design shown has 360 hadron towers per end-plug. Sampling in depth will be done with 4 samples in the EM section, 2 in the next 5 λ_0 of uranium, and 1 in the final 3 λ_0 of Fe. This would give 2520 readout channels per end plug. In addition, EM showers will be localized more sharply by finer pad readout of the second depth segment (4 X_0). Pads of about 1.5 × 1.5 cm will give about 2500 additional channels, making a total of 5000 readouts per end plug.

Mechanical construction and cryogenics are not discussed here. The problems involved are similar to those for the end cap discussed in Chapter 6, but are considerabaly less difficult.

TABLE 7.1 LONGITUDINAL SEGMENTATION

DEPTH STRUCTURE OF END PLUG CALORIMETER

CALORIMETER SECTION

Parameter	EM-U	Had-U	Had-Fe	Total
Thickness	30 X_0 1 λ_0	5 λ_0	3 λ_0	9 λ_0
No. of Plates	30	120	10	160 plates
Plate Thickness	3 mm	4 mm	50 mm	
Gap Thickness	5 mm	5 mm	5 mm	
Readout Groups	4 2+4+8+16 (X_0)	2 2.5+2.5 (λ_0)	1	7 readouts per tower
Overall Length	24 cm	108 cm	55 cm	187 cm

TABLE 7.2 TRANSVERSE SEGMENTATION
TOWER GEOMETRY AT z = 485 cm*

Ring	η	θ (deg)	r (cm)	Δη	Δr (cm) at z = 485 cm	No. of Segments	$(\Delta\ell)_\phi$
	3.00	5.70	48.4				
11				0.10	4.6 cm	40	7.0
	3.10	5.16	43.8				
10				0.15	6.1	40	6.4
	3.25	4.44	37.7				
9				0.15	5.3	40	5.5
	3.40	3.83	32.4				
8				0.15	4.5	40	4.7
	3.55	3.29	27.9				
7				0.15	3.9	40	4.1
	3.70	2.84	24.0				
6				0.15	3.4	40	3.5
	3.85	2.44	20.6				
5				0.20	3.7	40	2.9
	4.05	2.00	16.9				
4				0.20	3.1	20	4.8
	4.25	1.63	13.8				
3				0.25	3.1	20	3.8
	4.50	1.27	10.8				
2				0.30	2.8	20	3.0
	4.80	0.94	8.0				
1				0.35	2.4	20	1.9
	5.15	0.66	5.6				
						———	
					Total # of Towers	360	

*485 cm is 1.5 λ_0 into the end plug

FIGURE CAPTIONS - CHAPTER 7

7.1 Front view of end-plug calorimeter showing pad segmentation.

7.2 Elevation view of end-plug calorimeter.

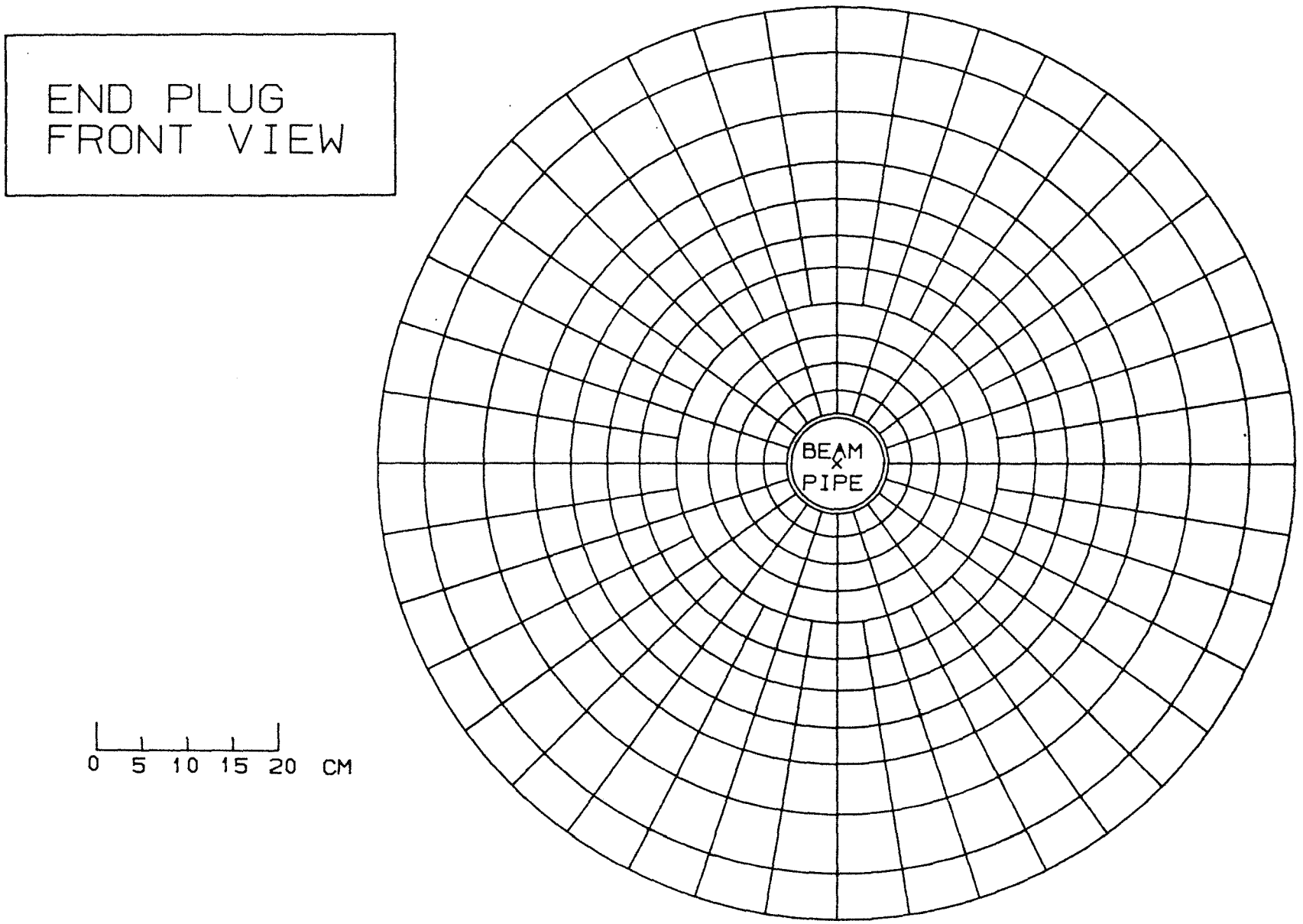

Fig. 7.1

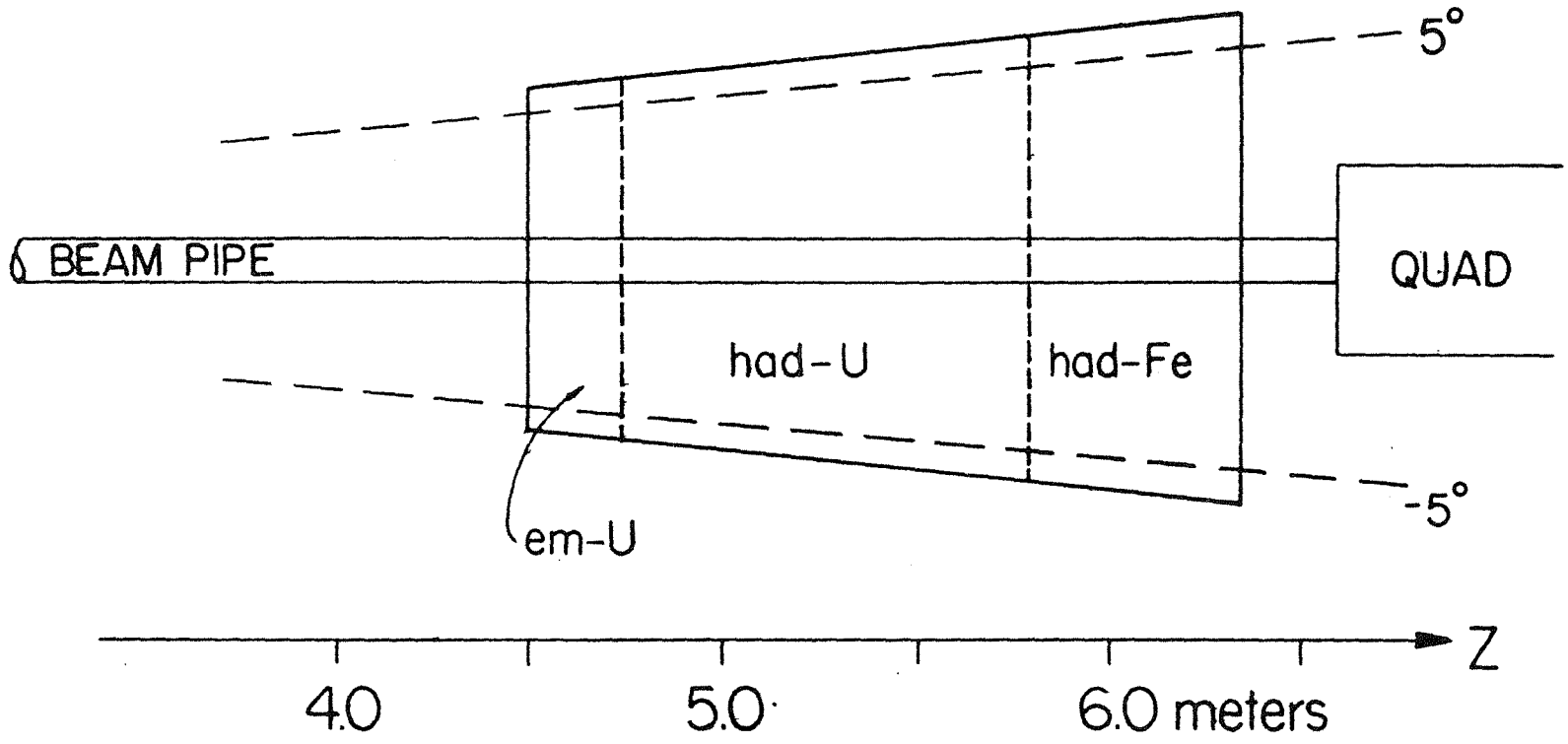

Fig. 7.2

8. ELECTRONICS FOR ULA

The requirements on the charge measuring electronics for the uranium liquid-argon are rather stringent; in this chapter we discuss our design criteria and the results of tests on the electronics built thus far. The general requirements include good control of equivalent amplifier noise, good reliability, compactness, and low-channel cost. Since the ULA signals represent the largest collection of signals in the experiment, and since the digitizers represent the largest single cost, we have chosen a scheme in which signals are multiplexed near the detector (after amplification) and again in the counting area prior to digitization. The multiplexing of dc levels at the detector can be made effectively noise free. The number of cables required for calorimetry which penetrate the radiation enclosure is reduced to a few thousand. It is also desirable to have fast analog pulse sums from regions of the detector for trigger purposes. The noise requirements for this purpose are less stringent.

8.1 DESIGN GOALS

Since the ULA calorimeter has its best resolution for EM energy we consider this case only. The longitudinal segmentation likewise places the heaviest burden on the first segment, 2 radiation lengths (X_0) in our case, where showers deposit a small fraction of their energy.

In the following we assume that 1 MeV of energy loss in liquid argon produces 20,000 electron charges and that 14% of the energy lost in the calorimeter is in the liquid argon. We choose as an example a 5 GeV electron shower. A 5 GeV shower deposits ~500 MeV in the first 2 X_0 on average, with a rms spread of ~100 MeV. Therefore $0.14 \times 500 = 70$ MeV are lost in argon

corresponding to 1.4×10^6 electron charges (e's) freed in the liquid. We would like to measure this average energy to 1%, which corresponds to 14,000 e's. Note also that if this is achieved one can measure muon, or other minimum ionizing particle, signals (~40,000 e's) to about 35%. It is desirable to do better.

8.2 FRONT END AMPLIFIERS

The standard way to measure small charges is by means of charge sensitive preamps. Since the output of a charge sensitive preamp returns to zero with a time constant of typically 100 to 1000 μs, it is necessary to shape the signal with appropriate filters. Alternatively one can sample the "base line" just before the signal, and then measure the signal. This method is particularly suited for colliders where the time of bunch crossing is well known. We intend therefore to follow the charge sensitive preamp by two analog storage stages, one measuring the base line and the second the signal, the first just before each bunch crossing and the second just after, as shown in Fig. 8.1.

In order to reduce the number of transmitted signals we generate the signal baseline difference in analog. This is possible because

i) The average baseline offset is ~0.1% of full scale.

ii) The two signals to be subtracted are stored and available for a long time if a trigger is present.

iii) By the use of standard J-FET op-amps and precision resistors, the difference can be obtained to an accuracy of 0.05% of the baseline level or, on average, to better than a few parts per million.

Since, in the presence of a trigger, the baseline corrected signals are available in dc, they can be time multiplexed for transmission to the counting room. Note that the baseline subtracted signals have a fixed maximum value since pile-up has been removed.

We intend to time multiplex 16 analog signals into one of 16 twisted pairs in a 34 conductor "twisted-flat" cable. Thus the ~50,000 signals can be transported on ~200 flat cables, which occupy a cross section of ~45×45 cm^2. Further multiplexing is also possible, up to about 64 signals per pair, without running into excessive readout time.

The preamps must be located as close as possible to the signal feed-throughs on the cryostat, while the baseline subtractor (BLS) can be 3 to 6 m away. We prefer to place the digitizers outside the radiation area because, while the previous circuit performs a single logic function (16 → 1 multiplex), the digitizers perform complex logic operations at card level, crate level, intercrate, and computer connection level. These operations are traditionally more prone to malfunction.

8.3 TEST RESULTS

With these goals in mind, we have built a charge sensitive amplifier (Fig. 8.2), the BLS (Fig. 8.3), and a high-gain amplifier to measure the equivalent input noise charge.

Since the noise of the charge sensitive preamp is typically a constant plus a term linear in the capacitance across the input, we

i) chose a high g_m FET (60,000 μMHO at 6 mA drain current) in order to minimize the capacitance effect.

ii) estimated the capacitance of a pad in the first EM compartment at ~200 pF (plus ~200 pF for connections) and therefore performed the test with 390 pF capacitor across the preamp input.

The noise signal measured in this way is shown in Fig. 8.4. We obtain an equivalent rms input noise of 2871 e's for this ideal situation, much better than the minimum requirements set forth previously. Allowing for degradation due to long connections, one should reasonably expect to reliably maintain a noise of ~5000 e's, which also means that the minimum ionizing particle signal is measured to an accuracy of 12.5%.

For the small pad areas of the ULA calorimeters, the radioactive noise contribution (mainly due to γ's) should be smaller than the electronic noise.[1]

A 5000e input charge corresponds to 140 μV preamp output signal and 0.25 MeV energy loss in argon. Thus 500 MeV in the first compartment (corresponding to 70 MeV in argon) give 39 mV at the preamp output. The preamp is well able to handle up to a 2-3 volt output, equivalent to 25-35 GeV total energy in the compartment, a rather unlikely occurrence. It is probably quite feasible to work at higher gain for the first compartment.

Each preamp signal is also available, after hard differentiation and an emitter follower, for trigger purposes (see Fig. 8.5). With the present preamp, again with 390 pF across the input, we obtain an equivalent signal of 60 mV per GeV of total deposited energy with an rms equivalent noise of 3.5 MeV. If one uses for a trigger the second and third section of the EM calorimeter plus the first and second section of the hadron calorimeter one could expect a noise of $\sqrt{(3.5^2+7^2+7^2+7^2)}$ = 13 MeV. Summing over the whole detector, assuming only random noise, gives σ_E(trigger) = 0.9 GeV, which for a total energy trigger is quite satisfactory. A threshold of 4.5 GeV, at 300,000 bunch crossings per second gives a random trigger of 0.08 Hz. For sets of 10 towers, appropriate for a cluster trigger, the noise in the trigger signal

could be ~40 MeV. Great care will be necessary in order to avoid external noise pick-up.

8.4 ADC AND RELATED HARDWARE

The end part of the electronics we intend to build consists of units (cards) which receive 16 twisted pairs carrying 16 time multiplexed signals each, or a total of 256 signals. In order to digitize these signals in a reasonable time, each card has 4 2-μs or 8 4-μs ADCs, giving a digitizing time of ~128 μs.

A crate of 16 cards can digest 4096 signals and 10 to 12 crates are enough for the whole detector. Each crate has a 20 MHz backplane for reading data from the ADC cards to a controller card which performs pedestal subtraction, empty channel suppression and gain normalization or scaling to energy. The last operation is done using a 24-bit multiplier which can run at 200 ns speed in pipeline fashion. Assuming an average occupancy of 10%, this allows 4096 words to be transferred to the buffer memory in 4096/10(0.2 μs) = 80 μs.

8.5 POWER DISSIPATION

We emphasize that dealing with ~40,000 channels of electronics one cannot forget the power dumped into the environment by the circuitry. For instance, the FET in the input stage is run at only 6 mA, which corresponds to ~60-90 mW, and depending on the supply voltage results in 2.4-3.6 kW of power dissipation. The preamp, which was perhaps too lavish, uses 195 mW at present but could probably be reduced to 100 mW for a total of 4 kW. The BLS and MPX use about 420 mW/channel or a total of 16.8 kW. Cooling and temperature control are a necessity.

REFERENCES CHAPTER 8

1. C. W. Fabjan et al., Nucl. Instrum. Methods **141**, 61 (1977) and V. Radeka, private communication.

FIGURE CAPTIONS - CHAPTER 8

8.1 (top) - Charge preamplifier signal.

(bottom) - Block diagram of the electronics.

8.2 Schematic of the charge sensitive preamplifier.

8.3 Schematic of the base-line-subtractor and multiplexer.

8.4 Measured noise signal from the preamplifier plus base-line-subtractor with 390 pF input capacitance.

8.5 Observed trigger signal for 80 MeV total energy input.

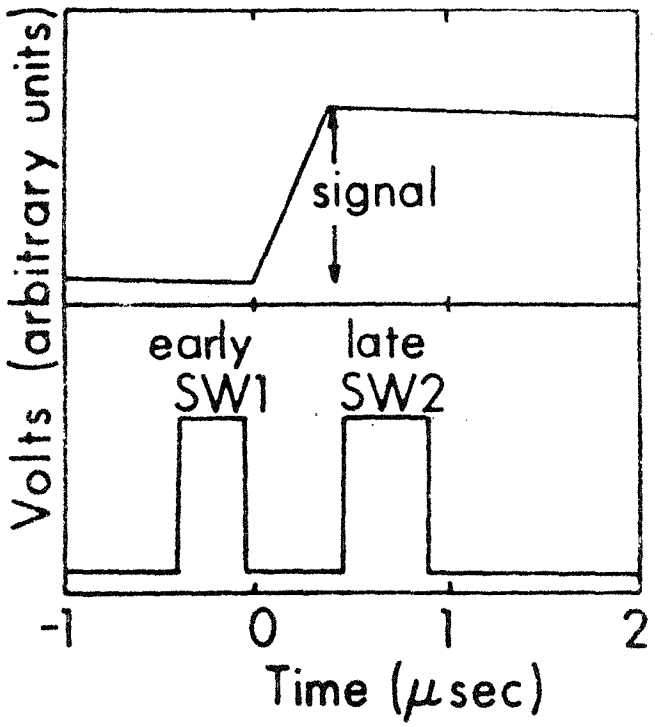
Volts (arbitrary units)
signal
early
SW1
late
SW2
-1
0
1
2
Time (μsec)

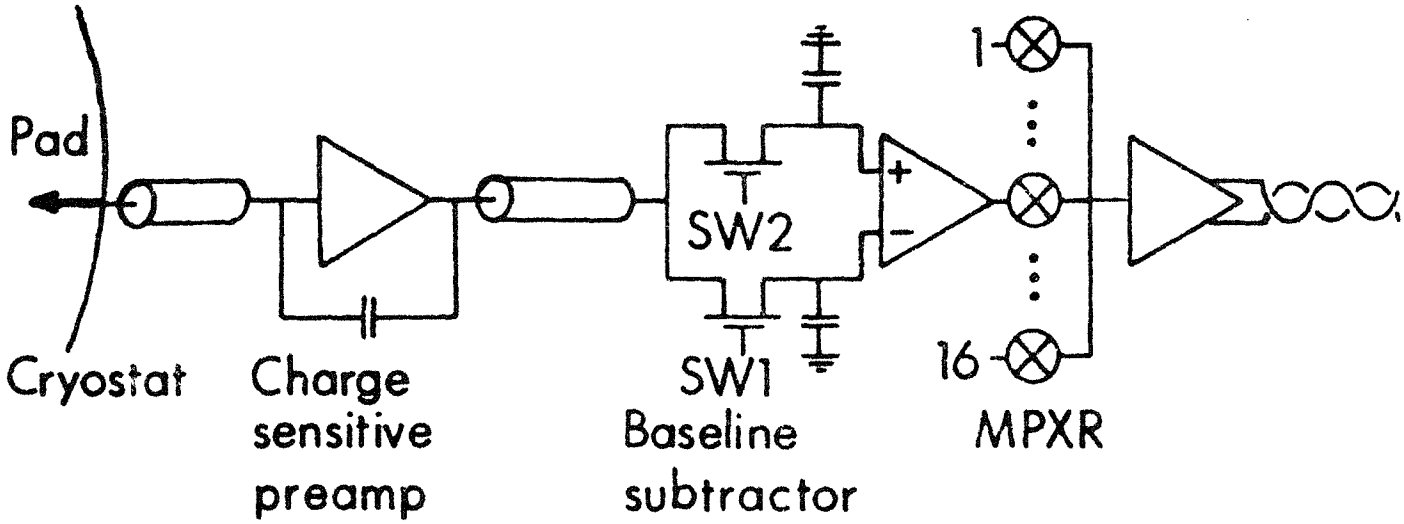
Pad
Cryostat
Charge
sensitive
preamp
SW2
SW1
Baseline
subtractor
1
16
MPXR

Fig. 8.1

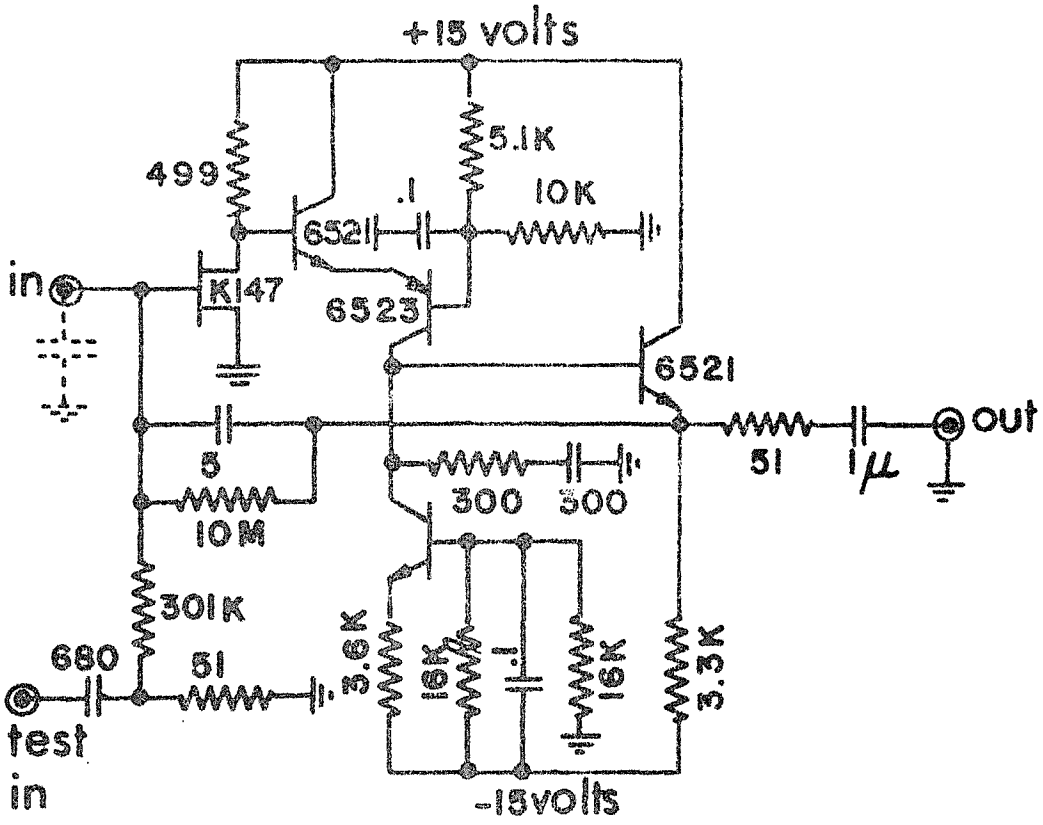
+15 volts
499
5.1K
.1
10K
6521
in
K147
6523
6521
out
51
1μ
5
10M
300
300
301K
680
51
3.6K
16K
16K
3.3K
test
in
-15volts

Fig. 8.2

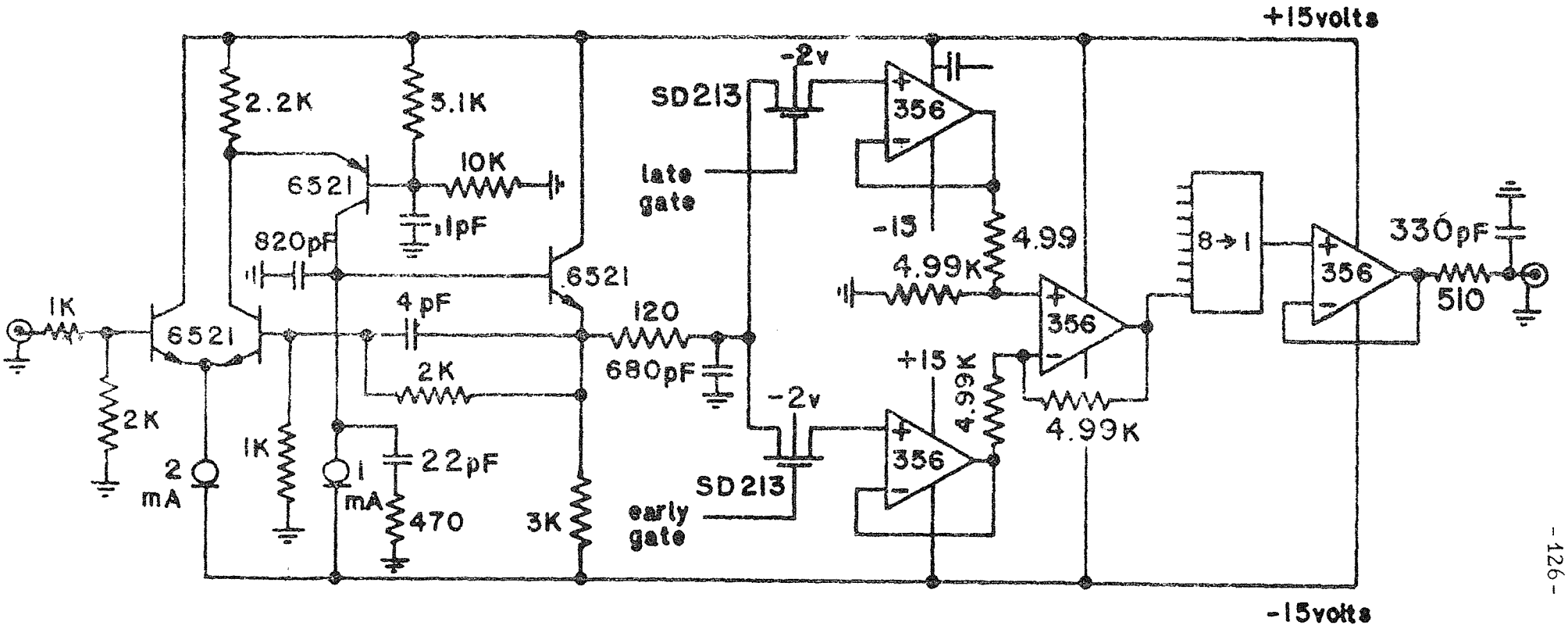
+15volts
-15volts
2.2K
3.1K
10K
6521
.1pF
820pF
6521
1K
6521
4 pF
120
680pF
2K
2K
1K
2
mA
1
mA
22pF
470
3K
SD213
late
gate
-2v
SD213
early
gate
-2v
356
-13
4.99
4.99K
356
+15
4.99K
4.99K
356
8→1
356
330pF
510

Fig. 8.3

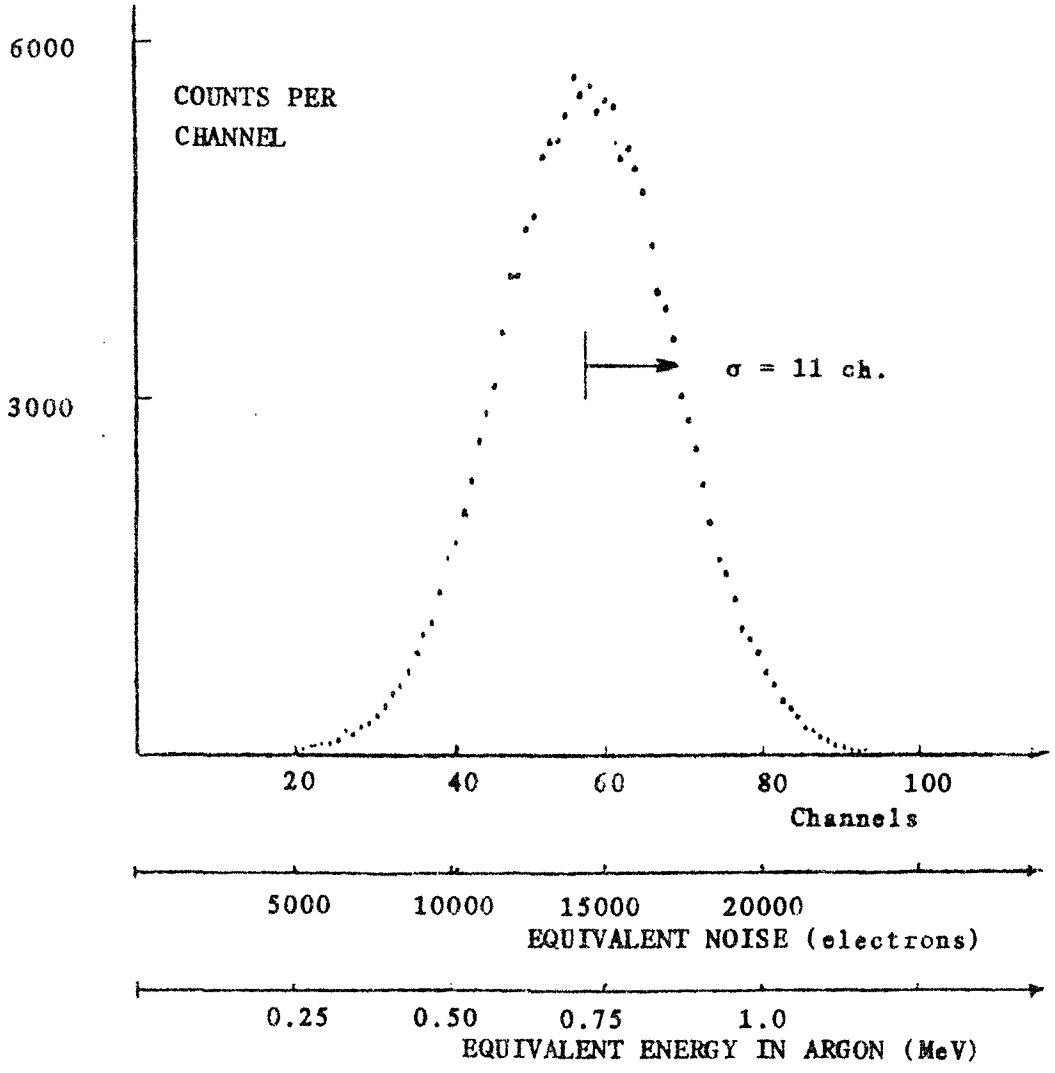
6000
COUNTS PER
CHANNEL
3000
σ = 11 ch.
20
40
60
80
100
Channels
5000
10000
15000
20000
EQUIVALENT NOISE (electrons)
0.25
0.50
0.75
1.0
EQUIVALENT ENERGY IN ARGON (MeV)

Fig. 8.4

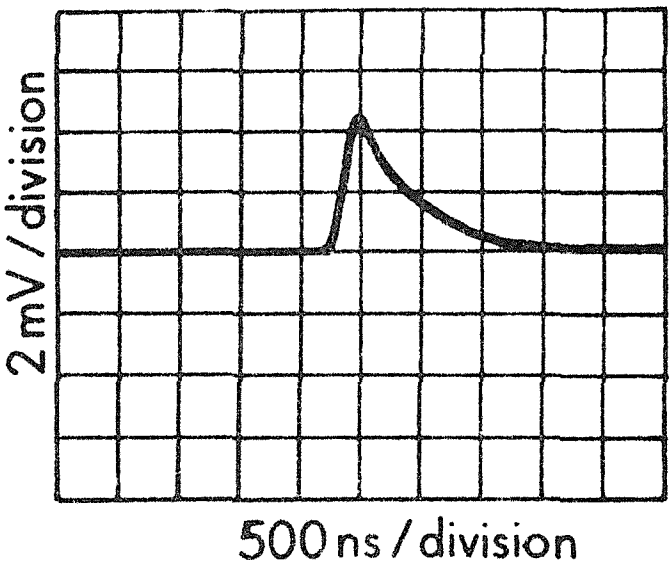

Fig. 8.5

9. THE MUON DETECTOR

9.1 INTRODUCTION

In Chapter 2 we presented the physics justification for measuring leptons--both electrons and muons--as well as possible. In this chapter we describe a muon detector optimized to accomplish these goals within reasonable financial and space limitations.

E740 will study leptons from fundamental hard scattering processes at and beyond the electroweak regime. This implies $p_T \gtrsim 50$ GeV/c for muons. Since angles down to ~8° are covered, this implies the need to separate muons from hadrons at momenta $p \gtrsim 360$ GeV/c.

At 90°, E740 has 7 λ_0 in calorimetry followed by 6 λ_0 in magnetized steel, for a total of 13 λ_0. This depth was deemed necessary to reduce interacting punchthrough to less than 1 emerging track per incident track. It was decided to scale the depth of material such that the punchthrough probability is independent of angle, and depends only on p_T. The punchthrough probability, throughout the detector, is then ≃ 1% at $p_T \simeq 15$ GeV/c and ≃ 10% at $p_T \simeq 40$ GeV/c.

An elevation view of one half of the detector is shown in Fig. 9.1. The detector is symmetric about 90° and the beam line. Drift tubes before and after the magnetized absorber provide the trigger as well as track information. Vertex tracking for off-line analysis comes from the central tracker described in Chapter 4.

There are three basic design criteria:

1. The iron must be thick enough to absorb showers effectively.
2. $\int$Bdl coupled with tracking granularity must provide momentum measurement errors smaller than multiple scattering up to 360 GeV/c. The transverse magnetic kick of the magnetized steel varies from about

0.6 GeV/c at 90° to about 0.9 GeV/c at 8°, the angular range of full muon coverage.

3. Occupancy in any muon tracking detector element must be low. Occupancy is defined as the probability of a hit in a detector element per inclusive inelastic event. In calculating the occupancy a rapidity density $1/\sigma\ d\sigma/d\eta = 3$ was used.[1]

The result from optimizing the design to meet these criteria is a detector with 1900 tons of steel magnetized to 20 kG instrumented by 29,000 drift tubes. Figure 9.2 shows the total absorber thickness and lever arm as a function of angle resulting from this optimization. The final design is 13 λ_0 deep at 90° and 18 λ_0 at 10°.

Three extra 1-in. gaps are left in the steel of all the muon detectors for instrumentation to be added later if needed. These gaps occur at 1λ, 4λ, and 5λ from the beginning of the steel.

Another possible option is to place small toroids with additional muon proportional drift tube planes outside of the plug calorimeter. These additions would extend muon momentum measurements into the 2° to 8° range and would require a small enlargement of the existing tunnel upstream and downstream of the present plan for a $40 \times 40 \times 64$ ft^3 collision hall. This option is not considered further in this report.

As the angle drops below 8° it becomes increasingly difficult to satisfy the scaling requirement imposed by punchthrough. In addition, the lever arm required to measure the angle of the exiting muon also increases. At some angle muon measurements are no longer attempted and the transition to the plug calorimeter (described in Chapter 7) is made. This angle was chosen to be 8°.

9.2 ELECTRICAL AND MECHANICAL DETAILS

9.2.1 Basic Geometry

As shown in Fig. 9.1 the muon detector is divided into a central portion, forward and backward intermediate portions, and forward and backward end caps.

Table 9.1 summarizes the basic parameters for each of these regions.

Table 9.1 E740 Iron and Coil Summary

	Central Cylinder	Intermediate Torus		End Cap Torus
Inner radius	3.0 m	2.7 m	from to	0.53 m 0.76 m
Outer radius	4.1 m	4.5 m		3.76 m
Length	3.0 m	1.6 m		1.6 m
Weight	560 t	330 t each		325 t each
Coil thickness (Cu coil)	5.0 cm	5.0 cm		5.0 cm
Coil current	1250 A	1250 A		1250 A
Total Coil Voltage (Volts)	20	15		20
Coil Power (kW)	100	80 each		100 each
Number of Coils	8	8		8
Conductor	$2.5\times2.5cm^2$	$2.5\times2.5cm^2$		$2.5\times2.5cm^2$
Total number of turns	240	192		192

9.2.2 Steel Design

All steel magnets will be assembled from flame cut, 8-in. thick grade 1020 low carbon steel. Magnetic properties of this steel were recently measured and summarized.[2]

The central steel "cylinder" is assembled as an 8-sided polygon from 8 "beams" of trapezoidal cross section. Each beam is 3m long. It comes with its own coil attached. The intermediate iron and the forward iron toroids are assembled from 8-in. plates weighing no more than 50 tons each. Figure 9.3, 9.4, and 9.5 show section views through the central, intermediate, and end-cap toroids.

9.2.3. Coils

In order to gain the maximum momentum resolution for a given weight, the steel will be excited to almost 20kG. This high excitation level requires the use of water-cooled coils. Low current density coils constructed from large dimension conductors have been built recently at Fermilab for E605. The engineering techniques needed to form and insulate the coils are understood.

The present design uses copper coils of 1 square inch cross section in a low power density design. There will be 32 coils of 24 turns each (7 m and 10 m circumference respectively) needed for the intermediate and end cap calorimeters and 8 coils of 30 turns (8 m circumference) needed for the central toroids. The total amount of copper will be 50 tons. The 1-inch copper can be wound by standard winding-table techniques and insulated with thermal-curing epoxy fiberglass tape. All coils proposed here are removable and can be prefabricated for quick installation during magnet assembly.

The actual power usage and excitation levels are operational decisions provided the water cooling capacity is adequate. As an example, a reduction

in current by a factor of 2 (using only 25% of the power) results in magnetization of 1 kG less than the one presented here; one should remember, however, the importance of adequate muon momentum measurement. With this design it may be possible to excite all toroids with only one 500 kW Transrex power supply.

9.2.4. Assembly of Toroids and Detector Support System

The toroids will be assembled in place on the detector transporter in the DO assembly hall. The completed toroids and transporter then form the skeleton on which the active detector elements are mounted. The arrangement and assembly of the 8-in. steel slabs will be optimized to minimize machining and welding.

The toroids and the detector will be assembled on a large 9-m wide by 11-m long transporter. This large I-beam weldment must hold the base of the toroids about 1.5 m above the floor. It must also distribute the 3000-ton load of the assembled detector onto the heavy-duty rollers that will enable the detector to roll in and out of DO. This platform will be assembled first, and then the toroids assembled on top of it. The design of the platform and the toroids will involve only pieces less than 50 tons. Thus a 50-ton assembly building crane will be the only large rigging equipment necessary for the assembly. Tolerances are important only at the mating machined surfaces crossed by lines of magnetic flux. Since the assembled toroids and transporter form the structure for all further detector assembly, it is important that this assembly procedure be straightforward and rapid.

9.2.5 Maintenance and Access

The central and intermediate toroids will be built with a clam-shell structure enabling them to separate horizontally into two halves. The end-cap toroids will slide parallel to the beams. This will allow the forward calorimeter to be moved away from the intersection point into the space vacated by the retracted end-cap toroid. Full access to the forward calorimeter and to the central tracker and central calorimeter will then be possible. The maintenance on the toroid and muon chamber system itself should be minimal. The muon chambers will clamp rigidly (and reproducibly) to the toroid transporter skeleton, thus allowing removal, repair, and alignment procedures to be simple and quick.

9.3 MUON PROPORTIONAL DRIFT TUBE SYSTEM

9.3.1 Muon Drift Tubes (PDT)

The instrumentation to register charged particles exiting the detector serves two functions. First, relatively crude but fast position correlations are needed to satisfy the first level trigger requirements. In particular, a rough p_T cut must be trivially derived from the bend angle in the iron. After the first level selection, coordinate digitization must provide precise locations and bend angles for further analysis. Since the first level trigger requires a decision between beam crossings, a drift chamber is limited to about 10 cm full cell size. In most locations this size is well matched to the first level "road" size requirements. On the end caps, near the axis, p_T resolution requires an even smaller full cell size, about 5 cm.

Many designs exist which provide accurate drifting over 10 cm dimensions. Drift chambers with simple box structure cells have been built[3] which gave excellent resolution (300 microns) and were self supporting in sizes up to 4 meters by 4 meters. The cell cross section used in Ref. 3 was 3 in. by 1.5 in. with a single central wire and no field shaping. Planes of perpendicular cells were bonded together to give rugged units with fixed relative alignment.

A similar type construction will be used for E-740 muon detectors. Figure 9.6 shows the muon chamber layout. There are 18 different sizes of chambers. Each unit shown has two planes in each direction to remove the left-right ambiguity. For most of the chambers, the cell size will be 10 cm by 5 cm. For chambers in the forward and backward directions, less than 20°, cell size will be 5 cm by 2.5 cm. Chambers 15-18 have wires only in the direction roughly parallel to the magnetic field. These chambers serve as redundancy and backup to those events where nearby delta rays or other spurious particles accompany the muon exiting the steel. Together with double hit electronics, these chambers will help identify spurious hits. All the rest of the chambers have wires in two dimensions.

The 18 chambers shown cover one octant (of one hemisphere) of the detector. The chambers at location 10 will have a thinner cross section than the others in order to fit between the steel. The octant units will overlap to eliminate edge dead spaces and to permit cross registration by tracks. These higher aspect ratio cells will have guide fields similar to the UA1 drift tubes[4,5]. In Table 9.2, the total wire count for all chambers of a given size is listed together with edge dimension, cell size, and pseudorapidity coverage. The total wire count is 29,434.

TABLE 9.2

Chamber	Wires	Dimensions (mxm)	Cell Width (cm)	Eta Range
1	776	2.8×2.1	10	0.51
2	800	2.8×2.3	10	0.45
3	1032	2.8×3.7	10	0.32
4	1208	2.8×4.8	10	0.23
5	1187	1.8×2.0	10	0.65-1.19
6	1248	1.8×2.2	10	0.59-1.09
7	1942	2.1×4.0	10	0.57-0.30
8	2236	3.1×3.9	10	0.38-1.09
9	2816	4.0×4.8	10	0.21-0.81
10	2511	2.5×2.5	10,5	2.66-1.04
11	1612	2.0×3.2	10	1.74-1.09
12	1830	1.3×1.6	5	2.66-1.74
13	2816	4.0×4.8	10	0.81-1.79
14	3724	2.6×3.2	5	2.66-1.64
15	432	2.8×4.2	10	0.26
16	1152	3.6×4.2	10	0.26-0.88
17	992	4.2×3.1	10	0.88-1.74
18	1120	1.8×2.3	5	1.74-2.66
Total	29,434			

The largest chambers proposed (4 m × 5 m aluminum) will expand 1.25 mm during a 10°C thermal excursion. Since the aluminum expands at twice the rate of steel, care must be taken in mounting the chambers to allow for differential expansion. A continuous alignment check, either with tracking or optics is necessary to maintain the advertised resolution.

9.3.2 Alignment of Chambers for the DO Detector

There are 6 steps in physically placing the wire tracking chambers into the DO collision hall, each resulting in some uncertainty as to the final position of a given wire. The steps and wire placement errors are as follows:

1. The wire is laid in the tracking chamber. This can be done by well-known techniques and its position relative to a pin on the outside of the chamber can be determined to within 50 microns.
2. Next the wire chambers or drift tubes must be placed into a framework which will later be mounted onto the detector itself. The accuracy with which this can be done is again 50 microns using similar techniques to those described in step 1.
3. The planes of PDT's are installed in the detector in the assembly hall before the detector is moved into the collision hall. Relative alignments of the wire chamber assemblies, as they are mounted onto the detector can be determined by standard optical techniques which yield relative position errors of ±100 microns. This alignment uncertainty can later be reduced to the order of 50 microns by looking at tracks with overlapping wires.
4. Some of the PDT's will not be physically attached to the detector in the assembly hall. They will be installed in the collision hall next to the walls before or after the detector is moved into place in the collision hall. The relative alignment of the wires in these PDT's is

the same as in steps 1 and 2 above. Alignment of the wires with respect to the collision hall is not important.

5. However, these PDT's must be aligned relative to the major portion of the detector once it has moved into place. This can be done most quickly through the use of a laser alignment system. Such a scheme involves the use of laser targets that consist of a number of photocells in an array. The targets are mounted accurately on the PDT's with respect to the wires. Targets are also accurately placed on the detector. Automatic Readout Micrometer Arms (ARM) can then be used with the targets to accurately determine offsets with respect to a laser beam. If the targets contain 4 photocells, accuracies of ±50 microns can be achieved.[6-9] This scheme has the advantage that it can be largely automated and therefore the time to align the detector, once it has been placed in the collision hall, can be greatly reduced.
6. Final alignment of the entire detector must be done once it has moved into the collision hall. This can best be done using the laser technique described briefly in step 5.

The overall position accuracy for any given wire at the conclusion of the alignment process is 200 microns if no tracking information is used. When tracking information is added, the relative positions of the wires can be determined to less than 100 microns. In later sections, a conservative estimate of 300μ is used in evaluating detector performance.

A requirement for maintaining alignment is that the collision hall temperature be constant to ±5° C. This requirement is imposed by the calorimeter electronics as well.

9.4. DETECTOR PERFORMANCE

9.4.1 Hadronic Punchthrough

Perusal of Fig. 9.7 graphically illustrates the need for many absorption lengths (λ_0) of material,[10] in this energy range. More quantitatively, Fig. 9.8 shows the number of particles in an hadronic shower as a function of depth for various energies.[11] Clearly, even at 90° for the electroweak scale, $p_T \simeq 50$ GeV/c, one needs at least 8 λ_0 of material just to "break even," i.e., one particle exiting per incident track. To explore a regime beyond the $W^{\pm}/Z^0$, one obviously needs even more material. It is worth mentioning that CDF[12] in B0 has only ~ 6 λ_0 at 90° where massive new phenomena would be kinematically favored to occur. By comparison, the UA1 experiment has found it necessary to go from 6 λ_0 depth to 9 λ_0 depth [13] in order to study muonic decays of the $W^{\pm}$ and the Z^0.

At 90°, our experiment will have 7 λ_0 in calorimetry followed by 6 λ_0 in magnetized steel, for a total of 13 λ_0. The curves shown in Fig. 9.8 can be parametrized, well past shower maximum, as $N(E, \lambda) \sim 5E\, e^{-\lambda/\lambda_{eff}}$ with $\lambda_{eff} = \lambda_0 E^{0.15}$. This implies the curve shown in Fig. 9.9. The depth for one particle in the cascade can be represented by $(\lambda/\lambda_0)_{N=1} \simeq 2.2\, \ell n(p_T/\sin\theta) - 0.76$. This expression was used to scale the depth of material. For our thickness, the punchthrough probability, at all angles, is then ≃ 1% at $p_T \simeq 15$ GeV/c and ≃ 10% at $p_T \simeq 40$ GeV/c.

To set the scale for the punchthrough problem one compares $\pi^{\pm}$ yields[14] to $\mu^{\pm}$ yields from $W^{\pm}$ decays in Fig. 9.10. As discussed above, punchthrough alone is not enormously supressed at 13 λ_0 depth, and buries the $W^{\pm}$ signal. In order to extract a clean signal at p_T values at and beyond the electroweak regime, one needs to track the particle which exits the magnetized iron. A muon will undergo multiple Coulomb scattering in the Uranium calorimeter and magnetized iron. In one dimension, it will scatter by $\Delta p_T^{MS}/p$, with Δp_T^{MS}

$= E_s \sqrt{L/L_{rad}}$ where $E_s \simeq 14$ MeV. For example at $p_T = 35$ GeV/c at 90°, the mean scatter will be 6.8 mrad. In contrast, a hadronic shower remnant will have a transverse momentum set by typical hadronic interactions, $\langle p_T^h \rangle \simeq 350$ MeV/c. An extremely crude estimate of the rejection factor due to only one angle cut is then,

$$\text{rejection} \simeq \frac{\Delta p_T^{MS}}{\langle p_T^h \rangle} \quad \frac{\langle n \rangle m_\pi}{\sqrt{s}},$$

where $\langle n \rangle$ is the mean multiplicity $\simeq 1.6$ ℓn s, $\sqrt{s} = \sqrt{2 m_p p_T}$ at 90° and the secondaries are all pions produced at rest in the c.m. This factor is $\simeq 0.019$ at $p_T = 35$ GeV/c.

This rejection power was better quantified by using data from a fine-grained calorimeter[10] (see Fig. 9.7). At 35 GeV/c the rejection factor is = 0.04 for a one dimensional rejection, based only on exit angle. The p_T dependence of this rejection factor is rather modest as indicated by the expression given above. A similar factor exists due to a cut on the exit position of the track. A Monte Carlo evaluation of this factor[15] for 2 independent exit coordinates is compatible with being equal to the angle factor squared. Finally, UA1[16] with 2 independent position and angle cuts, has a Monte Carlo result scaled to 13 λ_0 at $p_T = 35$ GeV/c which is a joint rejection factor = $(0.05)^4$.

In the case of our layout, there exist position and angle cuts on the exit track in the non-bending plane. In the bending plane the vertex and the 3 drift tube stations lead to one constraint. A conservative estimate is shown in Fig. 9.10, using a rejection factor from only 2 of the 3 cuts. Clearly the residual punchthrough background is well below the electroweak signal. Note that neither the third constraint rejection, nor rejection due

to tracking chambers in the steel or pads in the calorimetry have been applied. At p_T = 35 GeV/c the total rejection factor due to 13 λ_0 of absorption and the 2 cuts is $\simeq 1.4\times10^{-4}$. For comparison, non-interacting punchthrough is completely negligible: $e^{-13} = 2.3\times10^{-6}$.

9.4.2 Muons from Decay and Heavy Flavors

Decays from $\pi \to \mu\nu$ and $K \to \mu\nu$ are, in principle, a major source of background to prompt muons from sources due to electroweak bosons and heavy flavor decays. As discussed in Section 9.5, decays are the dominant background for a low-p_T trigger cut at $p_T \simeq 5$ GeV/c. In the electroweak regime of p_T, one uses a model of meson production[14] which is shown in Figure 9.11. The decay reduction factor for pions is roughly $Rm_\pi/p_T(c\tau)_\pi$ which favors a compact detector design. The E740 detector has r = 70 cm for tracking and transition radiation detection for electrons. At larger radii the dense uranium liquid-argon calorimeter provides a minimal decay distance. This yield of decay muons is shown in Fig. 9.11 and compared to the cross section for electroweak decays, $W^\pm \to \mu^\pm\nu$. Note that for $p_T > 5$ GeV/c, the dominant source of background muons comes from K-decays, not π-decays.

In Fig. 9.11, no reduction factor has been imposed for decay "kinks." To set the scale for cuts at p_μ = 30 GeV/c, a $\pi \to \mu\nu$ decay has a 1 mrad kink, and a $K \to \mu\nu$ decay has an 8 mrad kink. The central tracking resolves angles to $\simeq$ 10 mrad; hence, substantial reduction factors are available. For isolated muons from $W^\pm$ or Z^0, powerful topological cuts are available. The UA1 experience,[17] with a less compact geometry, is that $W^\pm$ and Z^0 can be easily extracted from this background. Note also that a yield which falls as e^{-bp_T}, when smeared by a Gaussian resolution with standard deviation σ, is increased by a factor $e^{(b\sigma)^2/2}$. As inspection of Fig. 9.11 shows, at $p_T \simeq$ 30

GeV/c the slope is $b \sim 8\ GeV^{-1}$. Given a resolution $dp/p = 0.18$ as discussed in Section 9.4.3, this implies a factor $e^{(b\sigma)^2/2} \simeq 1.4$ which is quite tolerable.

Another background is due to the production of jets containing heavy flavors which decay semileptonically. The yield for muons from this source, as evaluated by the ISAJET Monte Carlo,[18] is shown in Fig. 9.11. The yield is comparable to that for decays in the regime $p_T \simeq 30$ GeV/c. As with decay backgrounds, powerful topological cuts[17] exist which can be used to separate electroweak and heavy flavor muons.

9.4.3 Muon Momentum Resolution

The resolution on muon momentum is largely determined by multiple scattering. The depth of steel was chosen such that the punchthrough probability is a function of p_T only, independent of angle. Thus the steel depth varies roughly as $\ell n(p_T/\sin\theta)$ going from 101.6 cm at 90° to 142.2 cm at 10°. Given that one is dominated by multiple scattering, then $dp_T/p_T = dp/p$ varies as $1/\sqrt{L}$ where L is the depth of steel traversed. Hence, the resolution in p_T is only slightly dependent on angle; there is an 18% variation from 90° to 10°.

This being the case, it suffices to examine the muon momentum resolution at 90°. The torodial field is excited to 20 kG as discussed in section 9.2.3. Thus, the p_T bend is $\Delta p_T^B = 0.61$ GeV/c while the multiple scattering transverse kick is $\Delta p_T^{MS} = 0.106$ GeV/c. The ratio is $\Delta p_T^{MS}/\Delta p_T^B = 0.174$. Muons are measured in the central tracking chambers in 2 stations of drift tubes after the calorimetry (7 λ_0 deep, 1.5 GeV range cut, 230 X_0 deep), and after the magnetized steel (13 λ_0 deep, 2.7 GeV range cut, 288 X_0 deep) in 3 stations of drift tubes.

The drift tubes have 1.5 m lever arm in the central region, and 4.3 m lever arm in the forward region. Outgoing muon angles are determined to $d\theta \sim \sqrt{2}(dx/\ell) = 0.28$ mrad (central), 0.10 mrad (forward) where ℓ is the lever arm and dx is the positional accuracy (assumed = 300 μm, see Section 9.3.3). Since the multiple scattering error scales as $\sin\theta/p_T$ one would like to scale the lever arm as $(\sin\theta)^{-1}$ to have errors dependent only on p_T. This unfortunately leads to prohibitive space requirements.

The length ℓ was chosen in such a way as to have a trigger resolution roughly independent of angle and dependent only upon p_T. This length also defines the maximum measurable muon momentum. We require that muons at and beyond the electroweak regime be sign selected, so as to span the region of p_T with detectable hard scattering rates. At 90° the maximum p_T for which sign selection is possible, i.e., when multiple scattering equals measurement error, is roughly:

$$p_T^{MAX} \simeq E_s \sqrt{X_0^C + X_0^F}\, \ell/(\sqrt{2}\, dx)\, \sqrt{1 + (\ell/L_c)^2}$$

where

E_s = 14 MeV

X_0^C = depth of calorimetry in rad lengths

X_0^F = depth of steel in rad lengths

L_c = length of calorimetry.

At 90° the maximum is $(p_T^{MAX})_{90^0} \simeq 380$ GeV/c, while at 20°, $(p_T^{MAX})_{20^0} \simeq 280$ GeV/c.

For p_T below the measurement error limit one is dominated by multiple scattering. In this regime, 2 types of topologies can be identified. For muons in jets, the central track match will often be obscured, in which case one really has only a line at 13 λ_0 and a short line at 7 λ_0. In this situation $(dp_T/p_T)_{jet} = \pm 0.20$. For isolated muons, the central track is available, but smeared by the 230 X_0 in the calorimetry. In this situation, $(dp_T/p_T)_{isolated} = \pm 0.18$ which is essentially $\Delta p_T^{MS}/\Delta p_T^B$. These resolutions are based on hand calculations, confirmed by detailed Monte Carlo simulations and subsequent fits. Note that what is quoted here is the FWHM/2.36, whereas the resolution curves in fact have a Gaussian piece with additional long tails on the low momentum side.

Additional chambers may be inserted behind the calorimeter or within the steel, although a final decision has not yet been made. Chambers in the steel aid only a little in momentum resolution, but do aid substantially in punch-through rejection. Additional tracking chambers between the calorimeter and the steel improve the resolution slightly with respect to the values for dp/p already quoted above. This improvement clearly must be optimized against the implied increase in steel volume.

9.5 MUON LEVEL I TRIGGER

The muon trigger uses vertex z position determined to ±0.5 cm in the central tracker (Sections 4.3 and 10.2) and the struck cells in the outer muon chambers. The ability to trigger on muons depends on thick iron to control hadron punchthrough and an adequate lever arm in the muon chambers to measure bend angle quickly. The 10° - 20° region is difficult for the level 1 trigger for single muons but we will still be able to determine momentum and sign in this region.

The task of the muon trigger is to select muons out of a background from decays and punchthrough. This selection ideally should be only on the basis of the p_T of the muon, and not on the angle θ. First, let us attempt to calculate roughly the trigger rate in the central region, $-1 \lesssim y \lesssim 1$. A reasonable representation of ISR data for all charged particles in the trigger edge region, $1.5 \lesssim p_T \lesssim 4.5$ GeV/c, is $d^2\sigma^h/dydp_T^2|_{y=0} = ae^{-bp_T}$ with $a \simeq 180$ mb/GeV^2 and $b \simeq 4$ GeV^{-1}. This yield is shown in Fig. 9.12 over the region of interest.

Punchthrough at this p_T is quite small, as discussed in section 9.4.1. Pion decay has $(c\tau)B^{-1} = 780$ cm, ($B = \mu\nu$ branching ratio), while kaon decay has $(c\tau)B^{-1} = 590$ cm. At the p_T values appropriate to the trigger, the kaon and pion decays are roughly equal. For a decay length, $R_0 = 120$ cm $\simeq$ central tracking radius plus one λ_0 in the EM calorimetry has been assumed. The yield of decay muons is then,

$$\frac{d^2\sigma^h}{dydp_T^2} \simeq \left(1 - e^{-(R_0)m_\pi/p(c\tau)_\pi}\right).$$

This rate is shown in Fig. 9.10 also. Assuming a luminosity of $\mathcal{L} \simeq 10^{30}$cm^{-2} sec^{-1} and scaling of the cross section to $\sqrt{s} = 2$ TeV, the rate above the range cut, $p_T^R \sim 2.7$ GeV/c is then 0.30 Hz. This rate is comfortable even in the absence of cuts using the pattern of drift tube hits.

Naturally, this rate calculation is highly suspect. For verification, we have recourse to UA1 data.[13] This experiment finds a trigger rate at the same $\mathcal{L}$, scaled to the same decay path, of 80 Hz for a depth of 5.8 λ_0. This unacceptable rate was reduced by adding 60 cm of steel (total 9.4 λ_0). This addition reduces the punchthrough background by a factor of 0.05. Both decays and punchthrough (roughly comparable at 5.8 λ_0) are reduced by a factor of

0.17 due to the range cut being raised from 1.4 GeV to 2.0 GeV. This implies a rate of 6.8 Hz due to decay and 0.34 Hz due to punchthrough for a total of 7.1 Hz. Scaling again by 60 cm to the 13 λ_0 appropriate to E740, one extrapolates to 0.9 Hz decay and 0.002 Hz punchthrough. This result is at least in rough agreement with the 0.30 Hz calculation, and confirms that punchthrough is not serious at our depth of steel.

In the small angle region the situation is somewhat more difficult. In order to keep the range cut constant in p_T one would need to scale the steel thickness by $(\sin\theta)^{-1}$. In fact, the steel thickness scales like $\sim \ell n(p_T/\sin\theta)$ to keep punchthrough constant with p_T. This means that, for example, at $\theta = 20°$ the range cut is 3.55 GeV or $p_T^R = 1.21$ GeV/c. This leads to a rate of decay muons ~ 500 times larger in the forward region, $1 < y < 3$, and backward region, $-3 < y < -1$, than in the central region, $-1 < y < 1$, as can be seen in Fig. 9.12. This rate is unacceptable in that it would jam up the data acquisition stream.

To reduce the rate in the small angle region, the pattern of hits in the drift tubes outside the steel is used in the first level of trigger. A scaling of dr/ℓ by $(\sin\theta)^{-1}$ would make this trigger resolution dependent only on p_T and not θ, where dr is the drift tube hit resolution and ℓ is the lever arm between drift tubes. This scaling is approximately achieved by using 5 cm width for $8° < \theta < 20°$, 10 cm width for $20° < \theta < 60°$ (dr = 2.5 cm and 5 cm respectively), ℓ = 4.3 m for $8° \lesssim \theta \lesssim 20°$ and ℓ = 2.0 m for $20° \lesssim \theta \lesssim 60°$. Thus, the first level muon trigger resolution is largely independent of angle.

For example, consider $\theta \simeq 20°$. The muon exit angle is measured to $\simeq$ 12 mrad. The bending impulse is $\Delta p_T^B \simeq 0.85$ GeV/c. At a p_T of 2.5 GeV/c (i.e., the 90° range cut) the bend angle of 117 mrad projected to the vertex implies a displacement r^B = 58 cm. Measurement error in the drift tube is 2.5

cm with an added 6 cm due to exit angle error extrapolated to the vertex. Multiple scattering in the calorimetry and steel contributes 7.9 cm and 7.2 cm respectively. Folding in quadrature, the error is $\delta r = 12.5$ cm, or $\delta r/r^B = 0.21$. The shape of $\delta r/r^B$ as a function of p_T is shown in Fig. 9.13a. To the extent that multiple scattering dominates, $\delta r/r^B$ is independent of p_T.

The first level trigger envisions a "cut" at $p_T = 5.0$ GeV/c, which means a cut on r^B appropriate to $p_T = 5$ GeV/c, $r_B = 29$ cm + $2\delta r = 46$ cm. This cut is then $\simeq$ 98% efficient at $p_T = 5$ GeV/c and 50% efficient at $p_T \simeq 3.1$ GeV/c. This efficiency is shown in Fig. 9.13b. The result of folding $\varepsilon(p_T)$ into the decay muon yield is shown in Fig. 9.10. Clearly the small angle regions will have level 1 rates reduced from 500 times the central region rate to $\sim$ 5 times that rate. Using the UA1 data on rates this means $\sim$ 5 Hz, 1 Hz, and 5 Hz level 1 muon trigger rates for $p_T = 5$ GeV/c "cuts" in the forward, central, and backward regions respectively.

REFERENCES CHAPTER 9

1. R. B. Meinke, A. I. P. Conference Proceedings, No. 85, p. 347 (1981).
2. A. Ito et al., "B vs. H Curves for 1008 and 1020 Steels," TM-1197, July 1983.
3. S. Aronson, private communication, BNL E734.
4. K. Eggert et al., Nucl. Instrum. Methods **176**, 217-222 (1980).
5. L. E. Price, Long Drift Techniques for Calorimeters, ANL-HEP-CP-82-07.
6. T. Lauritzen and R. C. Sah, "The PEP Laser Surveying System," PEP-293 (1979).
7. J. Gunn et al., "A Precision Surveying System for PEP," PEP-2334 (1977).
8. J. Gunn and R. Sah, "Status Report: Plans for PEP Survey and Alignment," PEP-211 (1975).
9. R. Sah, "Automatic Surveying Techniques," PEP-210 (1976).
10. E594 Collaboration, private communication.
11. S. Iwata, DPNU-3-79.
12. CDF Design Report, 1981.
13. CERN/SPSC/82-51.
14. I. Hinchcliffe and R. Kelly, CDF-83.
15. A. Grant, Nucl. Instrum. Methods **131**, 167 (1973).
16. CERN/SPSC/78-19.
17. UA1 CERN-Preprint 83-39.
18. F. E. Paige, BNL 30805

FIGURE CAPTIONS - CHAPTER 9

9.1 Elevation view of one half of the detector.

9.2 (a) Total detector thickness as a function of angle.

(b) Lever arm as a function of angle.

9.3 Section AA through central cylinder.

9.4 Section BB through intermediate torus.

9.5 Section CC through end cap torus.

9.6 Conceptual PDT configuration.

9.7 Typical event in Fermilab E594 with 100 GeV π^- incident.

9.8 Number of particles in a hadronic shower as a function of depth.

9.9 Depth for one remaining particle in the hadronic cascade.

9.10 Comparison of $\pi^{\pm}$ yields and $\mu^{\pm}$ from W decay, punchthrough.

9.11 $\mu^{\pm}$ yields from decays and heavy flavors.

9.12 $\mu^{\pm}$ yields at the level 1 trigger.

9.13 (a) Fractional error in impact parameter for the level 1 trigger, $\delta r/r^B$, as a function of p_T.

(b) Trigger efficiency, $\varepsilon(p_T)$, as a function of p_T.

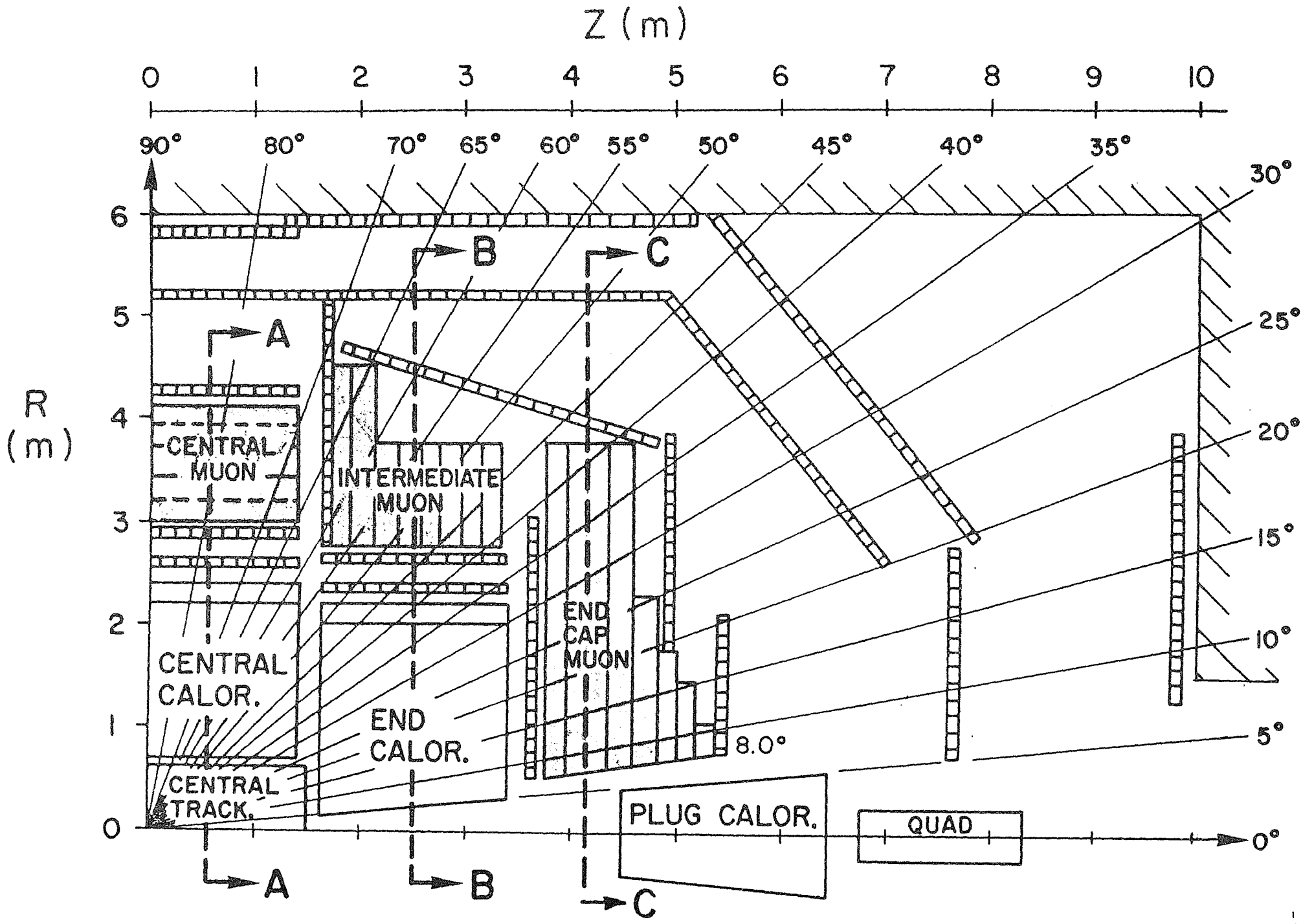
Z (m)
0
1
2
3
4
5
6
7
8
9
10
90°
80°
70°
65°
60°
55°
50°
45°
40°
35°
30°
25°
20°
15°
10°
5°
0°
R (m)
6
5
4
3
2
1
0
A
B
C
CENTRAL MUON
INTERMEDIATE MUON
END CAP MUON
CENTRAL CALOR.
END CALOR.
CENTRAL TRACK.
8.0°
PLUG CALOR.
QUAD

Fig. 9.1

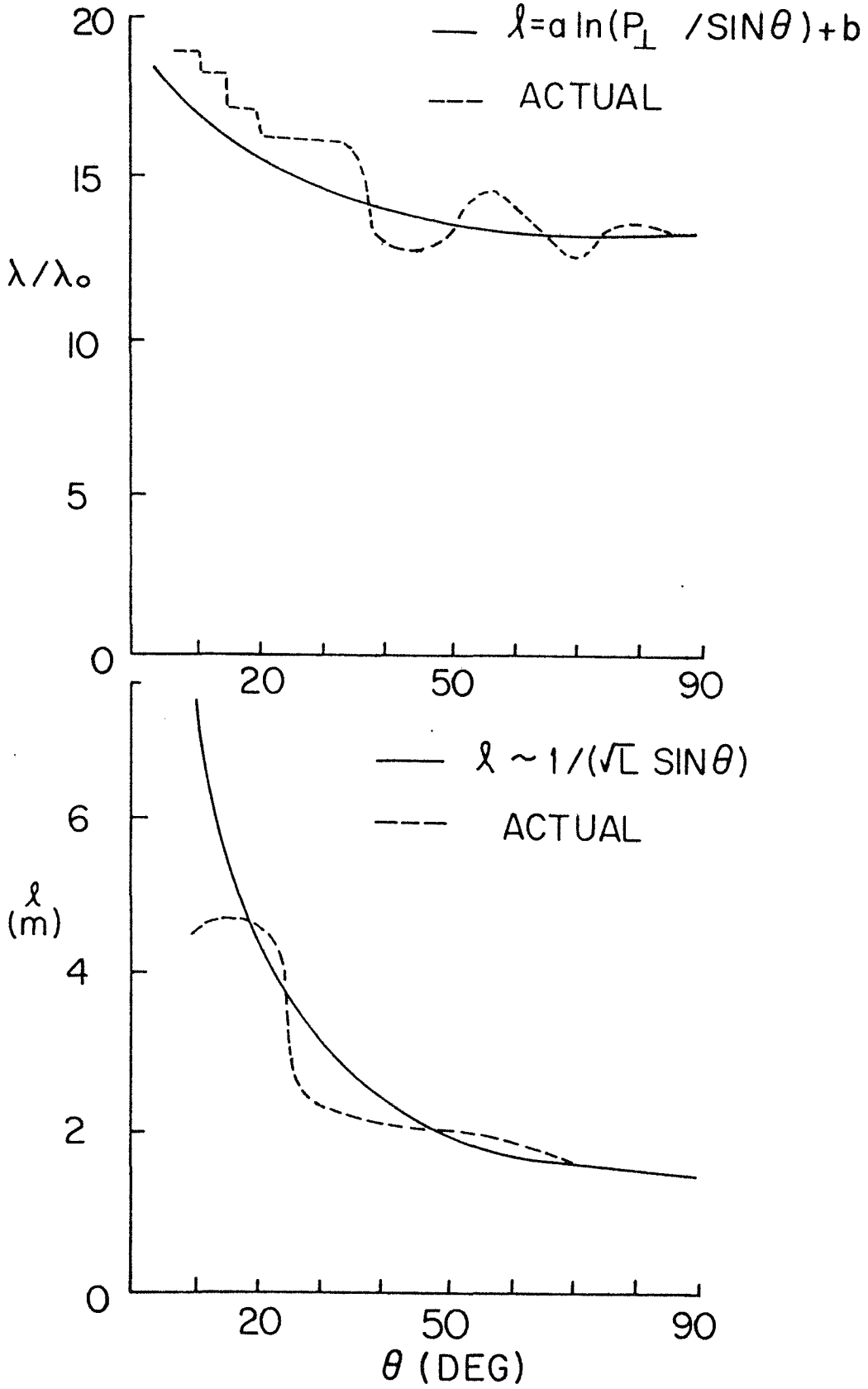
20
15
λ/λ₀
10
5
0
20
50
90
— ℓ=a ln(P⊥ /SINθ)+b
--- ACTUAL
6
ℓ (m)
4
2
0
20
50
90
θ (DEG)
— ℓ ~ 1/(√L SINθ)
--- ACTUAL

Fig. 9.2

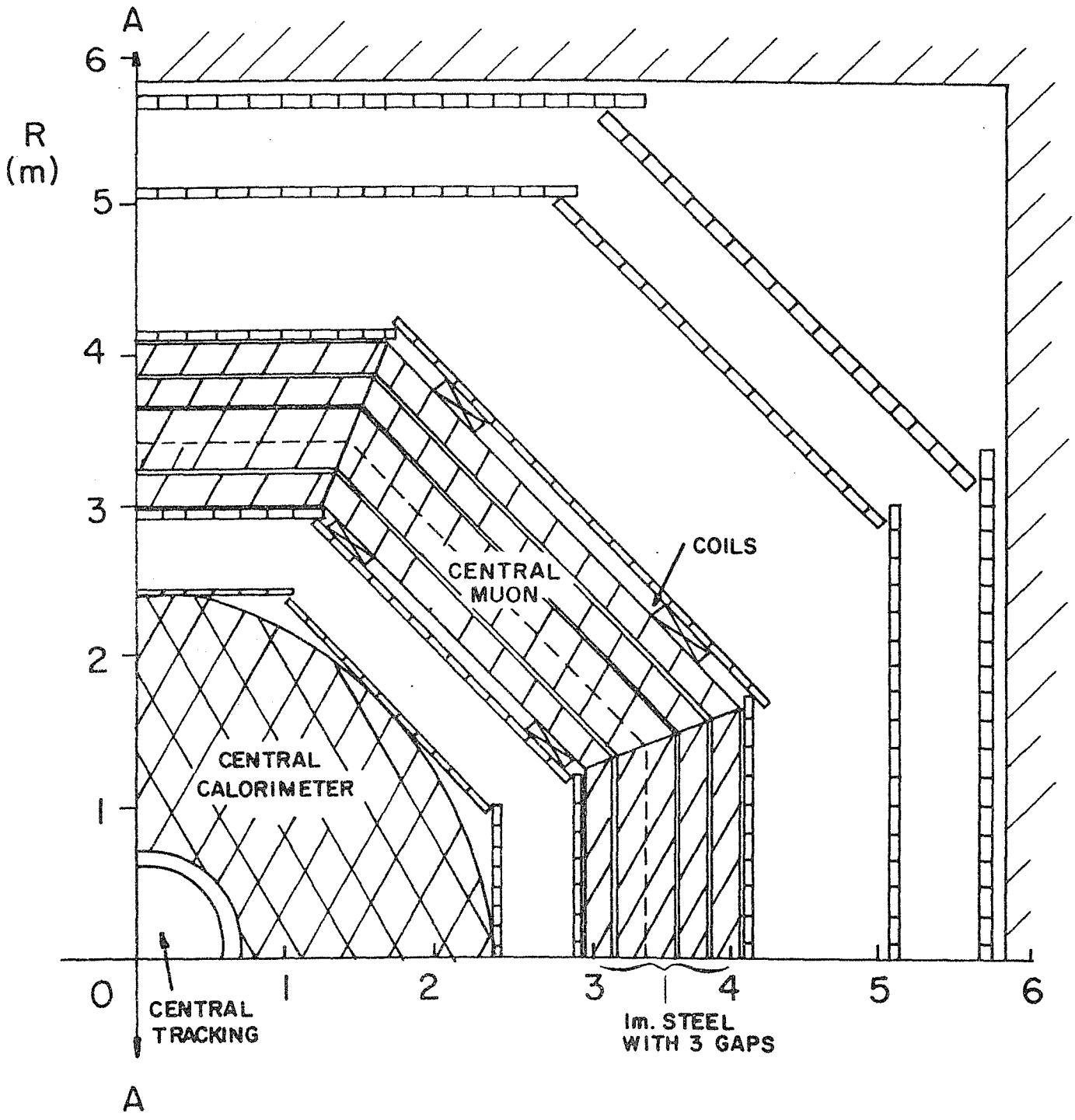
A
6
R
(m)
5
4
3
2
1
0
1
2
3
4
5
6
COILS
CENTRAL
MUON
CENTRAL
CALORIMETER
CENTRAL
TRACKING
Im. STEEL
WITH 3 GAPS
A

Fig. 9.3

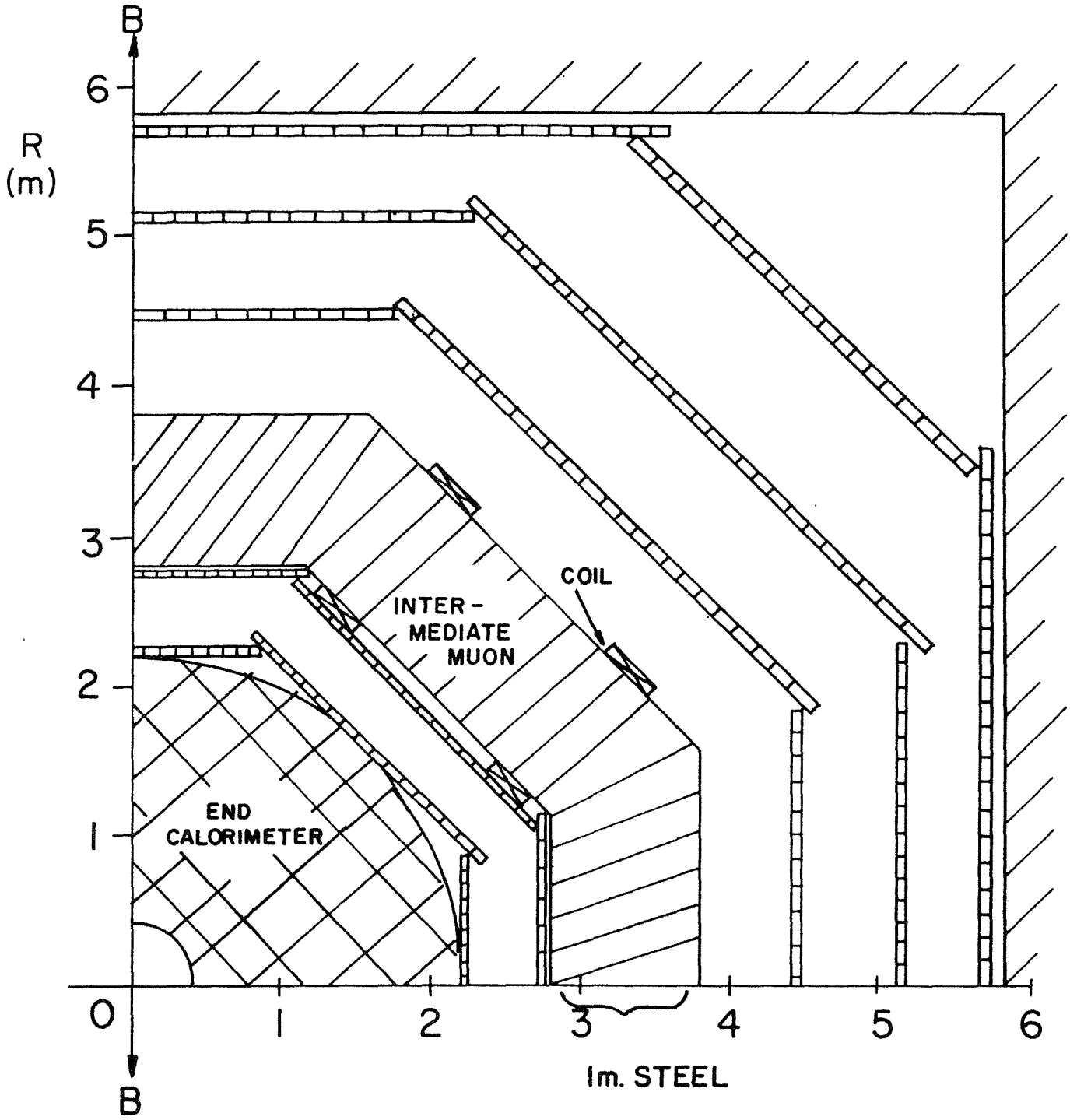
B
6
R
(m)
5
4
3
2
1
0
1
2
3
4
5
6
B
Im. STEEL
COIL
INTER-
MEDIATE
MUON
END
CALORIMETER

Fig. 9.4

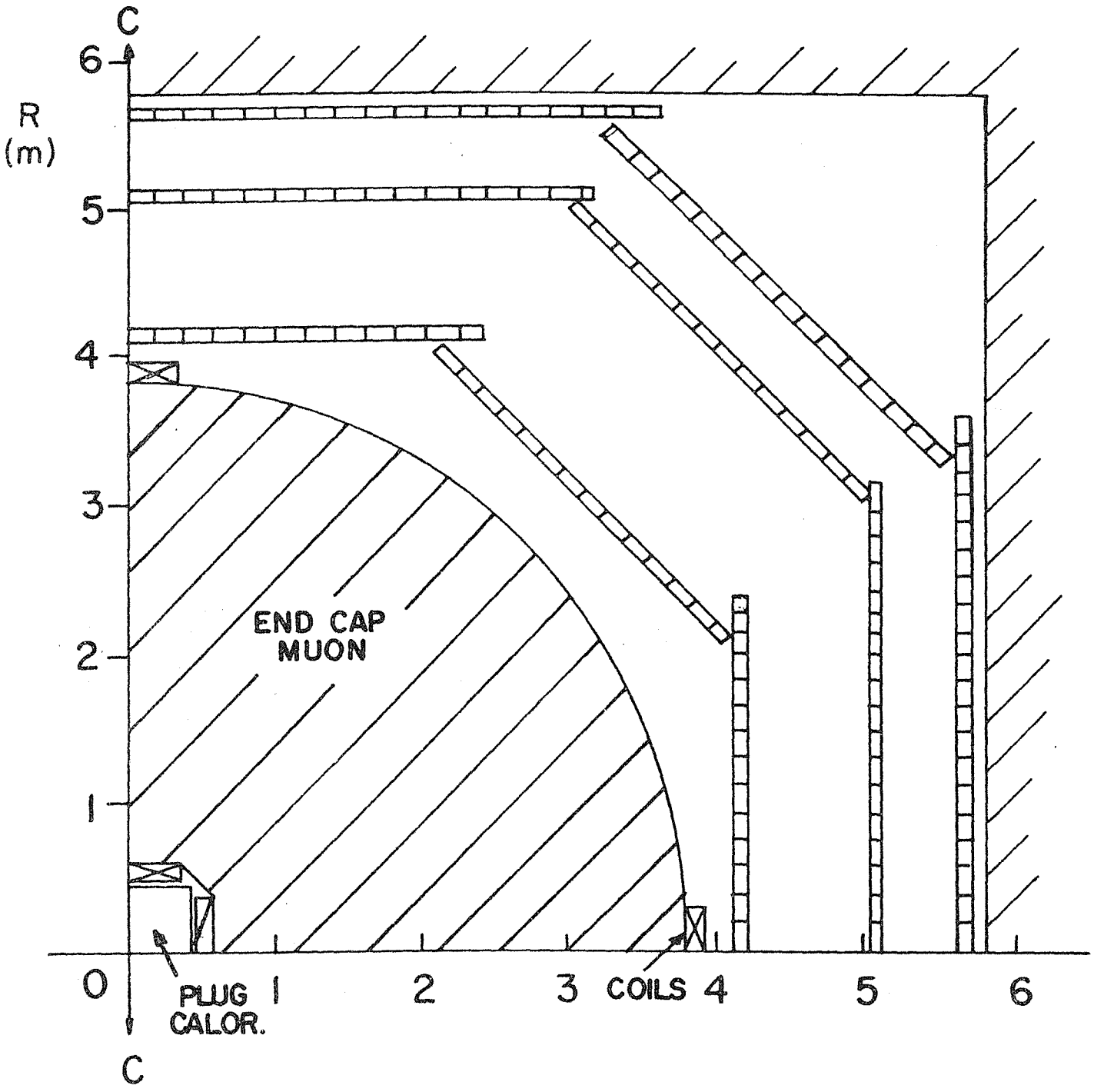

Fig. 9.5

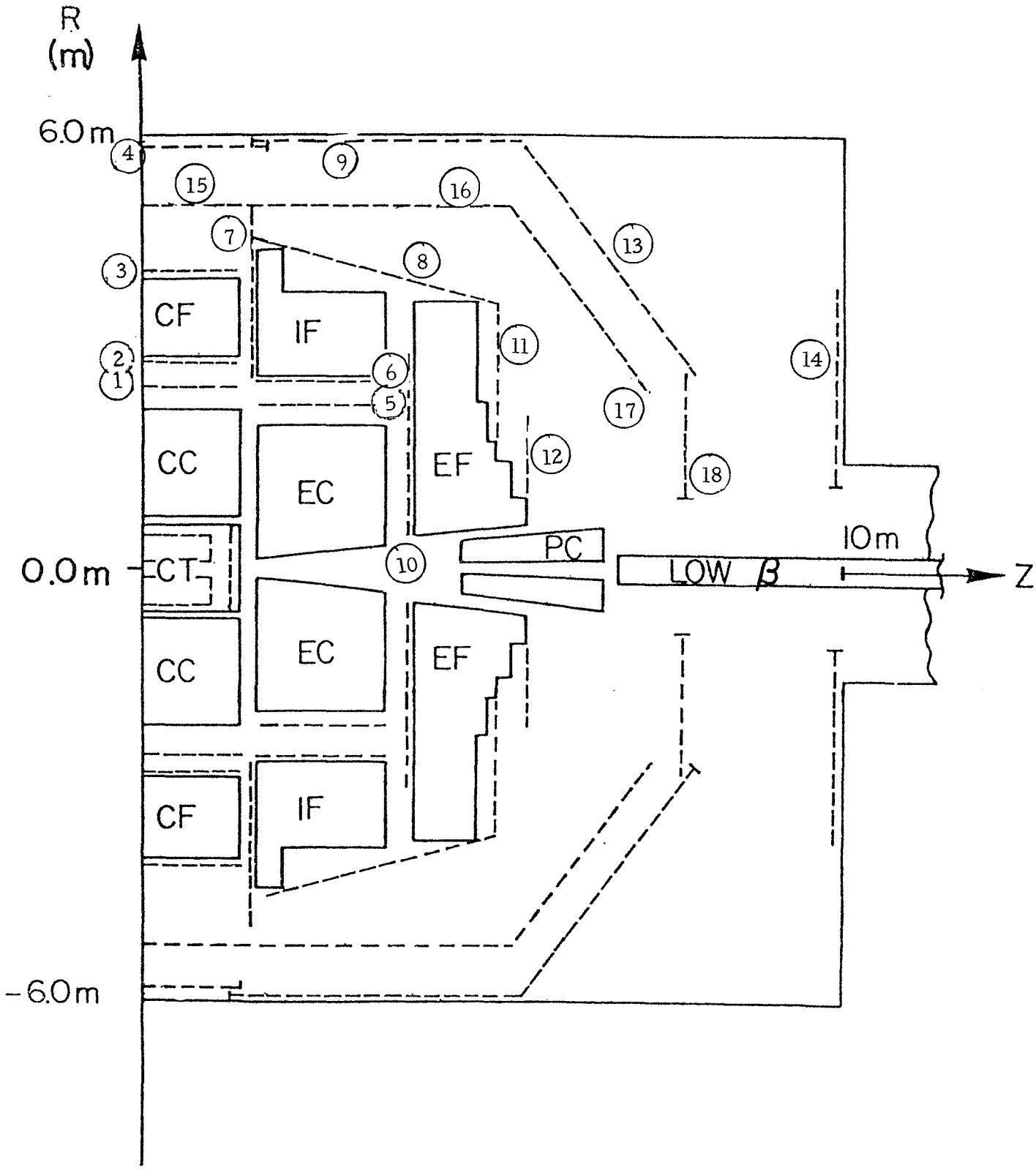

E 740 LAYOUT

Fig. 9.6

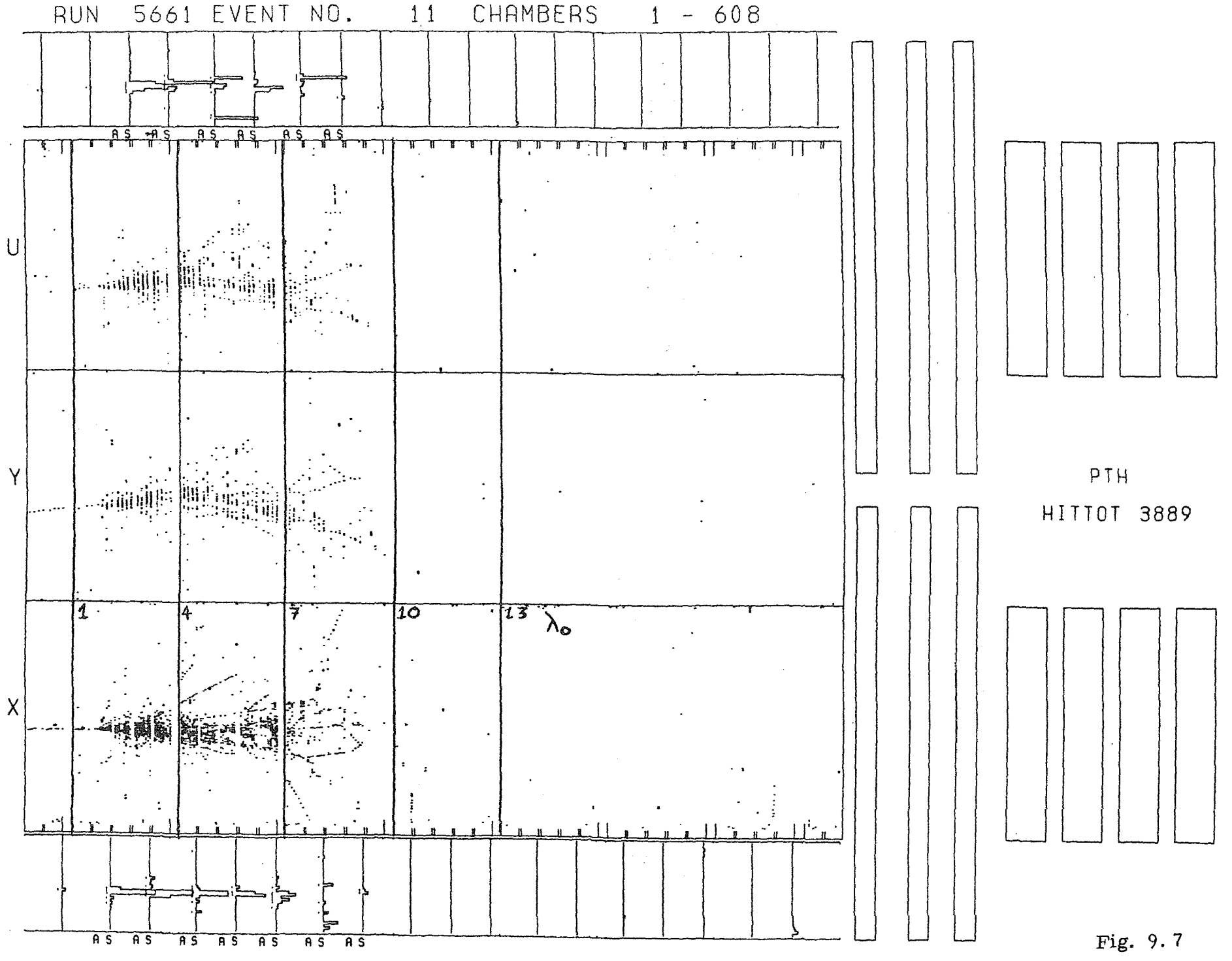
RUN 5661 EVENT NO. 11 CHAMBERS 1 - 608
AS AS AS AS AS AS
U
Y
X
1
4
7
10
13
λ_o
AS AS AS AS AS AS AS
PTH
HITTOT 3889

Fig. 9.7

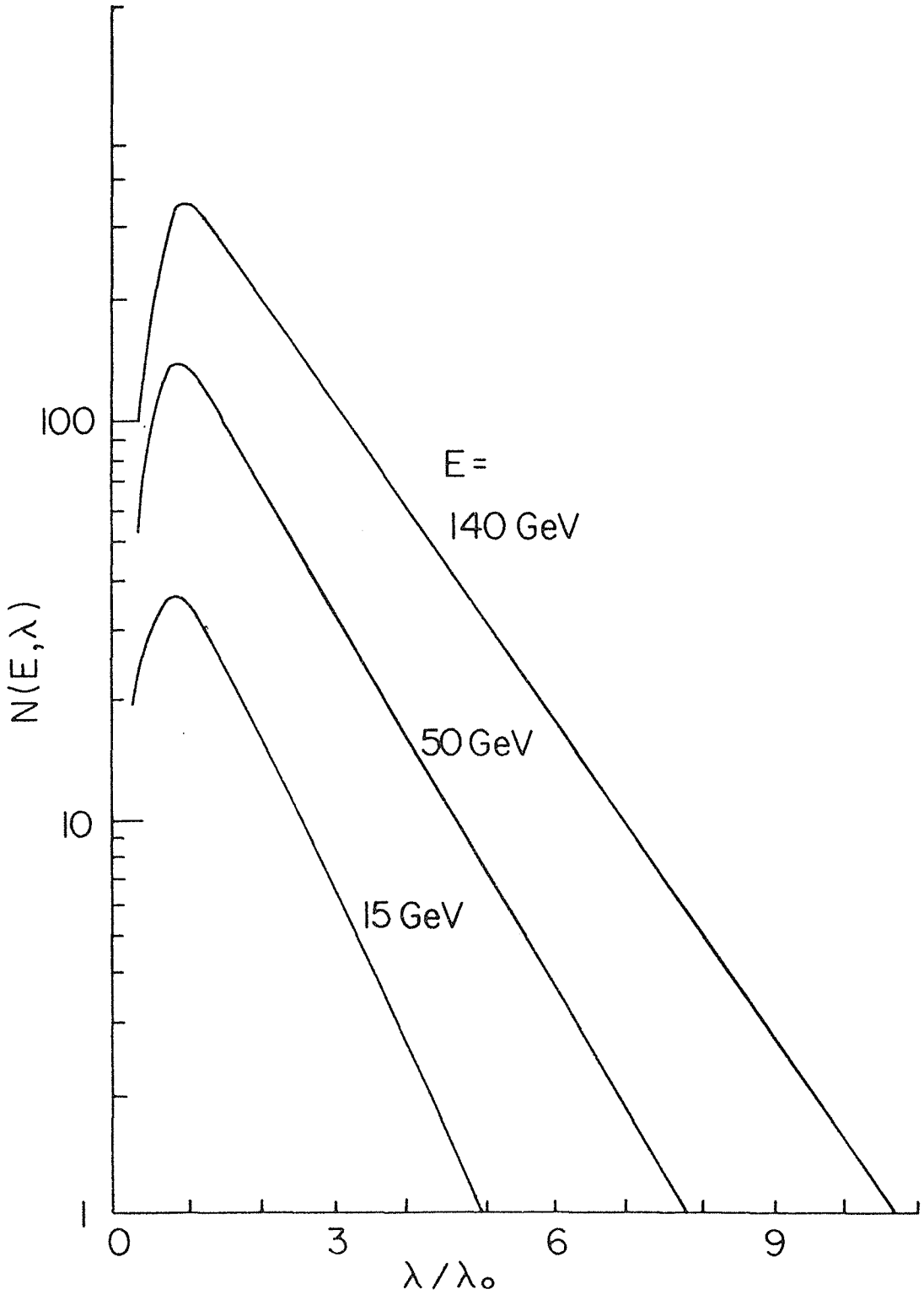

Fig. 9.8

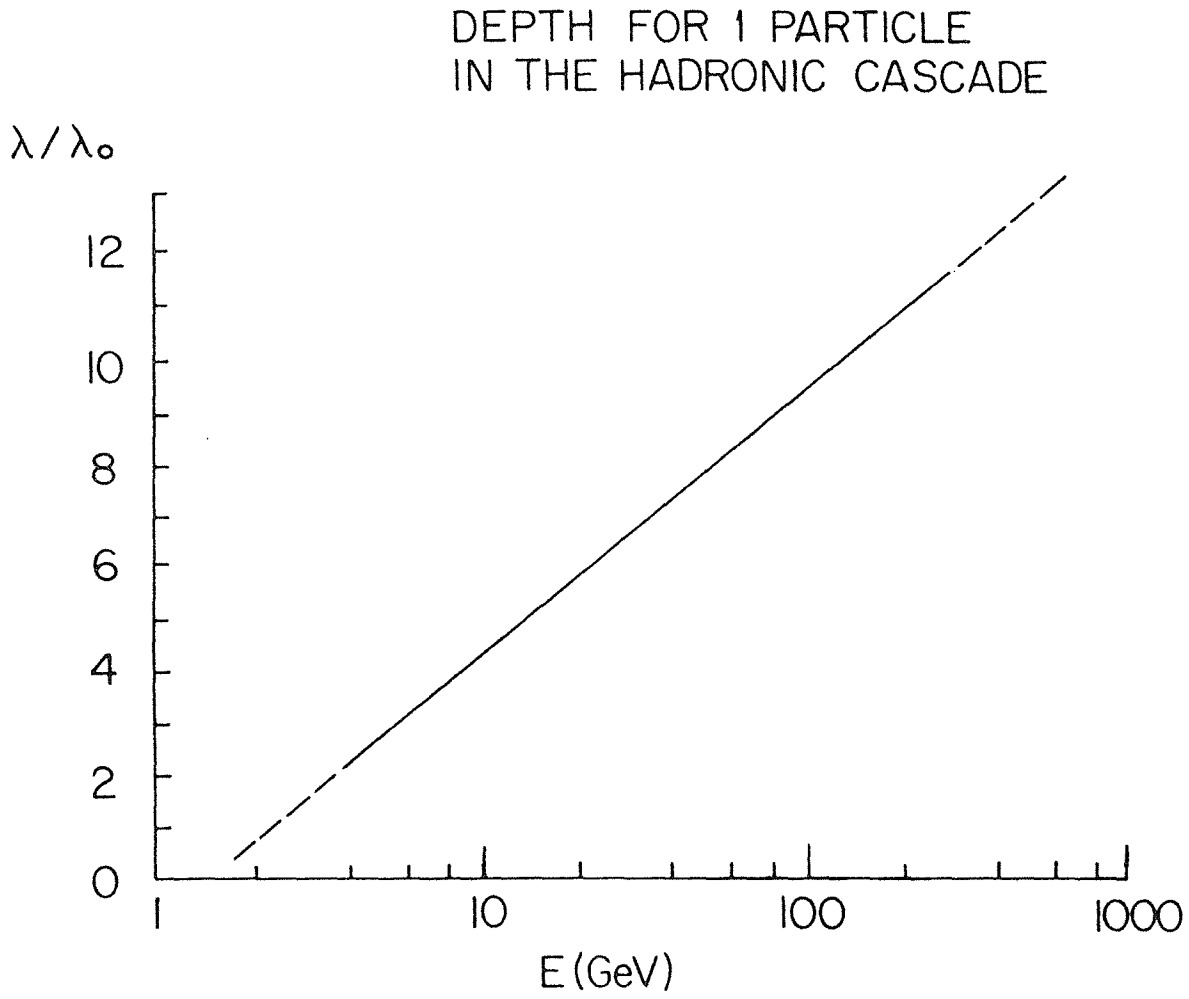
DEPTH FOR 1 PARTICLE
IN THE HADRONIC CASCADE
λ/λ₀
12
10
8
6
4
2
0
1
10
100
1000
E(GeV)

Fig. 9.9

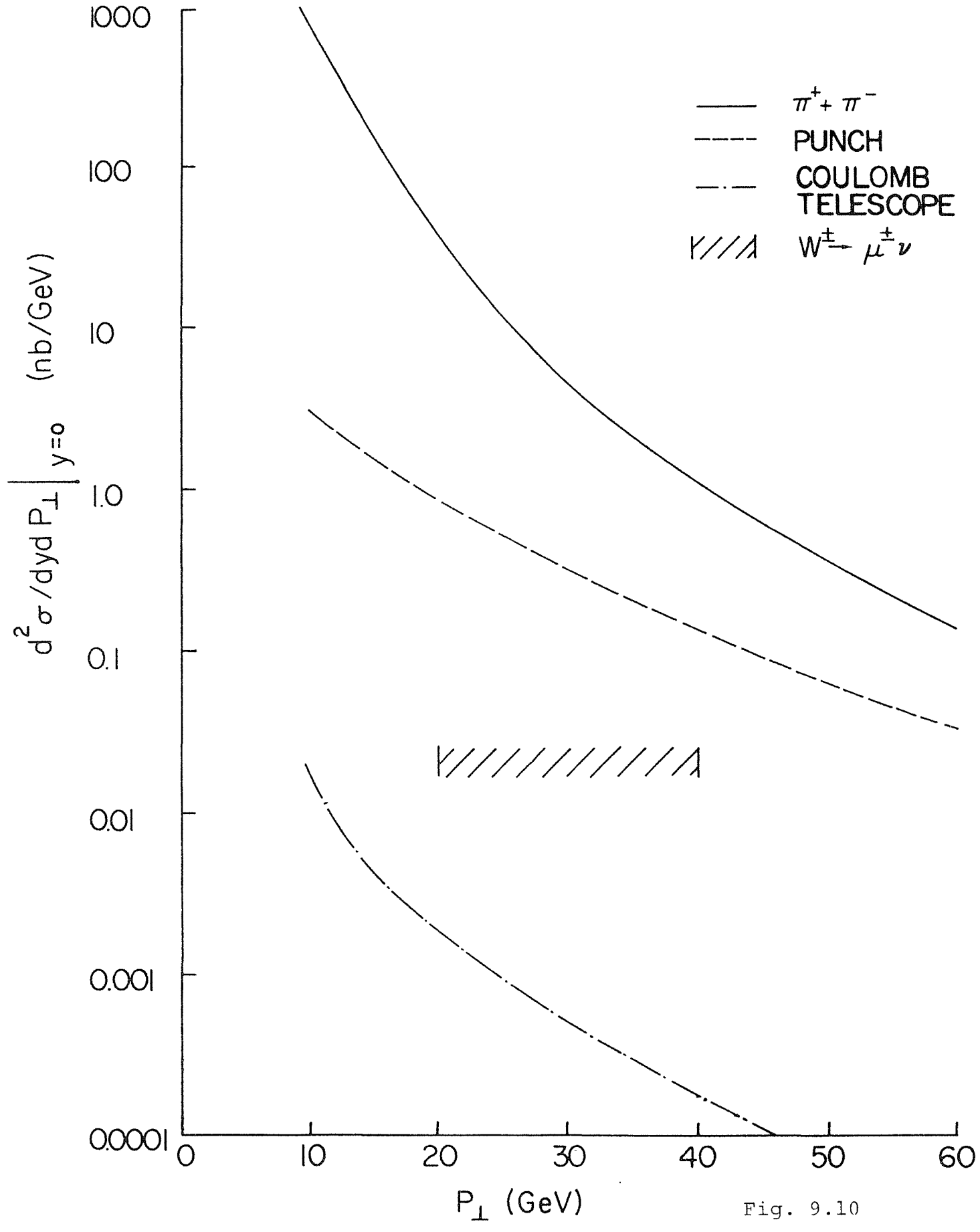
1000
100
10
1.0
0.1
0.01
0.001
0.0001
$d^2\sigma/dy\,d\,P_\perp\Big|_{y=0}$ (nb/GeV)
0
10
20
30
40
50
60
$P_\perp$ (GeV)
$\pi^+ + \pi^-$
PUNCH
COULOMB
TELESCOPE
$W^\pm \to \mu^\pm \nu$

Fig. 9.10

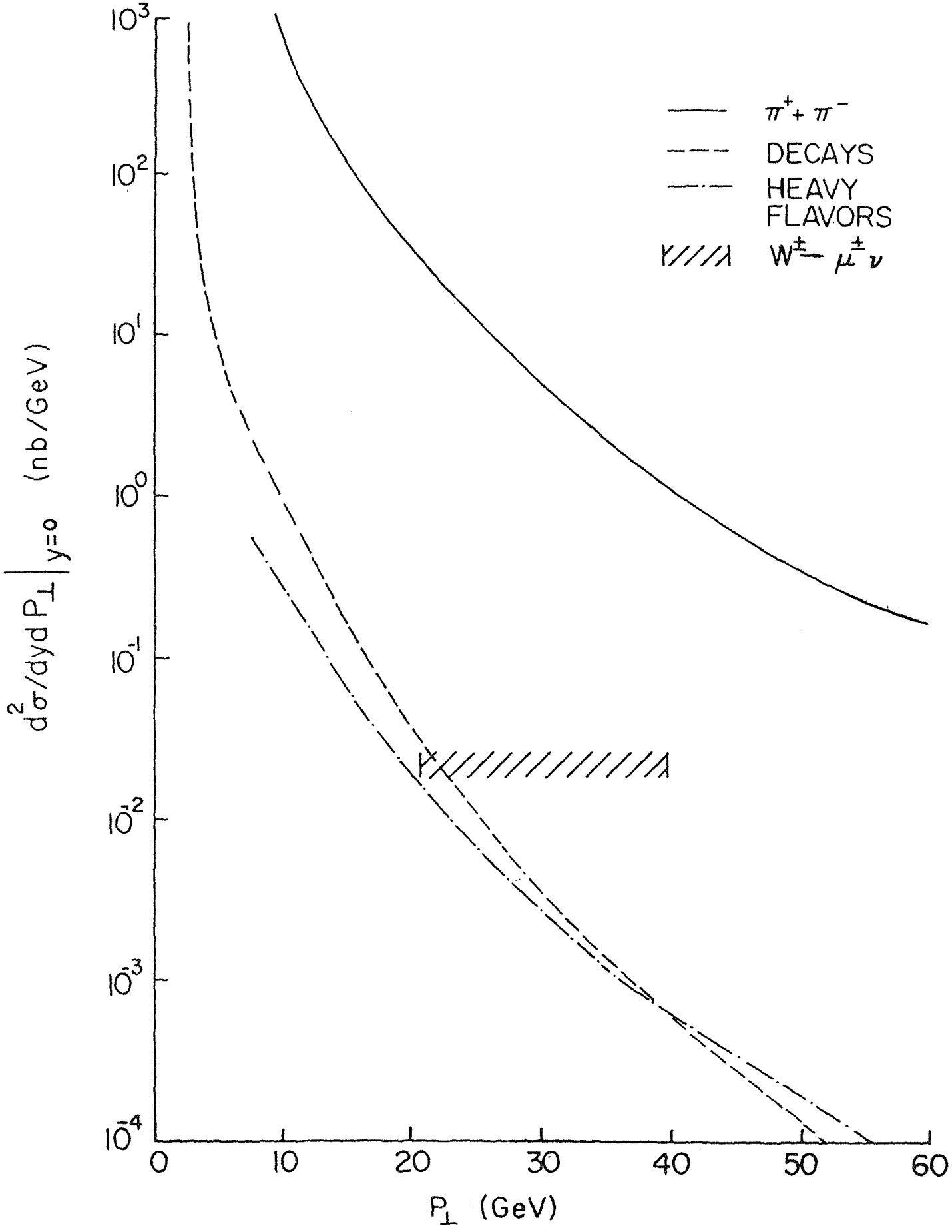
$\pi^+ + \pi^-$
DECAYS
HEAVY FLAVORS
$W^\pm \to \mu^\pm \nu$
$d^2\sigma/dy\,dP_\perp\big|_{y=0}$ (nb/GeV)
10^3
10^2
10^1
10^0
10^{-1}
10^{-2}
10^{-3}
10^{-4}
0
10
20
30
40
50
60
$P_\perp$ (GeV)

Fig. 9.11

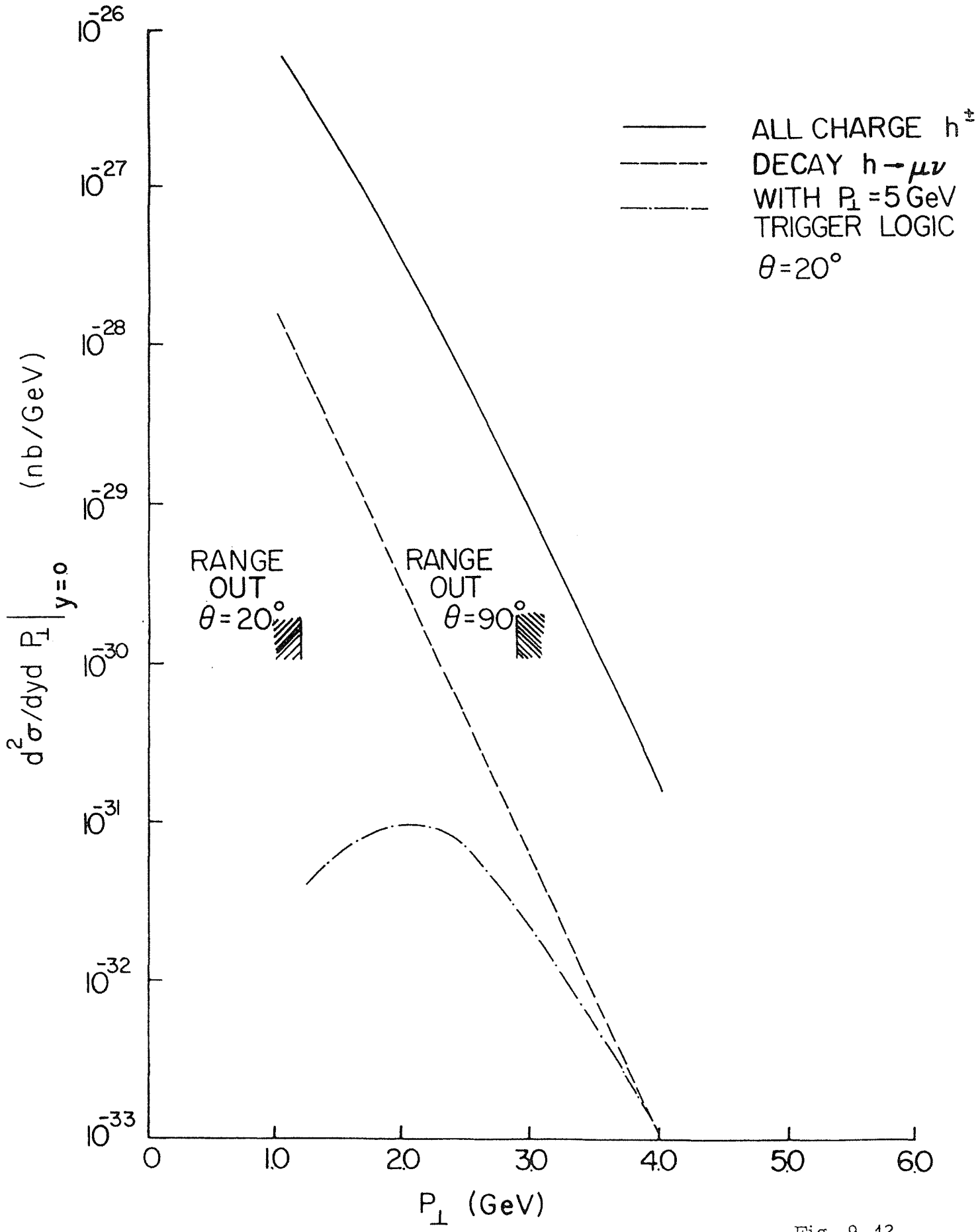
ALL CHARGE h±
DECAY h → μν
WITH P⊥ = 5 GeV
TRIGGER LOGIC
θ = 20°
RANGE OUT θ = 20°
RANGE OUT θ = 90°
d²σ/dyd P⊥ |y=0 (nb/GeV)
10⁻²⁶
10⁻²⁷
10⁻²⁸
10⁻²⁹
10⁻³⁰
10⁻³¹
10⁻³²
10⁻³³
0
1.0
2.0
3.0
4.0
5.0
6.0
P⊥ (GeV)

Fig. 9.12

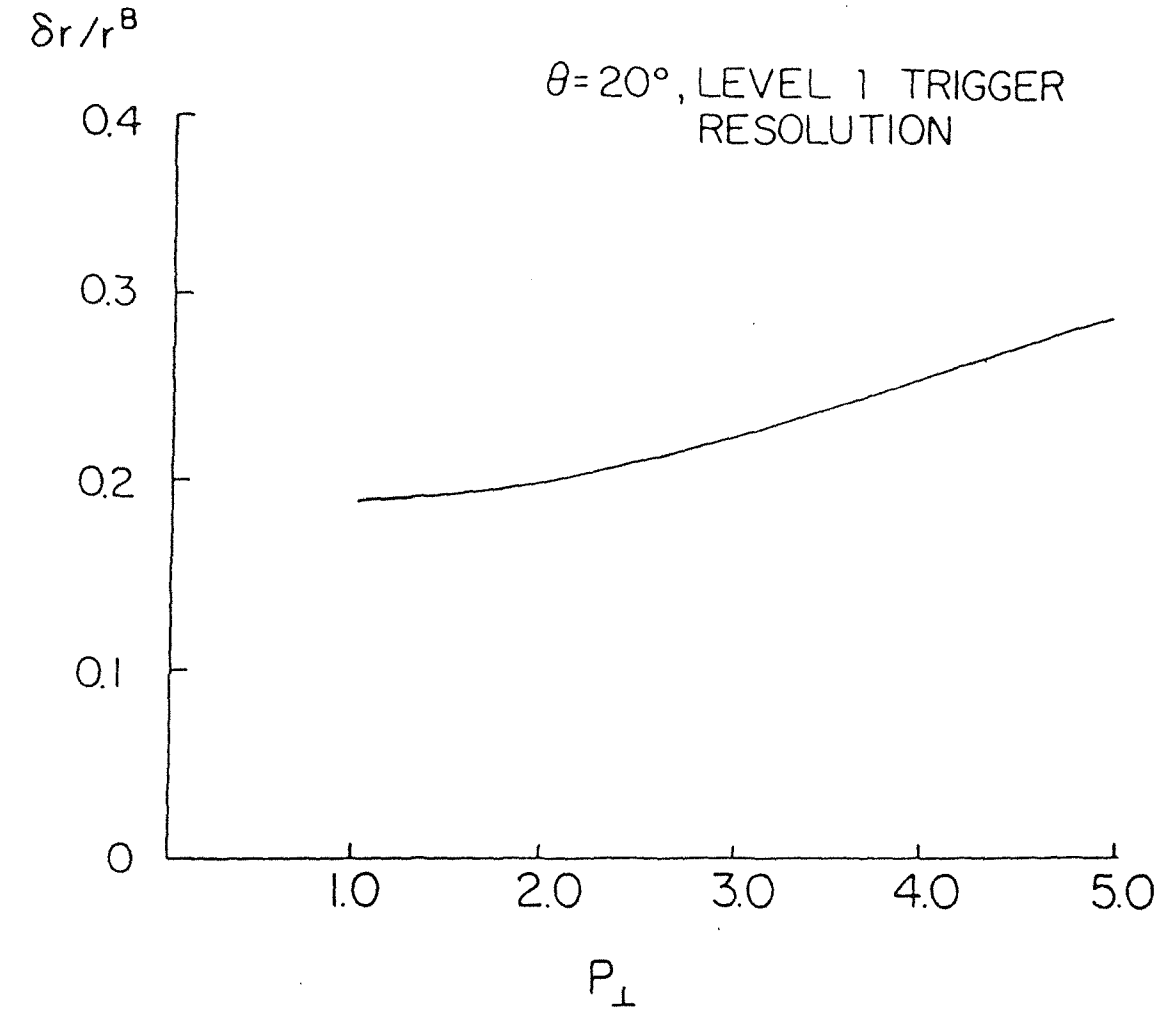
δr/r^B
θ=20°, LEVEL 1 TRIGGER RESOLUTION
0.4
0.3
0.2
0.1
0
1.0
2.0
3.0
4.0
5.0
P⊥

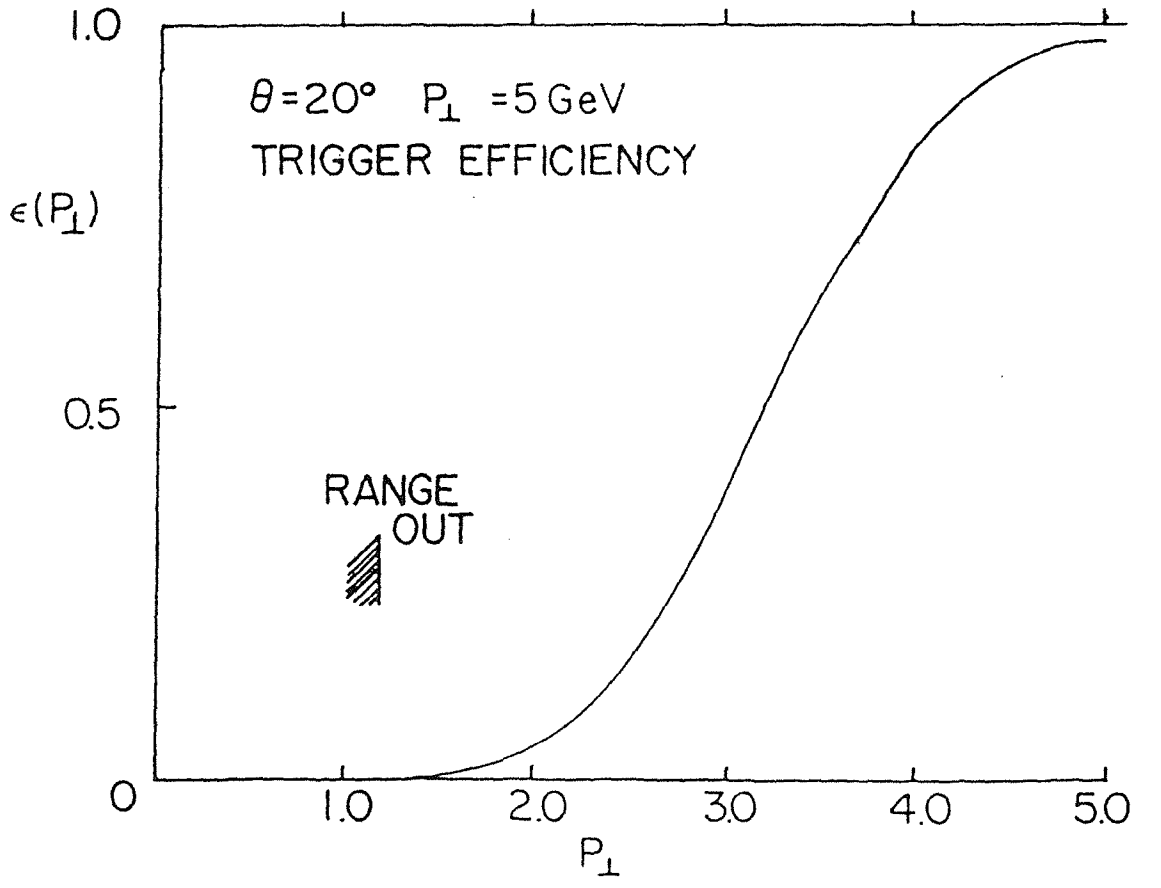
1.0
θ=20° P⊥ =5 GeV
TRIGGER EFFICIENCY
ε(P⊥)
0.5
RANGE OUT
0
1.0
2.0
3.0
4.0
5.0
P⊥

Fig. 9.13

10. TRIGGERS AND ON-LINE FILTERS

10.1 OVERVIEW

With an expected luminosity of $\mathcal{L} = 10^{30}cm^{-2}sec^{-1}$ and an inelastic cross section of ~ 50 mb the instantaneous interaction rate in the detector will be 50 kHz. The trigger must reduce this rate to a few hertz, a reduction factor of 10^4 without introducing appreciable dead time or sacrificing events of interest. To accomplish these goals we will implement a multi-tiered trigger operating in a FASTBUS environment described in Chapter 11. We are planning a trigger comprised of a number of levels of increasing sophistication with the first levels implemented in hardware for speed and the latter stages being done with microprocessors.

Apart from calibration, all triggers will demand a beam crossing and a "symmetric interaction" requirement from scintillation counters placed on both sides of the interaction region near the beam pipes. The beam crossing requirement will minimize cosmic-ray background, and the scintillators will veto "beam-gas" interactions. These conditions are called the "level 0" requirements.

All the triggers that can be generated within the 3.5 microsecond beam-crossing time are included in the level 1 category. They generate no dead-time for the system and are implemented in "hard-wired" logic with inputs being appropriate combinations of analog information from the calorimeter or particle coordinates from the tracking or muon chambers.

The following triggers have been considered and are included here:

1. Muon Trigger
2. Calorimeter Triggers
    a. Transverse Energy (E_T)
    b. Missing Transverse Momentum (MP_T)

c. Jets

d. Electron-Photon

3. Calibration Triggers

The calibration trigger is included for completeness. Presumably it will be used during times when the beam is not available and hence need not necessarily be implemented with the same restrictions as the others.

We imagine that the final trigger will be made up of a weighted logical "OR" of all the separate triggers with the weighting effected through prescaling and determined by considerations of physics interest and yield.

If a level 1 trigger is satisfied, digitization of the data is initiated. At the same time digitization is initiated on analog information used in the triggering process. This information as well as the detailed outputs from the digitizers are passed on to the level 2 trigger by being placed into a buffer that can be accessed by the pool of microprocessors resident in FASTBUS.

As currently envisaged, the microprocessors are organized as follows: some small number of them (~6) will be used to reformat the data and perform simple corrections such as pedestal subtractions. These will be assigned on a functional basis, e. g., one micro will read out the central tracker, another the end-plug calorimeters, etc. Most of the microprocessors (~50) will be devoted to implementing the level 2 trigger. With a trigger rate of ~400 Hz at level 2, each of the micros will have to process about 10 events per second. The number of instructions that can be performed in 100 msec by the powerful micros under consideration is $\sim 10^5$ permitting fairly sophisticated trigger decisions to be made. It is anticipated that the micros can be partitioned to operate on a particular geometrical piece of the apparatus or on the event as a whole.

The system will have sufficient flexibility that further levels of triggering, if needed, could be implemented. It might, for example, be of use to have a third level trigger which would analyze an order of magnitude fewer events with a concomitant increase in sophistication.

We discuss below each of the triggers in an attempt to assess their rates, the information needed, and their cost of implementation.

10.2 MUON TRIGGER

The goal of a muon trigger is to identify muons exceeding a given value of transverse momentum (p_T) by calculating the impact parameter of the muon after it traverses the magnetic field in the muon toroids. Central to this calculation is a rapid determination of the interaction vertex position, and an early determination of a line segment outside the iron.

10.2.1 Vertex Determination

The means by which a fast (<2 μsec) vertex location can be obtained was discussed in Section 4.3. Here we present the results of a simulation of its efficiency and precision. The procedure for vertex location using analog time information from sense wires and delay lines was simulated by a program to which ISAJET QCD jet events were presented. Expected resolutions for the timing information were incorporated; the radii of the chambers contributing to the algorithm were varied, as were the cuts on sense wire ϕ coordinates and the sum of delay times. The simulation assumed 12 azimuthal sectors in the chambers, rather than the 24 or 48 actually proposed.

The mean multiplicity of tracks into the chamber in the event sample was 38. After eliminating sectors with no tracks or ambiguous information, an

average of 6.4 sectors yields a good z coordinate. These independent coordinates give the correct z vertex position with σ_z = 0.5 cm when chambers ar r = 15 and 65 cm are chosen. In the more difficult situation of chambers at r = 30 and 40 cm, σ_z = 1.3 cm. Studies of superimposed individual events indicate that the fast trigger can detect events containing vertices separated by 2-3 cm. The fraction of events which fail to yield a correct vertex is at or below the level of 10^{-3}.

Clearly this simulation overestimates the efficiency of finding a vertex in a real environment where spurious hits, missing hits, and pulse shape variations occur. However, with the proposed doubling of the number of azimuthal sectors over that in the study and the high redundancy of information in the simulated results, we are confident that fast vertex location can be efficiently achieved.

10.2.2 External Muon Chambers

The muon PDT planes outside the iron toroids yield, in level 1, a set of coordinates which represent the drift cell number where hits occur. These give positions quantized to within one drift cell (5 cm in the central region and 2.5 cm in the forward regions).

The selection of muons above some threshold in p_T uses the analog versions of the latched hits in the two PDT stations outside the toroids, w_2 and w_3. To within a certain interval δ, w_2 and w_3 and the vertex coordinate z_1 must satisfy a linear relationship. For example, the algebraic relation for the deviation at the middle station gives

$$|w_3(C_1 - C_2 z_1) - C_3 w_2| \leq \Delta,$$

where the C's are constants determined by the geometry. The deviation Δ depends upon the p_T threshold chosen. Fast analog electronics can easily perform the check of this inequality within the time available for the level 1 trigger. If desired, a similar test can be performed using the non-bend coordinates from the hits in the same sector in order to give some additional suppression against spurious hits.

The level 1 rates expected from this trigger are estimated in Section 9.5 to be about 10 Hz, for full efficiency at $p_T \geq 5$ GeV/c. This rate is dominated by decay muons in the forward and backward direction. Without the p_T cut at the first level trigger, the trigger rate would be expected to be about 500 times larger.

10.3 CALORIMETRIC TRIGGERS

The remaining triggers--Jets, Electron-Photon, Transverse Energy, and Missing Transverse Momentum--depend on the analog information read in from the calorimeters. There are a number of important questions that must be considered in this regard:

1. Trigger Segmentation

   The desire to trigger on local energy deposition in the form of jets, photons, etc., dictates that the trigger components consist of projective towers weighted by $\sin\theta$, pointing to the interaction vertex. In the absence of other constraints, the logical tower size would be set by the size of the smallest jet (in angular extent) that would be encountered or the physical tower size, whichever is larger. The finite extent of the interaction region (σ = 28 cm)

introduces smearing which can be removed if the interaction point is known. In Fig. 10.1 are shown the relative contributions to the resolution in E_T, $\delta E_T/E_T$, due to the assumed segmentation of the detector and due to the finite interaction region size. The energy resolution of the calorimeter, assumed to be $\delta E/E = 0.4/\sqrt{E}$, plays a role only near $\theta = 90°$ for any energies exceeding a few GeV. These considerations suggest that as far as the trigger is concerned the number of subdivisions in the azimuthal angle and rapidity can be decreased by a factor of ~3. This assumes, of course, that the vertex information will not be used in the calorimetric triggers. The E_T smearing from all sources at the trigger level never exceeds ~20% and has no serious effect on the rate. We therefore assume that at the trigger level our towers will be subdivided into units of $\Delta\eta \sim 0.3$ and $\Delta\phi \sim 15°$, corresponding to about 10 of the towers in the actual calorimeter. If these trigger towers are overlapped on the grid of physical towers so that each physical tower appears in two trigger towers, there are about 1000 such trigger towers.

2. Electronic Noise

In order to minimize amplifier noise in the ULA, the integrating times must be long, of the order of microseconds. This precludes the use of this signal for the fast trigger and dictates that we use instead a "fast out" some 200 nsec after the crossing time. The higher bandwidth amplifier needed introduces noise. The "hard-wired" tower structure assumed above helps in this respect since the noise adds stochastically and the signal adds in phase. The noise was estimated in Section 8.3 to be at the level of 13 MeV for a single tower, 40 MeV for a 10 tower trigger signal, and about 0.9 GeV for the full detector. These contribute to E_T smearing at the trigger level.

3.Hadronic and Electromagnetic

One of the chief advantages of a uranium calorimeter is its uniform response to deposited hadronic or electromagnetic energy. Thus there is no well-defined boundary between an "electromagnetic" and a "hadronic" section. Nevertheless, for many reasons, it is useful to divide the detector in this way. For the purposes of the trigger where we wish to identify electrons or photons in the presence of hadronic energy we must make this distinction and for this reason all the trigger towers are assumed to consist of two sections. The first 24 radiation lengths or 1 absorption length will be called the "electromagnetic " whereas the reaminder will be "hadronic." Both sets of signals will be available to the trigger. We go now to a more detailed discussion of the separate triggers.

10.3.1 E_T Trigger

The implementation of this trigger is indicated in Figs. 10.2 and 10.3 which show the overall layout and some details of the E_T, MP_T, and Jet triggers respectively. As can be seen, all the tower energies, weighted by $\sin\theta$, are summed and a single discriminator cut determines the acceptance.

We may estimate the rates for this trigger by using the distribution from UA2[1] which decreases with E_T as $\exp(-E_T/5)$ and we can get a 1000 fold reduction in the trigger rate (50 Hz) by setting an E_T threshold of 35-40 GeV for level 1.

It is not clear that this will be a useful general trigger when the machine is running at full luminosity. The high thresholds required to reduce the rate to manageable levels cut into some physics of great interest, e.g.,

Z^0 decaying into electrons and the leptonic decays of the $W^{\pm}$. For this reason, we have a separate EM E_T trigger whose threshold could be set as low as 5 GeV.

10.3.2 Missing p_T(MP_T)

Referring to Fig. 10.3 we can see the method of obtaining a trigger involving missing transverse momentum. A vector sum of the visible transverse momenta is made by dividing the detector in quadrants and in each quadrant generating the components of E_T weighted by their respective $\sin\phi$ and $\cos\phi$. The appropriately signed sums are then compared to a preset level to determine whether there is any appreciable amount of missing momentum.

The threshold on missing p_T is smeared by effects of angular resolution and energy resolution. Figure 10.4 shows the missing p_T distribution after smearing the intrinsic behavior of the detector (c.f. Fig. 3.1) with these trigger level instrumental effects. In order to achieve a total rate of 10 Hz after a level 1 missing p_T trigger, we require a threshold of about 8-10 GeV/c.

It is clear that there is considerable uncertainty on the threshold which can be set on a purely missing p_T trigger in level 1. Our detector is in fact well suited to doing this due to the uniform response of EM and H compartments to hadronic energy. The refinements available in level 2 triggers (vertex position, fine segmentation, muon information, and reduced noise) should enable the cut to be sharpened giving perhaps a further factor of 10 rejection.

We should note that most of the anticipated use of missing p_T information is made in conjunction with other criteria--for example, the presence of lepton or jet activity--so the full burden of rate reduction need not be placed on the MPT requirement.

10.3.3 Jet Trigger

A simplified schematic of a jet trigger is indicated in Fig. 10.3. The logic will consist of searching for a group of trigger towers with large E_T deposit surrounded by relatively little activity. The real rate from jets has been measured[2] at CERN to be

$$\frac{d\sigma}{dE_T} = AE_T^{-n},$$

where $A = (4.7 \pm 0.3) \times 10^9$ μb and $n = 7.2 \pm 0.2$. At $\mathcal{L} = 10^{30}cm^{-2}sec^{-1}$, the real rate would be 10 Hz for an E_T threshold of 9 GeV.

A simulation of the smearing effects of the detector has been made using ISAJET for $\sqrt{s}$ = 2000 GeV jet production. The E_T deposit was included in 6 trigger towers symmetrized on the tower with maximum E_T; smearing due to the interaction vertex was included. The rate for single trigger jets above 10 GeV was found to be 600 Hz; above 20 GeV the rate was 50 Hz; and above 30 GeV, 10 Hz. Requirement of multiple jet activity, existence of leptons, or of missing p_T can reduce the rates. In level 2, a number of refinements will be made:

1. The vertex position will be inserted and the jet energies recalculated. The event may be rejected if it does not still satisfy jet criteria.
2. The muon information will be added.
3. Multi-jet correlations could be considered.
4. Correlations with missing p_T could be analyzed.

10.3.4 Electron-Photon Trigger

A requirement that E_T in an EM trigger tower exceed 5 GeV will reduce the trigger rate to about 100 Hz.[3] For a 10-GeV threshold, the rate is only a few Hz. This rate is almost wholly due to π^0 showers, according to our ISAJET simulations.

The following tasks would be performed at level 2:

1. Check if the cluster size is small.
2. Check if there is a track pointing toward the cluster. If there is, identify it as an electron, if not, flag it as a photon.
3. Require a TRD verification for electrons.
4. Look for MP_T or jet correlations if these are of interest; also look for e-μ correlations.
5. Compute di-electron masses.

10.4 BACKGROUNDS

The considerations above have used physics as input for estimating rates for various triggers. As may be expected there will be certain backgrounds that will, in general, elevate these trigger rates. Many of these are unknown and will depend on the details of the machine operation, but some can be estimated with some degree of confidence. We consider, briefly, the following:

1. Cosmic Rays

At first glance, it would seem that the ~10 kHz cosmic-ray rate over the detector will present a problem. A closer look reveals that this is not so. The raw rate is reduced by a factor of 7 by considering only the integration time of our muon chambers. The multiple scattering contributes a perpendicular kick of 600 MeV/c which gives us a worst case position resolution at the beam line of ~10 cm. This gives us a

factor of 60 reduction and using the z coordinate we get another factor of 10 leaving us with a rate of 2 Hz for muons to contend with. Further requirements in level 2 that the muon originate near the interaction vertex, coupled with a requirement that there be other particles emanating from the same vertex will eliminate cosmic-ray muons as a source of serious background.

2. Beam Gas

The limited operating experience with the Doubler does not yet permit us to draw any conclusions regarding this background. We propose to veto large fractions of this by having scintillators placed symmetrically upstream and downstream of the detector and tagging events coming from outside the interaction region. It should be noted that the experience at the $Sp\bar{p}S$ has been good in this regard.[1] Any surviving events would be eliminated by using correlations with the energy depostion patterns in the calorimeter and muon tracks in the muon detector.

10.5 SUMMARY

We summarize in the table below for the triggers considered, the rates for level 1 and the required information.

TABLE 10.1 ESTIMATED TRIGGER RATES FOR $= 10^{30}cm^{-2}sec^{-1}$

Trigger	Information Used	Condition	Rate
Level 0	Beam time and detector activity		50 kHz
Level 1			
Muon	Vertex and Muon PDT latch	$p_T > 5$ GeV/c	10 Hz
E_T	ΣE_T in trigger towers	$E_T > 40$ GeV/c	50 Hz
MP_T	Vector sum of tower p_T	$MP_T > 10$ GeV/c	10 Hz
Jet	Local E_T in tower cluster	$p_T > 20$ GeV/c	50 Hz
e/γ	Local E_T in EM tower	$p_T > 5$ GeV/c	100 Hz

Desired rate presented to level two triggers $\leq$ 400 Hz.

REFERENCES CHAPTER 10

1. CERN UA-2 Preprint CERN-EP/83-94, July 14, 1983.

2. CERN UA-2 Preprint CERN-EP/83-135, Sept. 9, 1983.

3. CDF Design Report, Figs. 8-3 and 10-2 were used to estimate rates.

FIGURE CAPTIONS - CHAPTER 10

10.1 Contributions to $\Delta E_T/E_T$ due to the size of the interaction region and due to finite segmentation effects. The segmentation effect is roughly the larger of the curves for constant size and constant $\Delta\eta$.

10.2 First level trigger system schematic

10.3 Schematic diagram for E_T, MP_T, and Jet Trigger - level 1

10.4 Missing p_T distribution including trigger level 1 resolution effects.

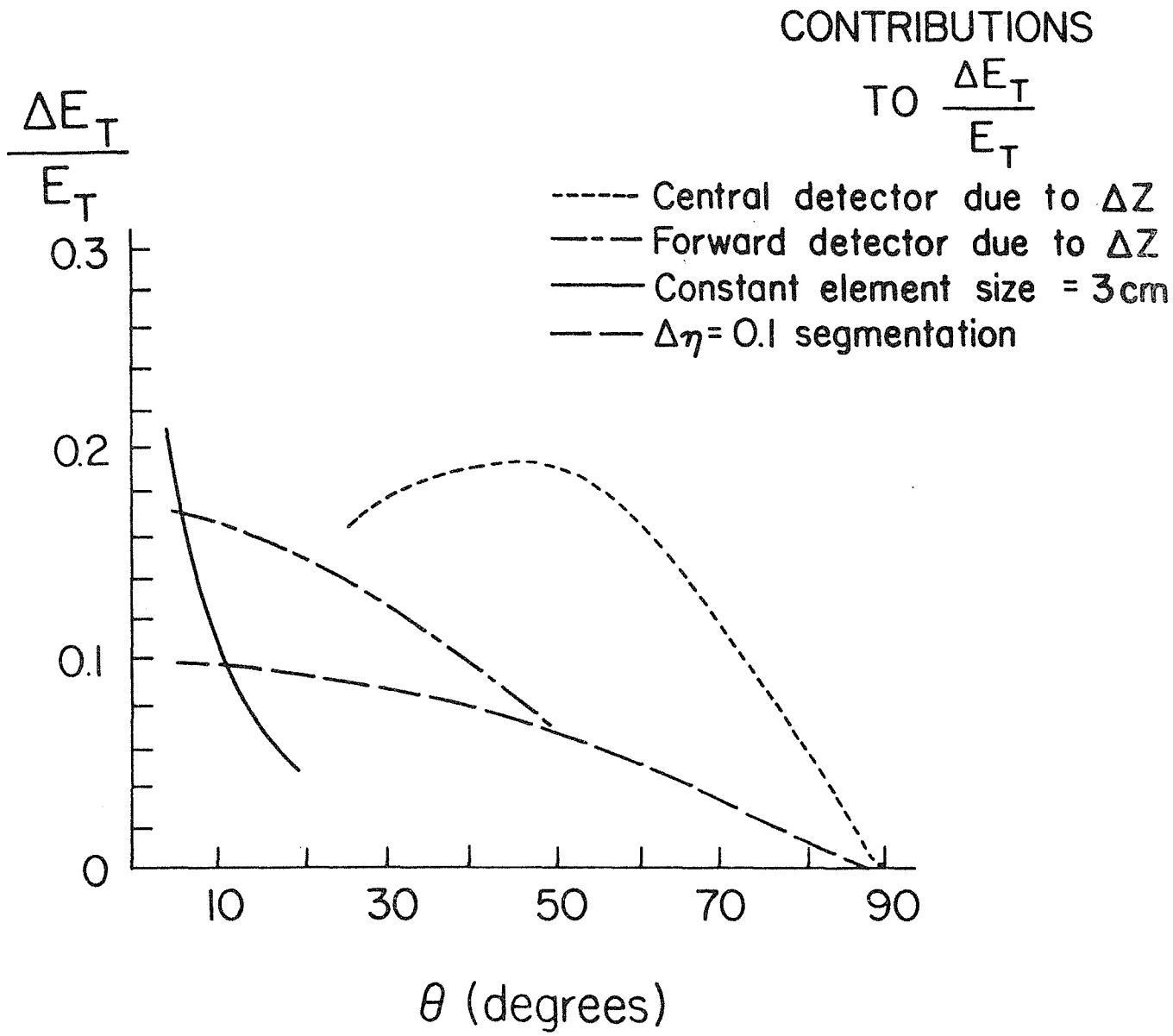
CONTRIBUTIONS
TO $\frac{\Delta E_T}{E_T}$
----- Central detector due to ΔZ
— - — Forward detector due to ΔZ
——— Constant element size = 3cm
— — Δη = 0.1 segmentation
$\frac{\Delta E_T}{E_T}$
0.3
0.2
0.1
0
10
30
50
70
90
θ (degrees)

Fig. 10.1

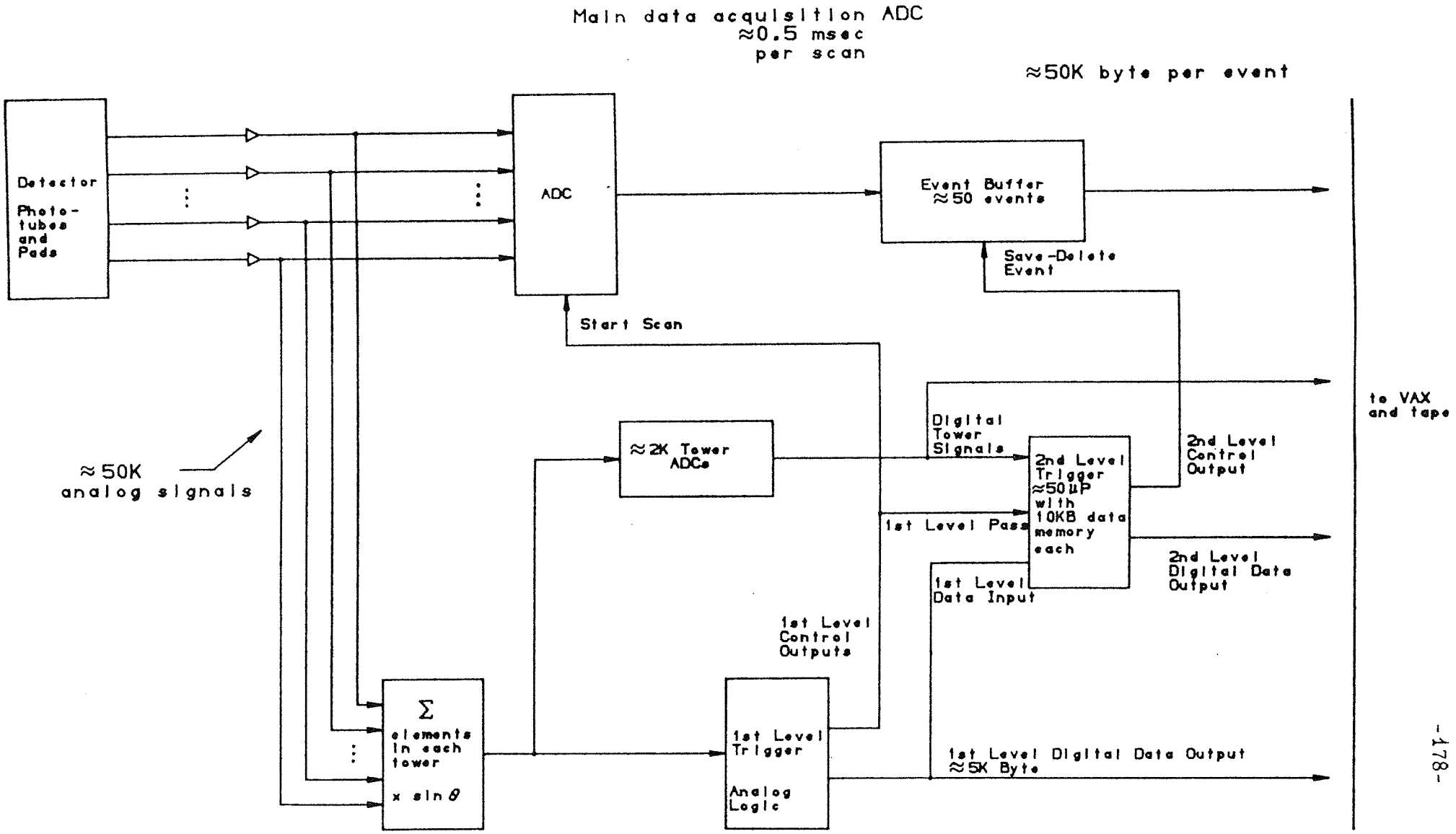
Main data acquisition ADC
≈0.5 msec
per scan
≈50K byte per event
Detector
Photo-
tubes
and
Pads
ADC
Event Buffer
≈50 events
Save-Delete
Event
Start Scan
to VAX
and tape
≈50K
analog signals
≈2K Tower
ADCs
Digital
Tower
Signals
2nd Level
Trigger
≈50µP
with
10KB data
memory
each
2nd Level
Control
Output
1st Level Pass
2nd Level
Digital Data
Output
1st Level
Data Input
1st Level
Control
Outputs
Σ
elements
in each
tower
x sin θ
1st Level
Trigger
Analog
Logic
1st Level Digital Data Output
≈5K Byte

Fig. 10.2

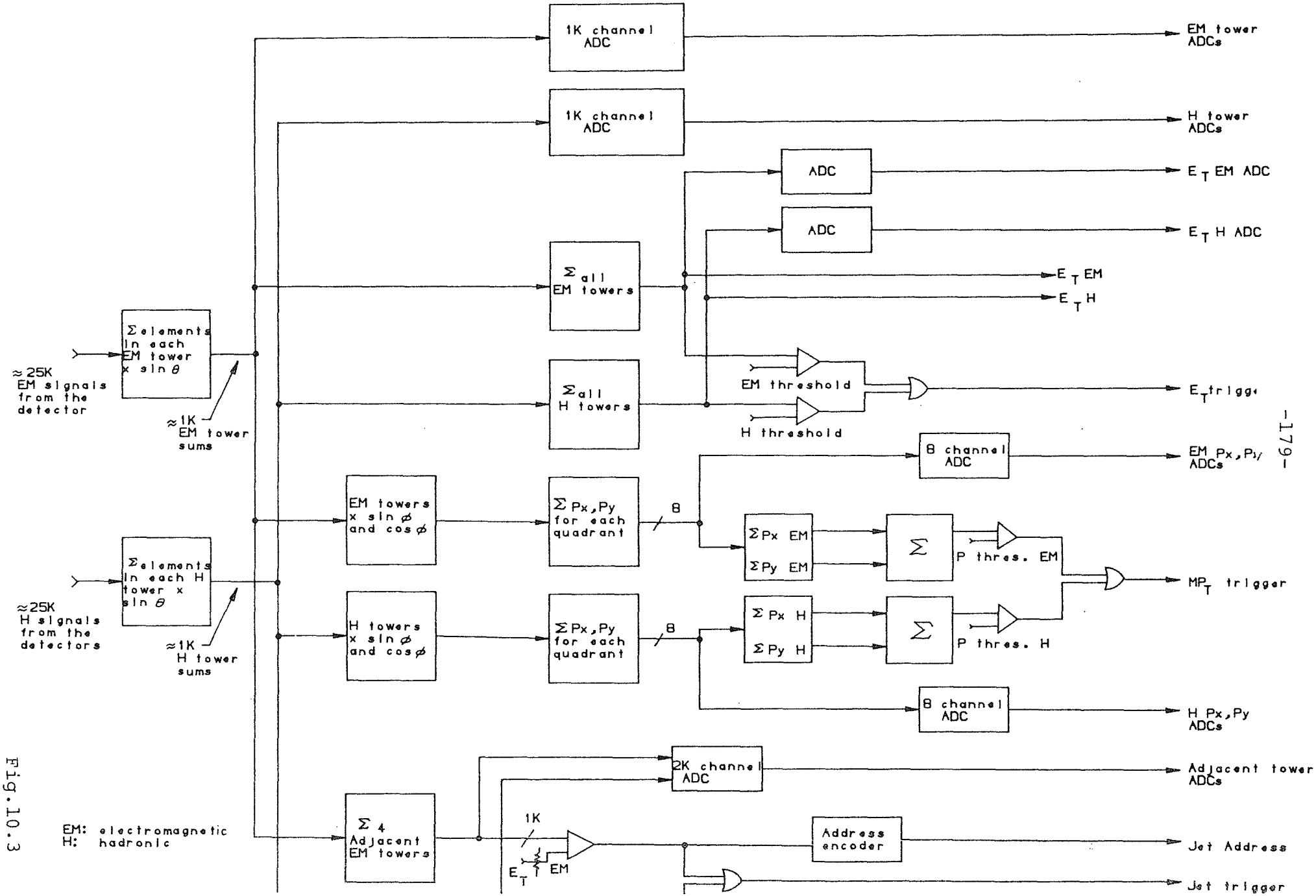
1K channel ADC
EM tower ADCs
1K channel ADC
H tower ADCs
ADC
E_T EM ADC
ADC
E_T H ADC
Σ all EM towers
E_T EM
E_T H
Σ elements in each EM tower x sin θ
≈25K EM signals from the detector
≈1K EM tower sums
Σ all H towers
EM threshold
H threshold
E_T trigg
8 channel ADC
EM Px, Py ADCs
EM towers x sin ϕ and cos ϕ
Σ Px, Py for each quadrant
8
Σ Px EM
Σ Py EM
Σ
P thres. EM
MP_T trigger
Σ elements in each H tower x sin θ
≈25K H signals from the detectors
≈1K H tower sums
H towers x sin ϕ and cos ϕ
Σ Px, Py for each quadrant
8
Σ Px H
Σ Py H
Σ
P thres. H
8 channel ADC
H Px, Py ADCs
2K channel ADC
Adjacent tower ADCs
Σ_4 Adjacent EM towers
1K
E_T EM
Address encoder
Jet Address
Jet trigger
EM: electromagnetic
H: hadronic

Fig. 10.3

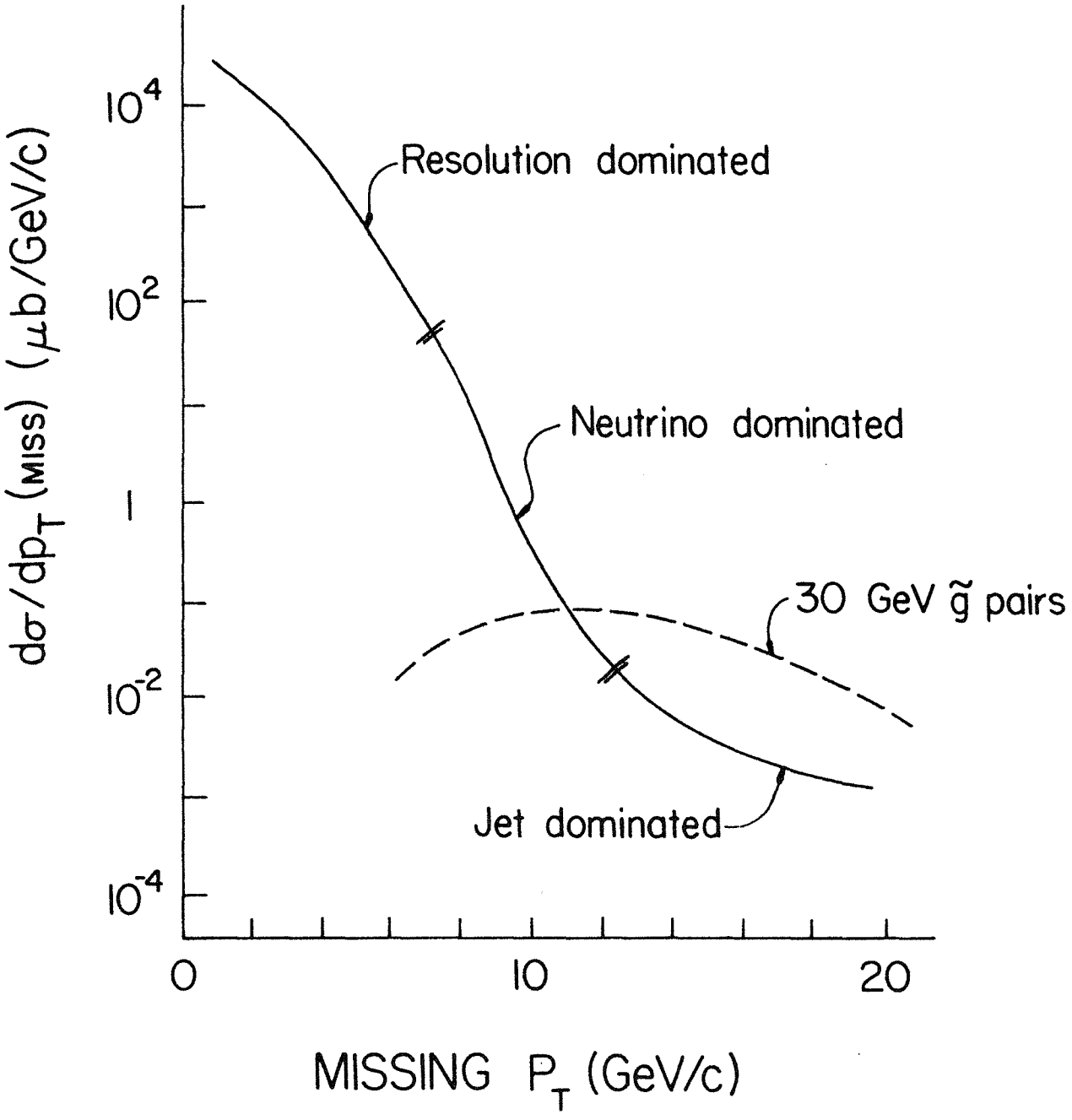
$d\sigma/dp_T$ (MISS) (μb/GeV/c)
10^4
10^2
1
10^{-2}
10^{-4}
Resolution dominated
Neutrino dominated
30 GeV $\tilde{g}$ pairs
Jet dominated
0
10
20
MISSING P_T (GeV/c)

Fig. 10.4

11. DATA ACQUISITION

The data-acquisition system for a detector such as ours must be capable of a variety of tasks, intended to accomplish the following basic objectives:

1. Effectively support installation and debugging.
2. Effectively support calibration and monitoring.
3. Facilitate the detection and reporting of system errors.
4. Select events of interest without introducing excessive dead time.
5. Assemble and organize events with consideration for later analysis.
6. Record events and calibrations.
7. Provide appropriate feed back to experimenters.

Given the likelihood that both the physics objectives and the available hardware will evolve with time, we adopt the following additional objectives:

1. Maintain flexibility by putting as much of the selectivity as possible in programmable devices.
2. Do all trivial corrections to and organizations of the data once and for all at the lowest level.
3. Guarantee sufficiently early operation and sufficient ultimate power by making a system which can be phased and expanded.
4. Attempt to exploit where possible good hardware and software developments made by other groups.

11.1 SYSTEM DESCRIPTION

In the architecture described here there is only one level of hardware trigger. At this level a number of different triggers will run in parallel, discriminating on the basis of such criteria as size and/or number of energy depositions in the EM or hadron calorimeter or the presence of muon-like

tracks leaving the iron (see previous chapter). The final decision is an OR of these individual tests and all decisions must be made between beam crossings. Events selected by one of these triggers will then be digitized and read into the data acquisition/filtering network. The system is intended to evolve in terms of the number and kinds of components as the luminosity increases and as trigger criteria change. The system, as described here, is in a mature but not necessarily final state. Figure 11.1 shows the overall system. Figures 11.2 and 11.3 show the global segments and typical local segments in some detail.

The local segments each correspond to a detector system which is functionally distinct and is, in general, the responsibility of a single group to design, construct, debug, and calibrate. Subsystems of this system will then be read from the digitizing electronics into separate buffers on the segment. Consider the example in Figs. 11.1-11.3; for each digitized event there will be a relatively short data block in each of the approximately three buffers on each of the six segments for a total of about 20 buffers filled in parallel.

In this system, the host computer is assumed to be a large VAX and the bus structure is FASTBUS. The microprocessors which will be used in this application will be chosen from among the new powerful 32 bit processors such as the M68000, NS16000, or 80386 and equipped with floating point coprocessors. The processors will be compact (~ 1 board) and will be interfaced to make use of all features of FASTBUS. They will support up to 4 MBytes of memory although for most applications only ~1 MByte will need to be installed. Such processors are predicted to have processing power in excess of a VAX-11/750. All applications software for the processors will be prepared, cross

compiled, and downloaded from the VAX. The boxes labeled SI in the figures are segment interconnects between the various FASTBUS segments.

11.2 SUBSYSTEM DESCRIPTIONS

11.2.1 Hardware Trigger and Digitization System

The various trigger systems discussed in Chapter 10 are assumed to have certain properties as seen by the data-acquisition system.

1. All hardware trigger decisions will be made between beam crossings which in certain running configurations may be separated by as little as 3.5 microseconds.
2. All hardware triggers will have an adjustment which allows one to increase or decrease the acceptance of that trigger, in a rational way, in order to adjust the sharing between various triggers and to match the overall yield of the hardware triggers to the processing power available in the programmable event filtering network.
3. All hardware triggers, in addition to supplying a trigger signal, will supply a bit pattern which indicates in some detail where in the detector and how the trigger criteria were satified. This bit pattern will be read into the data-acquisition system to be used as a guide in the further filtering of events.
4. Hardware trigger systems which utilize compact characterizations of the events, such as weighted analog sums of calorimeter signals, will provide for the digitization of those characterizations so that they, along with the rest of the event data, can be read in for events satisfying the trigger criteria.

The digitizing electronics, ADC's and TDC's, are assumed to have certain properties:

1. The worst case time for digitization of all signals is 0.5 msec with digitization typically complete within 0.2 msec.
2. The result of the digitization will consist of a 16-bit address and a 16-bit ADC value and/or a 16-bit TDC value for each hit.
3. The digitizing system will suppress the readout of channels which have not exceeded a defined threshold and will allow readout at a rate of at least one 16-bit word every 100 nsec for each of as many parallel streams as necessary.
4. A system will be provided which will allow an efficient determination of the calibration constants for each electronic channel (pedestal, slope, etc.).

The detector itself will contain about 80,000 elements. Mean occupancy in an event will vary between 5% and 20%, for different portions of the detector. Each detector hit requires a minimum of 4 bytes of data to specify its address and value. We estimate that about 40,000 bytes of data, on the average, will be required to describe an event. If the readout were done into a single buffer, the time required would be 2 msec. Assuming that the hardware triggers pass 1/500 of all events at a luminosity of $3\times10^{30}cm^{-2}sec^{-1}$, such a scheme would imply a dead time of 50%. By using ~20 parallel read out paths, as described above, even allowing for the tendency of data not to be distributed uniformly across these paths, the dead time resulting from digitization and read out should be less than 10%.

11.2.2 Local Acquisition Level Segments

The several local FASTBUS segments (Fig. 11.3) contain the buffer-memory memory modules, calibration control modules and microprocessors associated with a particular functional portion of the detector (e.g., central tracker, end calorimetry, etc.). For the purpose of handling beam-beam events, the function of the intelligence on these separate segments is to assemble from the various incoming paths a properly formatted event fragment and to notify processors at a higher level of its identity, size, and storage location. This function will likely be performed initially by microprocessors of the type described above, but in a high rate environment they should be augmented, as indicated in Fig. 11.3, by bit slice processors which can very efficiently perform functions such as correcting all ADC and TDC values for their calibration constants.

A bit slice processor is a high-speed micro-coded device based on bit slice technology such as the AMD 2900 series or the Motorola 10800/10900 series. These devices are much faster than general microprocessors especially for simple computations such as performing calibration constant corrections but are difficult to program. This programming difficulty limits their use in complex programs such as those used in pattern recognition. Bit slice based devices have been described by FASTBUS manufacturers as future products. Involvement with such devices should be reserved until all problems associated with the general microprocessors are resolved. The inclusion of a single device of this type on each segment handling the event assembly and calibration corrections before the micros see the data significantly increases the effective compute power available. Since this will not become important until high luminosity operation, a bit slice device is probably not necessary during the early running.

During non-beam activity such as calibrating and debugging, the microprocessors on each segment can operate that segment in a manner completely independent of the rest of the system and report results, either continuously or at completion, to a particular task running in the VAX at the control level.

11.2.3 Global Level Segments

This level, shown in Fig. 11.2, consists of perhaps 40 general microprocessors, of the kind described earlier, running on two or more FASTBUS segments. Here data from all portions of the detector are available. The primary function of the intelligence at this level is to select events of interest and to construct complete records of these events. The flow of event filtering and assembly is expected to go as follows:

1. A free processor at the global level takes the trigger bit pattern data for the next event and reads in the corresponding trigger signal digitizations. These data are routed directly to a global segment as shown in Fig. 11.2.
2. The processor then verifies the trigger by applying a more sophisticated algorithm to the particular data which were used to satisfy the hardware trigger. At this level it is possible to have criteria which combines information from several hardware triggers.
3. If the event is not rejected, the processor proceeds to obtain further data for the event, perhaps this time the normal full digitizations for the section of the detector involved in the trigger. This fragment of the event will be found stored in a buffer on a lower level acquisition segment.
4. With the analysis of this fragment, the processor rejects the event or selects an additional fragment to read in, either to continue the

verification of the hardware trigger or to apply criteria not contained in the hardware trigger.

5. When the entire event has been read in and assembled and is still found to be of interest, the event is sent to the VAX to be recorded.
6. Other events which come while this processor is busy are taken by other processors.
7. When events are rejected, the space occupied by their fragments on the local level are freed for other reuse.

In addition to filtering, major processing tasks of a monitoring nature, such as tracking muons through the detector to monitor gains, can be performed at the global level. Also at this level a processor can be dedicated to monitoring the overall performance of the filtering system by tabulating the findings of all of the filtering processors.

11.2.4 Control Level

This level consists of a number of tasks running in a large VAX. Its function is to control the operation of the entire system in terms of initializing it and of instructing it to assume various running configurations as desired. As presently conceived this will also be the level responsible for writing the final output tapes. Processors on the levels below will pass along events identified as being of interest. These events will then be sorted on the basis of trigger and filter determined categories and written into files of particular event types. When these files reach the appropriate size, they will be written to tape. In addition, it is in the VAX that the operators of the experiment have access to the data. For studies of detector subsystems, a large number of independent tasks running on the VAX will each be able to access selected subsets of the data flowing from the detector and

during times when the beam is not on will be able to request changes in the detector's running mode. Extensive facilities will be available to provide continuous monitoring of the detector operation as well as physics analysis on a sampling basis.

11.3 SOFTWARE IMPLICATIONS

Performing the selection process in software increases flexibility. This software breaks logically into two aspects: 1) the system software, 2) the applications software. The system software will be machine dependent and will depend to some extent on the position of the device within the network. The applications software, on the other hand, should be written in as machine independent a way as possible. This software includes analysis and filter algorithms. One imagines wanting to run the same algorithms at various times in the course of the life of the detector in various different devices at different levels in the network. For this reason well defined standards will be set for software modules. In particular the way in which such modules interact with (read and write) the data stream and the way in which they interact with the control layers of programs will be standardized very early. In addition, the basic format of the data structure for events, constants, and control information will be established and maintained at all levels from the bit slice to the offline processor. In terms of the basic data-acquisition algorithms, they will first be written and exercised in the VAX. When the micros become operational, these algorithms will migrate down to them. When the bit slice processors or other new devices become operational the appropriate algorithms will be migrated into them. Thus the system should be operating from a very early state as a pure VAX system and as

required will become more powerful with the addition of hardware and the migration of software into it.

11.4 INSTALLATION AND DEBUGGING

Other very important functions of the data-acquisition system which have not been discussed are 1) installation and debugging and 2) monitoring and calibration. The questions of installation and debugging relate in large part to the ease with which the system can be decomposed into a significant number of segments which are sufficiently separate that workers do not interfere with each other and yet can continue to exploit the power and facilities of high-level computing. A logical and the simplest division of this system is by low-level segment. A somewhat more difficult implementation, in which individual micros working with individual input buffers can operate independently from the rest of the system, will also be possible. Partitioning of the system can be either "effective" or "actual." "Effective" partitioning will occur when the host VAX grants a particular task running within it exclusive control of a particular segment or micro/input buffer. "Actual" partitioning will occur when the host VAX denies all access across the segment interconnect into a particular segments and a small VAX is connected directly into that segment. The configuration of a small VAX connected directly into a single segment will also be used in the case of test beam operations.

11.5 CALIBRATION AND MONITORING

It will be necessary periodically to do monitoring and calibrating using pulsers. There is no reason why an individual micro on an individual segment

cannot simply perform this function in its entirety for a particular device on its segment. It would control the ramping of the pulser (via the CAL CTL module in Fig. 11.3), accumulate the data and calculate the constants. These constants would then be sent up to the VAX for recording. In this way the entire process will go very quickly since it will be done in parallel for every detector type in every region. It will be done in a closed loop form with the micro capable of checking calibrations which it finds questionable by rerunning the relevant points with higher statistics or finer step sizes. As mentioned earlier this system also naturally accomodates setting aside some processors to analyze events identified by the other processors as being of interest in monitoring the performance of some portion of the detector, such as in the case of "through going" muons.

11.6 SYSTEM SUMMARY

The data acquisition system for DØ performs a variety of tasks related to the collection, selection, recording, and monitoring of data from the detector. The architecture described, built on FASTBUS segments, allows efficient parallel event processing as well as flexibility in structure. A large number of powerful microprocessors allow sophisticated event filtering, with multi-user online control and data analysis provided by a VAX 11/790. Some details of the FASTBUS components required for this system are indicated in Table 11.1. The VAX should be equipped with adequate memory and disk storage, video displays, printers, tape drives, and terminals.

TABLE 11.1

Fastbus Hardware

Number	Description
8	Crates, Power Supplies, Cooling
8	Segment Interconnects
20	Buffer Memories
50	Micro Processors
1	Host Processor Interface
8	I/O Registers
8	Bit Slice Processors

FIGURE CAPTIONS - CHAPTER 11

11.1 Block diagram of data acquisition system. HI is host interface; SI is segment interconnect.

11.2 Schematic diagram of the global segments

11.3 Schematic diagram of typical local segments (central tracking and one end plus end plug calorimeter).

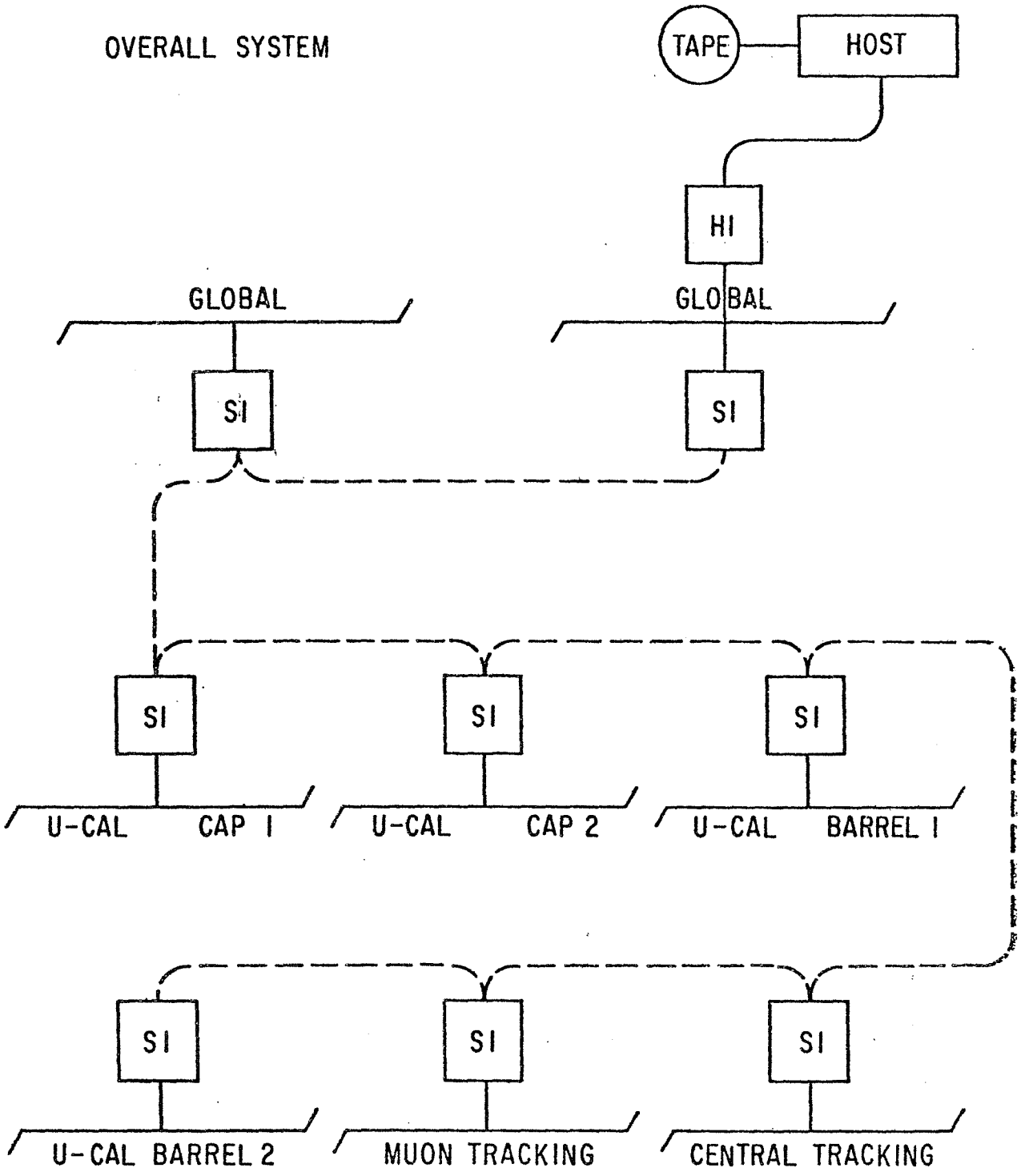
OVERALL SYSTEM
TAPE
HOST
HI
GLOBAL
GLOBAL
SI
SI
SI
SI
SI
U-CAL CAP 1
U-CAL CAP 2
U-CAL BARREL 1
SI
SI
SI
U-CAL BARREL 2
MUON TRACKING
CENTRAL TRACKING

Fig. 11.1

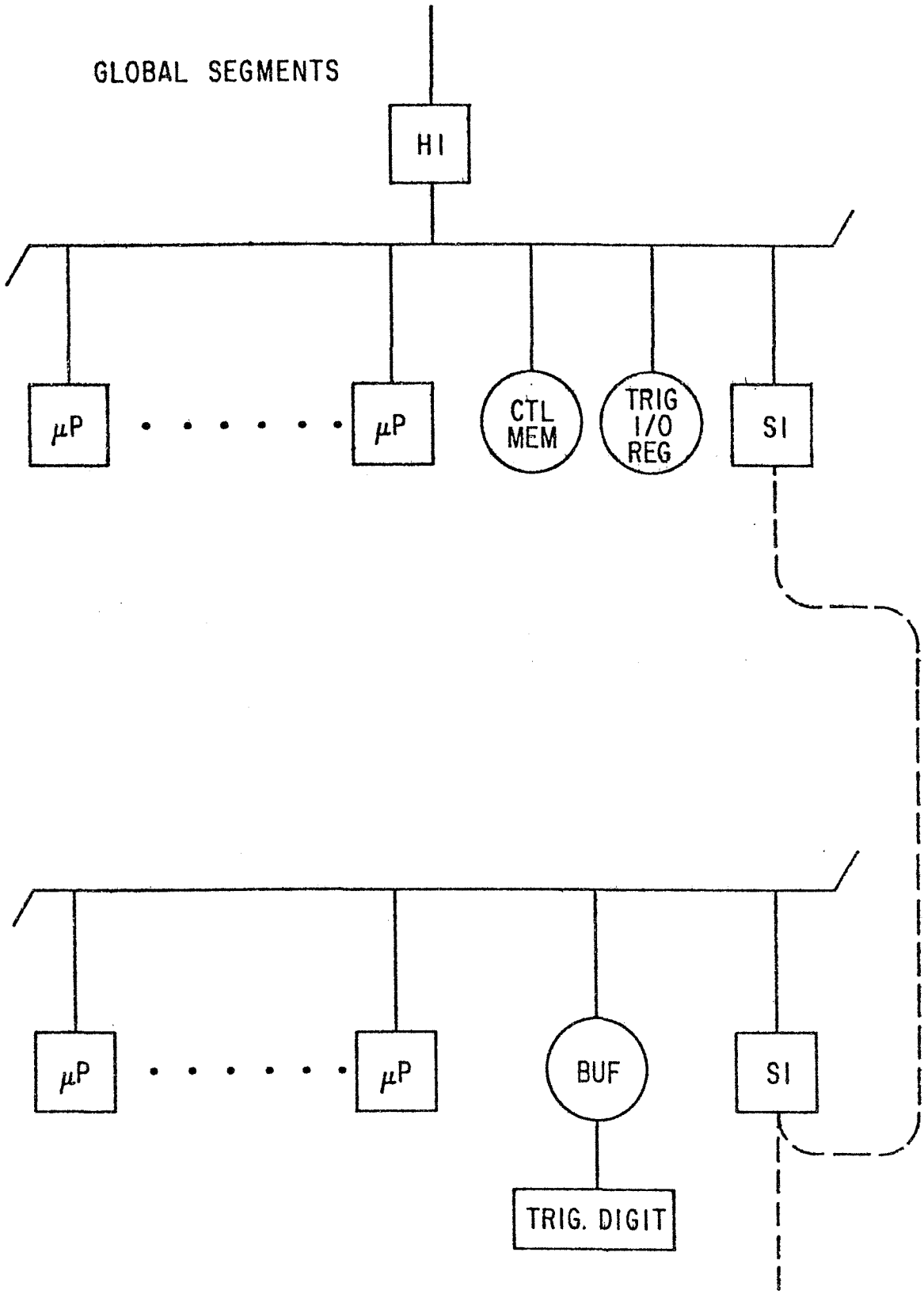
GLOBAL SEGMENTS
HI
μP
μP
CTL MEM
TRIG I/O REG
SI
μP
μP
BUF
SI
TRIG. DIGIT

Fig. 11.2

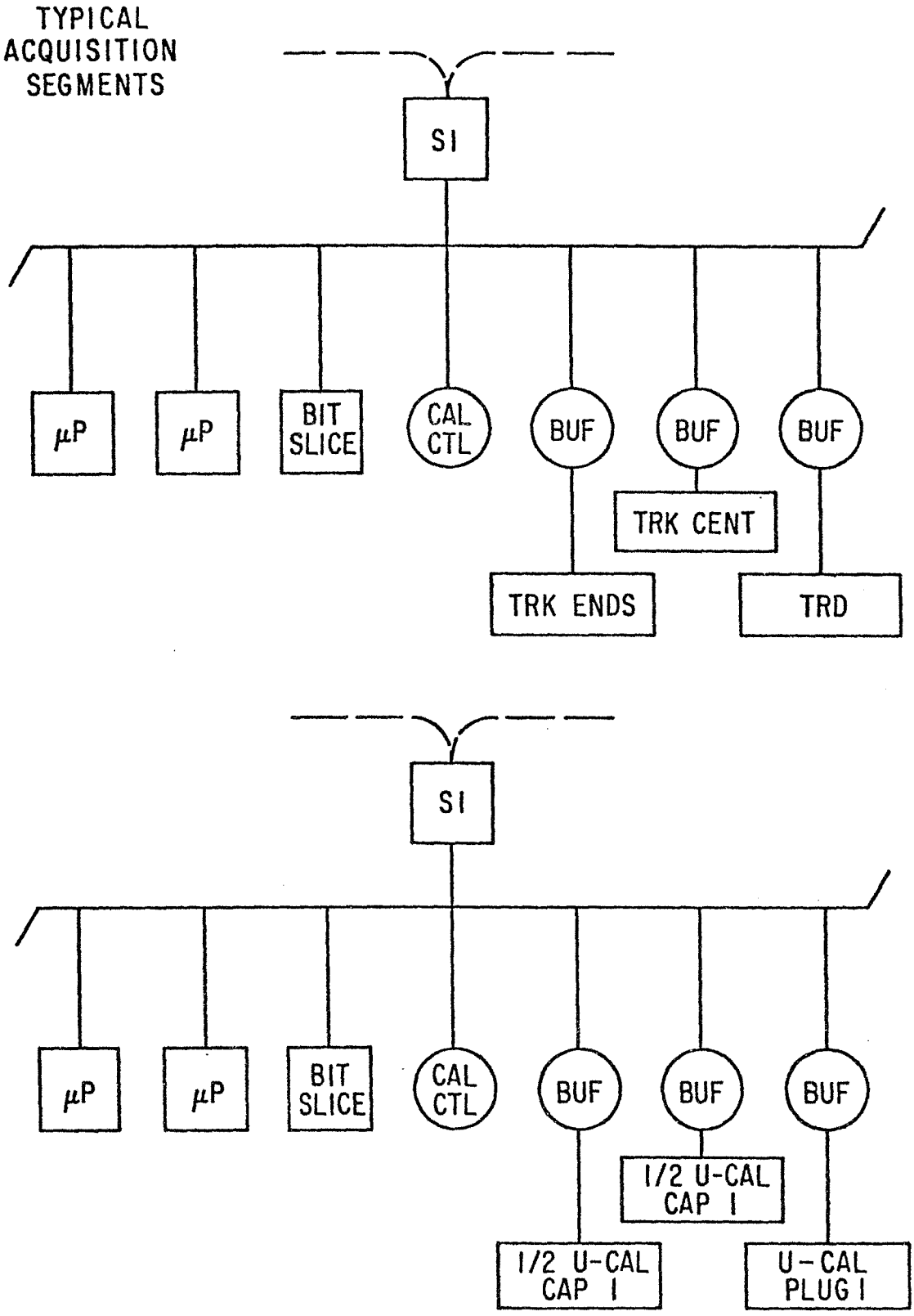
TYPICAL
ACQUISITION
SEGMENTS
SI
μP
μP
BIT
SLICE
CAL
CTL
BUF
BUF
BUF
TRK CENT
TRK ENDS
TRD
SI
μP
μP
BIT
SLICE
CAL
CTL
BUF
BUF
BUF
1/2 U-CAL
CAP I
1/2 U-CAL
CAP I
U-CAL
PLUG I

Fig. 11.3

12. ASSEMBLY AND MOUNTING

The assembly hall, as presently envisaged, would consist of a 4000 sq. ft ground level area and a similar size pit at the level of the collision hall 35 ft below grade. Preliminary versions of hall design are shown in Figs. 12.1-12.3. Both of these areas will be serviced by a single 50-ton crane and perhaps an additional 20-ton unit.

It is envisaged that the ULA detector will be constructed in modular form. The 5-10 ton modules, complete with liquid container skins, will be assembled, tested, and then transported to the assembly hall. At the hall the modules will be inserted into the large vacuum vessels for the central and end-cap detectors. This will be done at the upper level.

In parallel with the ULA assembly, we expect to construct the iron toroids for the central and end cap detectors on the floor of the pit. When the toroids and ULA detectors are complete, the ULA will be lowered by hydraulic platform and inserted horizontally into the toroids. The floor of the assembly pit must have enough room to allow the five major sections of the detector to be assembled and serviced without interference between them.

After assembly of the central toroid and the central ULA, the central tracking detectors will be inserted. The sections of the detector will then be brought together complete with the Collider and main-ring beam pipes which will thread through the sections. The connections between the pipe sections will have flanges and may have valves, if baking out the pipes in situ cannot be accomplished.

The assembly hall will have cryogenic services (nitrogen and argon) at both the upper and lower levels, and separately inside the collision hall. Movement of the detector, which should take less than a day, will be done with liquid argon in the system. Transfer between the assembly hall and collision

hall cryogenic systems will be accomplished with a separate moveable cryogenic system.

When the detector is ready to be inserted, the shield door will be unstacked using the 50-ton crane. We will need a door opening large enough that the complete detector will span the requisite 120 ft from assembly area to collision hall. The detector will carry its harness of cables with it from the assembly pit. If the move can be accomplished in this manner we expect the detector would be operational within a day of the actual move. It is possible to contemplate a scenario, where central and end sections of the detector move individually into the hall, but the additional complexities of multiple cable harnesses, transfer lines, and beam pipe connection might significantly increase the time required for installation and removal of the detector.

For servicing the ULA detector we expect to put only ruggedized preamps on the periphery of the cryostats and all other electronics in more accessible locations near the edges of the muon steel or in the counting rooms. We intend however to allow the central detector to be serviced in situ by splitting the end iron and moving horizontally so that it can "clam shell" around the beam pipe, which would allow room for the intermediate iron toroids to be partially retracted. The most severe constraint that we face in this regard is the position of the low-β quads which limit longitudinal movement.

Service to the ULA detectors is limited to hatches through the vacuum vessels which permit access to feedthrough connections for signals, high voltage, and to LN_2 cooling coils and to liquid argon feed lines. Since all modules will have been previously tested, and since we are considering a design for the readout to avoid blocking capacitors we expect that no access to the inside of a ULA module will be necessary.

FIGURE CAPTIONS - CHAPTER 12

12.1 Preliminary site plan for the DO area.

12.2 Preliminary floor plan showing upper and lower assembly areas and the collision hall.

12.3 Preliminary sectional views of assembly and collision halls.

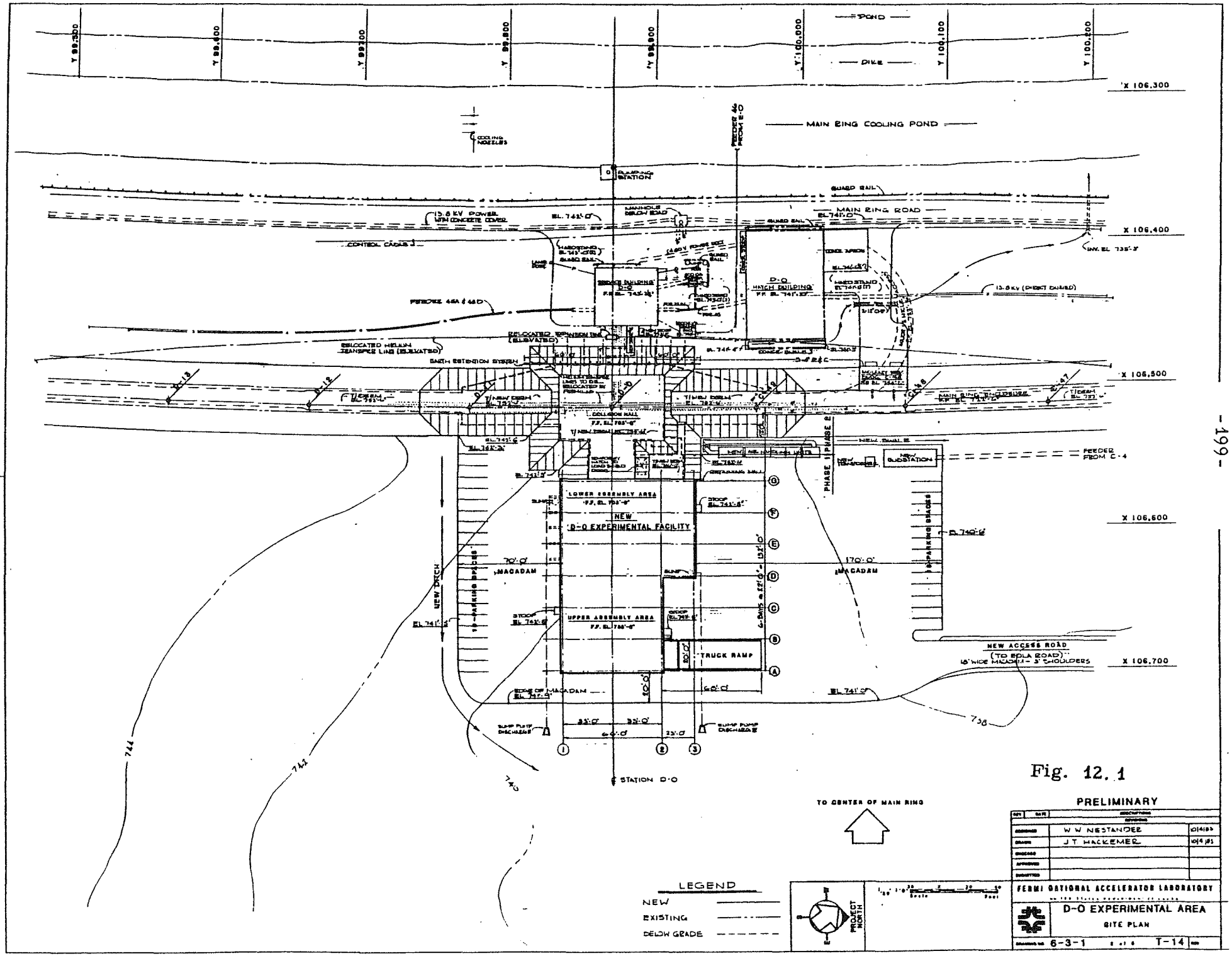
MAIN RING COOLING POND
MAIN RING ROAD
NEW D-O EXPERIMENTAL FACILITY
LOWER ASSEMBLY AREA
UPPER ASSEMBLY AREA
TRUCK RAMP
NEW ACCESS ROAD
(TO BOLA ROAD)
STATION D-O
TO CENTER OF MAIN RING
LEGEND
NEW
EXISTING
BELOW GRADE
PROJECT NORTH
PRELIMINARY
W W NESTANDER
J T HACKEMER
FERMI NATIONAL ACCELERATOR LABORATORY
D-O EXPERIMENTAL AREA
SITE PLAN
6-3-1
T-14

Fig. 12.1

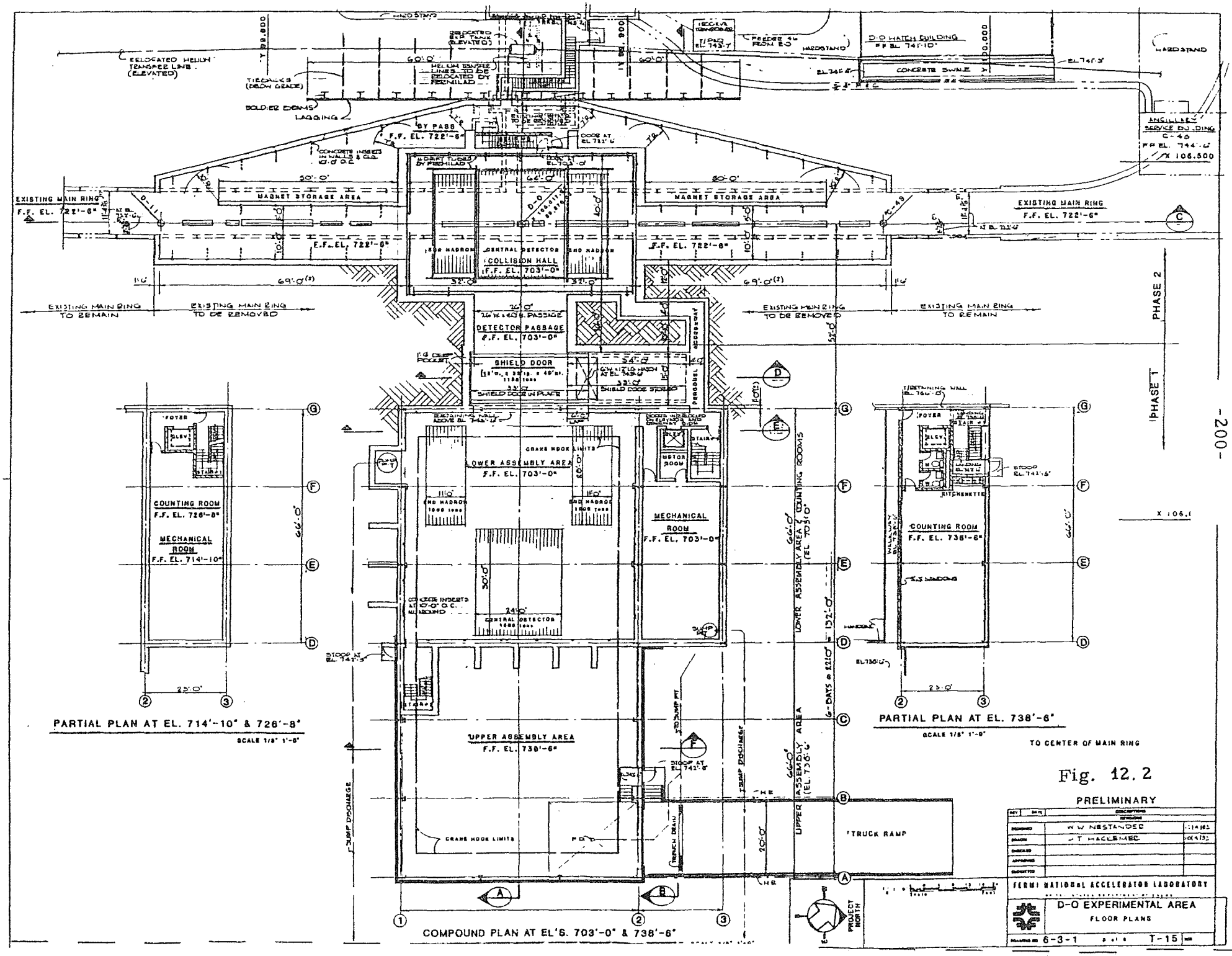

Fig. 12.2

PRELIMINARY

DESIGNED	W.W. NESTANDER	11/85
DRAWN	J.T. MACLEMED	06/13/
CHECKED		
APPROVED		
ENGINEER		

FERMI NATIONAL ACCELERATOR LABORATORY

D-O EXPERIMENTAL AREA
FLOOR PLANS

6-3-1 T-15

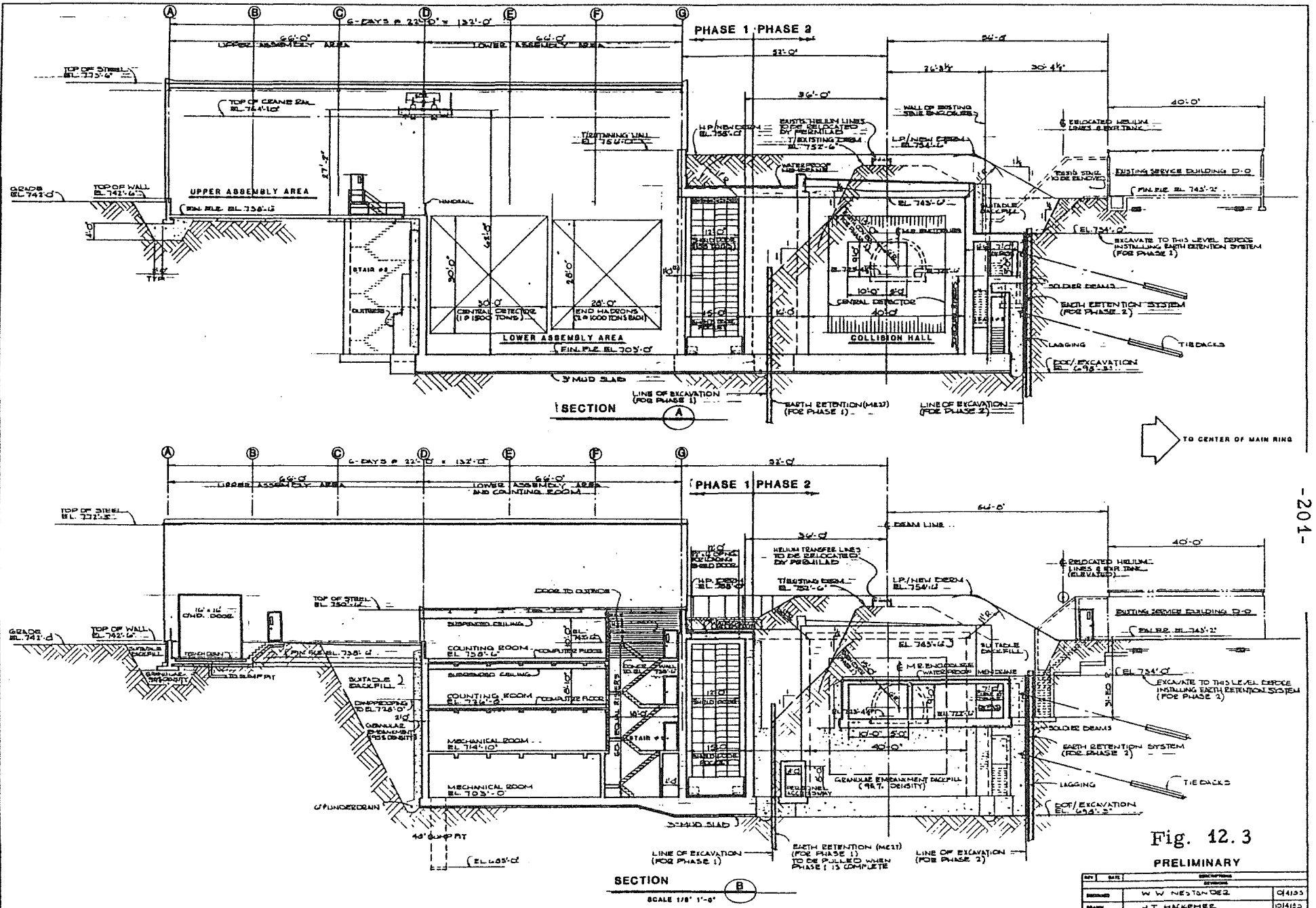

-201-

Fig. 12.3

PRELIMINARY

DESIGNED	W W NESTANDER	9/1/83
DRAWN	J T HACKEMEE	10/1/83
CHECKED		
APPROVED		
SUBMITTED		

FERMI NATIONAL ACCELERATOR LABORATORY

D-0 EXPERIMENTAL AREA

SECTIONS

8-3-1 T-16